# MATRIX-ENABLED DAMAGE TOLERANCE IN OXIDE CFCCs

AFOSR CONTRACT NO. F49620-02-1-0128
FINAL REPORT

Frank W. Zok
Materials Department, University of California, Santa Barbara, CA 93106
Phone: (805) 893-8699; Fax: (805) 893-8486; E-mail: zok@engineering.ucsb.edu

Carlos G. Levi
Materials Department, University of California, Santa Barbara, CA 93106
Phone: (805) 893-2381; Fax: (805) 893-8486; E-mail: levic@engineering.ucsb.edu

Robert M. McMeeking
Dept. of Mechanical Engineering, University of California, Santa Barbara, CA 93106
Phone: (805) 893-8434; Fax: (805) 893-8651; E-mail: rmcm@engineering.ucsb.edu

The objective of this program has been to elucidate the underlying mechanisms by which porous matrices give rise to composite toughness in the absence of interphases between the fibers and the matrix, the role of microstructure and processing in attaining this behavior, and the mechanics associated with the deformation, cracking and failure of the composites. The broader goal has been to develop the knowledge base necessary to exploit the nonlinear phenomena occurring within the matrix. Properties of prime interest include in-plane tensile strength and notch sensitivity, subject to both fiber-dominated and matrix-dominated loadings. Recognizing that changes in the structure of the porous matrix have opposing effects on the properties of interest (enhancing some while compromising others), the research has sought to identify the microstructural parameters that provide a desirable balance of composite properties. The key variables explored were those pertaining to the characteristics of the porosity, notably its content, as well as the nature and extent of the bonds which determine both the strength of the particle network within the matrix and the strength of the fiber-matrix interface.

The highlights of the program are summarized below. Additional details are in the appended papers.

## I. Mullite/Alumina Mixtures for Use as Porous Matrices

Weakly bonded particle mixtures of mullite and alumina have been assessed as candidate matrices for use in porous matrix ceramic composites. Conditions for the deflection of a matrix crack at a fiber-matrix have been used to identify the combinations of modulus and toughness of the fibers and the matrix for which damage tolerant behavior is expected to occur in the composite. Accordingly, an experimental study on modulus and toughness of particle mixtures as well as the changes in these properties following aging at elevated

# REPORT DOCUMENTATION PAGE

Form Approved
OMB No. 074-0188



| 1. AGENCY USE ONLY (Leave blank) | 2. REPORT DATE | 3. REPORT TYPE AND DATES COVERED |
|---|---|---|
| | 03/29/2006 | Final Technical 20020101-20050630 |

**4. TITLE AND SUBTITLE**
Matrix Enabled Damage Tolerance in Oxide CFCC's

**5. FUNDING NUMBERS**
F49620-02-1-0128

**6. AUTHOR(S)**
Zok, Francis W.

**7. PERFORMING ORGANIZATION NAME(S) AND ADDRESS(ES)**

The Regents of the University of
California
Office of Research
University of California
Santa Barbara, CA 93106-2050

**8. PERFORMING ORGANIZATION REPORT NUMBER**

**9. SPONSORING / MONITORING AGENCY NAME(S) AND ADDRESS(ES)**

Air Force Office of Scientific Research/NA
801 N. Randolph Street
Arlington, VA 22203-1977
Dr. Byung-Lip Lee

**10. SPONSORING / MONITORING AGENCY REPORT NUMBER**

AFRL-SR-AR-TR-06-0123

**11. SUPPLEMENTARY NOTES**

**12a. DISTRIBUTION / AVAILABILITY STATEMENT**

Approved for public release,
distribution unlimited

**12b. DISTRIBUTION CODE**

**13. ABSTRACT** *(Maximum 200 Words)*

The program has focused on the mechanics of deformation and fracture of a family of porous-matrix all-oxide continuous fiber ceramic composites (CFCCs). The activities have lead to substantive developments in the mechanistic understanding of: (i) mechanical properties and thermal stability of porous mullite/alumina matrices; (ii) strength, fracture resistance and notch sensitivity of porous-matrix composites; and (iii) stability and performance of oxide composites in gas turbine combustion environments. Models to describe the pertinent phenomena have been developed and validated.

| 14. SUBJECT TERMS | | | 15. NUMBER OF PAGES |
|---|---|---|---|
| | | | 16. PRICE CODE |
| 17. SECURITY CLASSIFICATION OF REPORT | 18. SECURITY CLASSIFICATION OF THIS PAGE | 19. SECURITY CLASSIFICATION OF ABSTRACT | 20. LIMITATION OF ABSTRACT |

temperature was designed and conducted. Models for these properties based on bonded particle aggregates have been calibrated. Upon combining the experimental and modeling results, predictions are made of the critical aging times at which damage tolerance is lost because of sintering at the particle junctions and the associated changes in mechanical properties. For an aging temperature of 1200°C, the critical time exceeds 10,000 hours for the mullite-rich mixtures.

## II. Controlling Mechanical Properties via Precursor-Derived Alumina

An assessment has been made of the utility of a precursor-derived alumina in controlling both the modulus and the toughness of mullite-rich porous matrices. Property changes have been probed through models of the mechanical behavior of bonded particle aggregates. The upper allowable limit on the concentration of precursor-derived alumina to ensure damage tolerance in a fiber composite lies in the range of 7–9%, depending on the mullite/alumina ratio in the particle slurry and the subsequent aging treatment. Values slightly below this limit yield composites that exhibit a desirable balance between fiber- and matrix-dominated properties.

## III. Notch Sensitivity of Ceramic Composites with Rising Fracture Resistance

A theoretical framework has been developed for the notched strength of ceramic composites that exhibit rising fracture resistance. It is based on established concepts of crack stability under stress-controlled loadings. Using a linear representation of the resistance curve (expressed in terms of an energy release rate), analytical solutions are obtained for the strength as well the amount of stable crack growth preceding fracture and the associated fracture resistance. Calculations have been performed for several test configurations commonly used for material characterization, including single- and double-edge notched tension, center-notched tension, and single edge-notched bending. The results reveal salient trends in strength with notch length and specimen geometry. An assessment of the theory has been made through comparison with experimental measurements on an all-oxide fiber composite. The utility of the theoretical results both for rationalizing the trends in measured notched strength and for guiding experimental studies of notch sensitivity have been demonstrated.

## IV. Strength and Notch Sensitivity of Porous-Matrix Oxide Composites

Effects of matrix strength on the notched and unnotched tensile properties of a family of porous-matrix oxide composites have been examined both experimentally and theoretically. Experiments were performed on three composites, distinguished from one another by the amount of binding alumina within the matrix. Increases in alumina concentration produce elevations in unnotched tensile and shear strengths, but the benefits are offset by an increase in notch sensitivity. The degree of notch sensitivity can be rationalized on the basis of a model that accounts for interactions between notch tip tensile and shear bands. The model predictions are cast in terms of the ratio of the notch length to a characteristic bridging length scale. These results, in turn, form the basis for an

analytical formula for notched strength, accounting for effects of elastic anisotropy and finite sample size. The utility of this formula in predicting notched strength has been illustrated. Issues associated with bridging law shapes and bridging length scales have been addressed. The effect of alumina concentration on notch sensitivity are rationalized in terms of its influence on the bridging length scale, dictated by the interplay between the unnotched tensile strength, the longitudinal Young's modulus, the degree of in-plane elastic anisotropy and the fracture energy. The net result is a decreasing bridging length scale and hence increasing notch sensitivity as the matrix is strengthened with alumina.

### V. Effects of Combustor Rig Exposure on a Porous-Matrix Oxide Composite

Effects of exposure in a laboratory combustor on microstructural stability and property retention of an all-oxide fiber-reinforced ceramic composite have been explored. The material consists of a porous mullite-alumina matrix and Nextel 720 fibers in an 8-harness satin weave. To assess the effects of matrix strength, two matrix conditions have been used, distinguished from one another by the amount of alumina added through precursor impregnation and pyrolysis (1.8% and 4.8%). In both cases, the dominant damage mode upon exposure involves interply delamination along the panel mid-plane. However, significant reductions in the rate and extent of cracking are obtained in the material with higher alumina content: a result of the higher delamination resistance. Mechanical tests performed on exposed specimens reveal a slight (10–20%) reduction in tensile strength along the fiber direction and a comparable increase in shear strength. These trends suggest some sintering of the matrix upon exposure. Examinations of fracture surfaces provide additional supporting evidence. Implications for long-term performance and strategies for imparting improvement in microstructural stability and delamination resistance have been elucidated.

## PAPERS PUBLISHED

M.A. Mattoni and F.W. Zok, "A Method for Determining the Stress Intensity Factor of a Single Edge-Notched Tensile Specimen," *Int. J. of Frac.*, **119**: L3-L8, 2003.

H. Fujita, G. Jefferson, F.W. Zok and R.M. McMeeking, "Mullite/Alumina Mixtures for use as Porous Matrices in Oxide Fiber Composites," *J. Am. Ceram. Soc.*, **87**, [2] 261-67, 2004.

J.R. Dryden and F.W. Zok, "Effective Conductivity of Partially Sintered Solids," *J. App. Phys.*, **95**, [1], 2004.

M.A. Mattoni and F.W. Zok, "Notch Sensitivity of Ceramic Composites with Rising Fracture Resistance," *J. Am. Ceram. Soc.*, **87**, 914-922, 2004.

H. Fujita, G. Jefferson, C.G. Levi and F.W. Zok, "Controlling Mechanical Properties of Porous Mullite/Alumina Mixtures via Precursor-Derived Alumina," *J. Am. Ceram. Soc.*, **88**, [2] 367-375, 2005.

M.A. Mattoni, J.Y. Yang, C.G. Levi and F.W. Zok, "Effects of Combustor Rig Exposure on a Porous-Matrix Oxide Composite," *Int. J. Applied Ceram. Tech.*, **2** [2], 133-140, 2005.

M.A. Mattoni and F.W. Zok, "Strength and Notch Sensitivity of Porous-Matrix Oxide Composites," *J. Am. Ceram. Soc.*, **88** [6] 1504-1513, 2005.

*International Journal of Fracture* **119:** L3–L8, 2003.


# A METHOD FOR DETERMINING THE STRESS INTENSITY FACTOR OF A SINGLE EDGE-NOTCHED TENSILE SPECIMEN

*M.A. Mattoni and F.W. Zok*
*Materials Department, University of California*
*Santa Barbara, CA 93106*
*e-mail: zok@engineering.ucsb.edu*

**Abstract.** A straightforward method for determining the stress intensity factor of a single edge-notched tensile specimen with unknown end conditions is presented. It involves the use of measured crack mouth opening displacements, coupled with existing solutions for stress intensity factors and crack opening displacements for uniform tensile loading and for pure bending. The use of the method is demonstrated through experiments on a porous matrix ceramic composite.

**1. Introduction.** The single edge-notched tensile (SENT) specimen is commonly used for measuring the fracture resistance of engineering materials. The pertinent existing solutions for stress intensity factors are based on two limiting idealizations of the conditions at the specimen ends where the force is transmitted from the testing machine to the specimen. In the first, the loading fixture is assumed to have no rotational stiffness and the *stress* is distributed uniformly across the specimen ends. To achieve this condition, the specimen length, H, must be significantly greater than the width, W, and the fixture must have a mechanism for allowing rotation with minimal constraint. The latter condition is usually achieved by pin loading. The stress intensity factor for this case is given by standard handbook solutions, e.g., Tada *et al.* (1985). In the second, the loading fixture is assumed to be rigid and the axial *displacements* are uniform across the specimen end. In this case, a bending moment is induced at the specimen ends, in addition to the applied tension. To achieve these conditions, a significant length of the specimen at the ends must be clamped using stiff grips. Pertinent solutions for the stress intensity factor for the uniform displacement condition have been developed by Marchand *et al.* (1986), Blatt *et al.* (1994), John *et al.* (1995), and John and Rigling (1998).

The differences in the stress intensity factors in the two cases are usually significant. For example, for a test specimen with aspect ratio H/W=2 and a crack length a/W=0.5, the normalized stress intensity factors for the uniform stress and the uniform displacement conditions are $K/\sigma\sqrt{\pi a} = 2.83$ and 1.29, respectively: a difference of more than a factor of 2. It is expected that stress intensity factors for test

conditions that yield intermediate levels of constraint will not be represented adequately by either of the two limiting cases.

Here we present a straightforward method for determining stress intensity factors for the SENT geometry under conditions in which *neither* of the two limiting conditions are obtained. The development of the method has been motivated by the need to assess fracture resistance of ceramic composites that are currently being fabricated in small quantities and for which the test specimens are necessarily small. Often this precludes the use of long tensile specimens for the purpose of gripping long sections near the ends and achieving uniform displacement conditions. Furthermore, compliant end tabs are usually used to ensure a uniform pressure distribution along the gripped surface and to prevent crushing. Such tabs reduce the grip stiffness and compromise the goal of a uniform displacement condition. Pin loading configurations are also impractical because of the potential for bearing failure. This is due to the high stresses needed to initiate crack tip failure coupled with the low crushing strength of the matrix in the composites of interest. As a result, the uniform stress condition is also difficult to achieve.

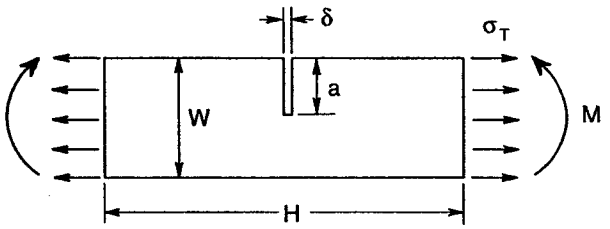


*Figure 1.* A schematic showing the uniform tensile stress and the bending moment at the ends of an SENT specimen. Note that the stress intensity factor from the moment is negative.

**2. Analysis.** When neither of the limiting end conditions is achieved, the stresses at the specimen ends can be partitioned into two components: (i) a uniform tensile stress, $\sigma_T$, equal to the average (measured) stress, and (ii) a bending stress, $\sigma_B$, proportional to $\sigma_T$, but otherwise of unknown magnitude (Fig. 1). The stress intensity factor associated with these two stress components is:

$$K = F_T(a/W)\,\sigma_T\sqrt{\pi a} - F_B(a/W)\,\sigma_B\sqrt{\pi a} \equiv F_E(a/W)\,\sigma_T\sqrt{\pi a} \qquad (1)$$

where $F_T(a/W)$ and $F_B(a/W)$ are the usual non-dimensional functions for tension and bending given in handbooks (e.g. Tada *et al.*, 1986), and $F_E(a/W)$ is the function that

characterizes the normalized stress intensity factor in the present test configuration. The corresponding crack mouth opening displacement, $\delta$, is:

$$\delta = V_T(a/W)\frac{4\sigma_T a}{E} - V_B(a/W)\frac{4\sigma_B a}{E} \equiv V_E(a/W)\frac{4\sigma_T a}{E} \qquad (2)$$

where E is the plane strain Young's modulus, the functions $V_T(a/W)$ and $V_B(a/W)$ are obtained from handbooks, and $V_E(a/W)$ characterizes the normalized crack opening in the test configuration. Rearranging Eqn. 2 yields an expression for the bending stress:

$$\frac{\sigma_B}{\sigma_T} = \frac{V_T}{V_B} - \frac{1}{V_B}\left(\frac{\delta E}{a\sigma_T}\right) \qquad (3)$$

Combining Eqn. (1) and (3) gives the stress intensity factor as:

$$F_E = \frac{K}{\sigma_T\sqrt{\pi a}} = \left(F_T - \frac{F_B V_T}{V_B}\right) + \left(\frac{F_B}{V_B}\right)\left(\frac{\delta E}{4\,a\sigma_T}\right) \qquad (4)$$

This result indicates that the stress intensity factor can be obtained from a combination of the known functions and the normalized crack mouth opening displacement, $V_E = \delta E/a\sigma_T$, the latter being obtained experimentally.

**3. Experiments.** The analysis was assessed through a series of SENT tests on a porous matrix ceramic composite. The composite consisted of Nextel 720 fiber cloth in an 8 harness satin weave and a porous mullite-alumina matrix. The matrix was introduced in two steps: (i) pressure-assisted infiltration of a mullite-alumina slurry through the fiber preform, and (ii) impregnation and pyrolysis of an $Al_2Cl(OH)_5$ solution (an alumina precursor). Processing details were essentially identical to those described by Mattoni *et al.* (2001), with two exceptions. First, the concentration of the precursor solution was increased to give a volumetric yield of $\approx 8.3\%$ (compared with 3% in previous studies). The more concentrated solution allows a prescribed matrix density to be achieved with fewer impregnation and pyrolysis cycles. In the present study, 4 such cycles were used, yielding a final matrix porosity of 31.9%. Second, to prevent segregation of the precursor during drying, the panels were gelled immediately after precursor impregnation by immersing them in a $NH_4OH$ environment for 6 hours. The absence of segregation was confirmed through a series of matrix hardness measurements at various points through the plate thickness.

The aspect ratio of the gauge section of the SENT specimens was fixed at H/W=2.1. The width of all specimens was W=24 mm whereas the notch length was varied over the range a/W=0.35–0.65. To facilitate gripping, thin fiberglass tabs were adhesively attached to the ends over a length of approximately 4 mm. The specimens were instrumented with a displacement gauge at the crack mouth and a crack gauge at the notch tip. Corroborating measurements of crack length were obtained through direct optical observations of the notch tip region using a stereomicroscope.

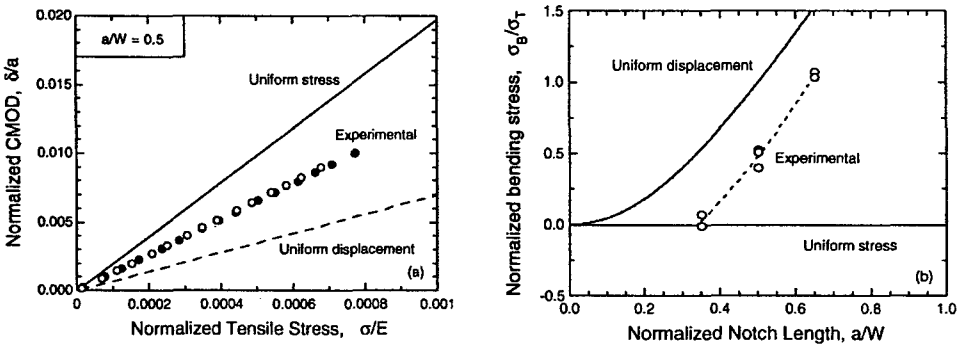


*Figure 2.* Effects of end condition on (a) the CMOD response and (b) the bending stress.

**Table I Functions for Single Edge-Notched Specimen under Uniform Tension and Bending (from Tada *et al.* 1985).**

| | F(a/W) | V(a/W) |
|---|---|---|
| Tension | $\sqrt{\frac{2W}{\pi a}\tan\left(\frac{\pi a}{2W}\right)}\,\frac{0.752+2.02(a/W)+0.37\left(1-\sin\left(\frac{\pi a}{2W}\right)\right)^3}{\cos\left(\frac{\pi a}{2W}\right)}$ | $\frac{1.46+3.42\left(1-\cos\frac{\pi a}{2W}\right)}{\left(\cos\frac{\pi a}{2W}\right)^2}$ |
| Bending | $\sqrt{\frac{2W}{\pi a}\tan\left(\frac{\pi a}{2W}\right)}\,\frac{0.923+0.199\left(1-\sin\left(\frac{\pi a}{2W}\right)\right)^4}{\cos\left(\frac{\pi a}{2W}\right)}$ | $\frac{1.46+3.42\left(1-\cos\frac{\pi a}{2W}\right)}{\left(\cos\frac{\pi a}{2W}\right)^2}$ |

The variation in CMOD with applied stress for one specimen configuration is plotted in Fig. 2(a). Combining measurements of this type with Eqn. (3) and the functions in Table I yields the normalized bending stresses plotted in Fig. 2(b). Also shown for comparison in these figures are the predicted values for uniform stress and uniform displacement conditions, using solutions in Tada *et al.* (1985) and John and Rigling (1985). The experimental results lie between the predictions for the two limiting cases, as expected. Evidently the bending stress is small for a/W=0.35 but subsequently increases rapidly with increasing a/W.

The preceding results were combined with the load and crack length measurements and the result in Eqn. (4) to obtain the initiation fracture toughness, $K_o$, as well as the fracture resistance, $K_R$, subsequent to the onset of cracking. The results are plotted in Fig. 3. The initiation toughness is independent of the notch length, at a value $K_o$=7.8±0.7 MPa$\sqrt{m}$. The fracture resistance curves increase linearly with crack extension, at a rate independent of the initial notch length. The consistencies in $K_o$ and $K_R$ between specimens of varying notch length provide confidence that the present method of determining the pertinent stress intensity factors is indeed correct.

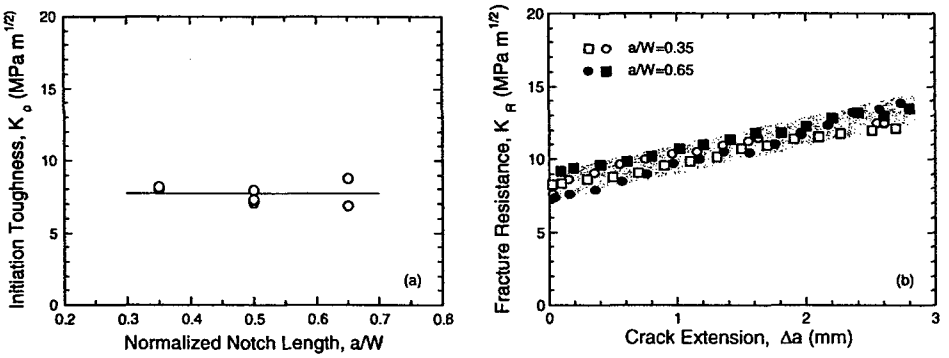


*Figure 3.* Effects of notch length on (a) the initiation fracture toughness and (b) the fracture resistance curve.

**4. Concluding Remarks.** The present method for determining the stress intensity factor provides flexibility in the test configurations used for determining fracture resistance. Specifically, it provides latitude in the degree of constraint exerted by the grips without compromising the integrity of the fracture resistance measurements. In addition to its use in test configurations that are known to experience intermediate end conditions, the method would be useful for checking whether a particular

targeted end condition, either uniform stress or uniform displacement, has indeed been achieved.

**Acknowledgements**: Funding for this work was provided by the Air Force Office of Scientific Research under Contract number F49620-02-1-0128, monitored by Dr. B.L. Lee.

## References

Blatt, D., John, R., Coker, D., 1994. Stress Intensity Factor and Compliance Solutions for a Single Edge Notched Specimen with Clamped Ends. *Engineering Fracture Mechanics*, 47, 521–532.

John, R., Kaldon, S.G., Johnson, D.A. and Coker, D., 1995. Weight Function for a Single Edge Cracked Geometry with Clamped Ends. *International Journal of Fracture*, 72, 145–158.

John, R. and Rigling, B., 1998. Effect of Height to Width Ratio on K and CMOD Solutions for a Single Edge Cracked Geometry with Clamped Ends. *Engineering Fracture Mechanics*, 60, 147–156.

Marchand, N., Parks, D.M., and Pelloux, R.M., 1986. $K_t$ Solutions for Single Edge Notch Specimens under Fixed End Displacements. *International Journal of Fracture*, 31, 53–65.

Mattoni, M.A., Yang, J.Y., Levi, C.G., and Zok, F.W., 2001. Effects of Matrix Porosity on the Mechanical Properties of a Porous-Matrix All-Oxide Ceramic Composite. *Journal of the American Ceramic Society*, 84, 2594–2602.

Tada, H., Paris, P.C., and Irwin, G.R., 1985. The Stress Analysis of Cracks Handbook. Del Research Corporation, St. Louis, MO.

journal

J. Am. Ceram. Soc., 87 [2] 261–67 (2004)

# Mullite/Alumina Mixtures for Use as Porous Matrices in Oxide Fiber Composites

Hiroki Fujita,[†] George Jefferson,[‡] Robert M. McMeeking[*,§] and Frank W. Zok[*,†]

Materials Department, Department of Mechanical and Environmental Engineering, University of California, Santa Barbara, California 93106

Department of Aeronautics and Astronautics, Air Force Institute of Technology, Wright Patterson Air Force Base, Ohio 45433

**Weakly bonded particle mixtures of mullite and alumina are assessed as candidate matrixes for use in porous matrix ceramic composites. Conditions for the deflection of a matrix crack at a fiber-matrix interface are used to identify the combinations of modulus and toughness of the fibers and the matrix for which damage-tolerant behavior is expected to occur in the composite. Accordingly, the present study focuses on the modulus and toughness of the particle mixtures, as well as the changes in these properties following aging at elevated temperature comparable to the targeted upper-use temperature for oxide composites. Models based on bonded particle aggregates are presented, assessed, and calibrated. The experimental and modeling results are combined to predict the critical aging times at which damage tolerance is lost because of sintering at the particle junctions and the associated changes in mechanical properties. For an aging temperature of 1200°C, the critical time exceeds 10 000 h for the mullite-rich mixtures.**

## I. Introduction

THE USE of porous matrixes to enable damage tolerance in continuous-fiber ceramic composites (CFCCs) has emerged as a new paradigm in high-performance materials.[1] The concept obviates the need for fiber coatings to affect crack deflection, thereby providing opportunities for lower-cost manufacturing relative to that of conventional coated-fiber systems. Furthermore, on selection of all-oxide constituents, the long-term durability requirements in the targeted high-temperature applications can be met.

Although the porous matrix concept offers new opportunities for the development of damage-tolerant CFCCs, it also presents challenges in the design and synthesis of microstructures that meet the opposing property requirements placed on the matrix. That is, in the absence of fiber coatings, the matrix must be sufficiently weak to enable damage tolerance under fiber-dominated loadings, yet retain adequate strength to ensure acceptable off-axis properties. In principle, the combination of properties can be tailored through changes in the state of the matrix. For instance, improvements in the interlaminar strength and off-axis in-plane strength can be obtained by reducing the matrix porosity; however, these improvements come at the expense of a reduction in the damage tolerance under fiber-dominated loadings. These offsetting effects suggest the existence of an optimum in matrix properties at which a prescribed *balance* of properties is attained. However, the relationships between matrix structure and composite performance are understood presently at only a rudimentary level. Consequently, the pathway to optimization remains ill defined.

The objective of the present article is to elucidate some of the connections between composition, microstructure, and mechanical properties of a candidate family of porous matrices, with emphasis on the conditions needed to enable damage tolerance in fiber-dominated loadings. Effects of the matrix on off-axis properties are addressed elsewhere.[2] The work stems from concurrent activities on the development of all-oxide CFCCs for use in future gas-turbine systems.[3–6] Because of the interest in mullite/alumina fibers for use in these applications, the present article focuses specifically on mullite/alumina matrixes. These matrices are both chemically compatible with the fibers and exhibit mechanical characteristics that make them attractive for use in CFCCs. A perspective based on the mechanics of crack deflection is used to guide the experimental measurements and provide a framework for interpreting the property values. Consideration is given to the stability of the properties following long-term exposure at elevated temperature, comparable to the targeted upper use temperature for oxide CFCCs.

We present a review of the mechanics of crack deflection at a fiber-matrix interface. The results are used to identify the critical combination of matrix modulus and matrix toughness needed for deflection and to motivate the subsequent mechanical measurements. The nature of the candidate matrix system, the processing route, and the measurement procedures are described. Results for modulus and toughness are presented, along with predictions of these properties from models of bonded-particle aggregates. Finally, we address the implications on crack deflection in CFCCs. For this purpose, calibrated models are used to establish the critical aging time at which the crack deflection condition is no longer satisfied and thus the damage tolerance is lost.

## II. Mechanics of Crack Deflection

As a minimum requirement for damage tolerance in CFCCs, cracks in the matrix must either arrest at or deflect into the fiber/matrix interface rather than penetrate into the fibers. The conditions that satisfy this requirement are obtained from the He and Hutchinson[7] diagram shown in Fig. 1. Crack arrest or deflection is predicted to occur when the ratio of interface toughness, $\Gamma_i$, to fiber toughness, $\Gamma_f$, falls below the corresponding ratio of energy release rates, $G_d/G_p$, associated with deflection into the boundary and penetration into the fiber. The critical ratio is controlled by the elastic mismatch parameter:

$$\alpha \equiv \frac{(\bar{E}_f - \bar{E}_m)}{(\bar{E}_f + \bar{E}_m)} \tag{1}$$

T. A. Parthasarathy—contributing editor

Manuscript No. 10088. Received March 28, 2003; approved September 12, 2003.
Funding for this work was provided by the Air Force Office of Scientific Research under Contract No. F49620-02-1-0128, monitored by Dr. B. L. Lee, as well as a gift from NGK Insulators.

*Member, American Ceramic Society.
†Materials Department.
‡Department of Aeronautics and Astronautics.
§Department of Mechanical and Environmental Engineering.

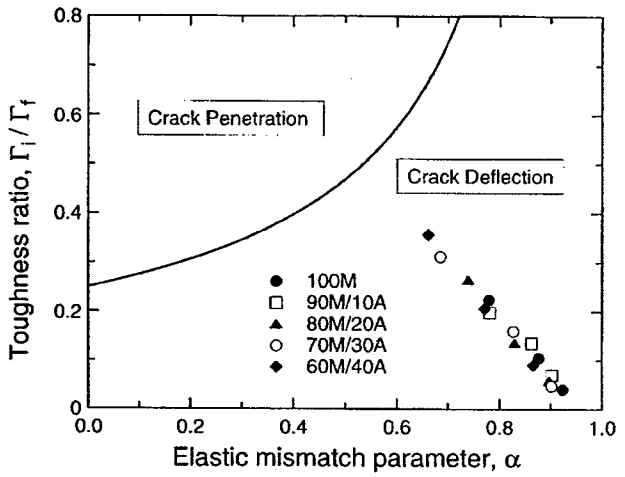


**Fig. 1.** Conditions for crack deflection at a fiber-matrix interface (solid line). Experimental measurements from this study are superimposed (symbols). The latter assume a toughness ratio $\omega \equiv \Gamma_i/\Gamma_m = 1$ and fiber properties $\Gamma_f = 15$ J/m$^2$ and $E_f = 260$ GPa.

where $\bar{E}$ is the plane strain modulus, and the subscripts $f$ and $m$ refer to fiber and matrix, respectively. For porous matrix systems, $\alpha$ takes on relatively high values (>0.5), and hence the allowable toughness ratio is also relatively high. In the systems of present interest, the matrix and fiber constituents are essentially the same, i.e., mullite/alumina, and hence the nature of bonding at the fiber-matrix interface is similar to that between particles in the matrix. Consequently, the interface toughness is expected to be proportional to the matrix toughness: $\Gamma_i = \omega\Gamma_m$ where $\omega$ is a nondimensional parameter of order unity. Because of the reduced efficiency of particle packing along the fiber surfaces,[8] it is expected that $\Gamma_i < \Gamma_m$ such that $\omega < 1$. For conservative design, $\omega$ is taken to be 1.

The critical combination of matrix and fiber properties are obtained in the following way: For $\alpha \geq 0$, the energy release rate ratio, $G_d/G_p$, can be represented by an approximate empirical equation:

$$\frac{G_d}{G_p} = \frac{1}{4(1-\alpha)^{0.9}} \tag{2}$$

This equation is an exact representation of the He and Hutchinson[7] criterion at $\alpha = 0$ and has an error ≤4% over the range $0 \leq \alpha \leq 0.95$. On setting $G_d/G_p = \Gamma_i/\Gamma_f$ in Eq. (2) and combining the result with Eq. (1), the deflection condition is re-expressed as follows (Here the Poisson's ratios of the fiber and the matrix are assumed to be the same. Consequently, the plane strain modulus ratio $\bar{E}_f/\bar{E}_m$ can be replaced with Young's modulus ratio $E_f/E_m$).

$$\Sigma \equiv 0.134\left(\frac{\Gamma_f}{\Gamma_m}\right)\left(1+\frac{E_f}{E_m}\right)^{0.9} > \omega \tag{3}$$

Here $\Sigma$ is a nondimensional parameter that characterizes the propensity for crack deflection. It identifies the critical combination of $\Gamma_i\Gamma_f$ and $E_m/E_f$ needed to cause deflection.

In light of this prediction, the subsequent experimental study focuses on the matrix properties $\Gamma_m$ and $E_m$, with a view to assessing whether the crack-deflection condition in Eq. (3) is satisfied when the matrix is combined with the specified fiber, notably Nextel 720™ (3M Corp., St. Paul, MN).

## III. Materials and Test Procedures

Two generic matrix topologies have previously been explored.[6] The first involves the use of particle mixtures of mullite and alumina and relies on the more rapid sintering kinetics of alumina to bond the network together. The second is based on the use of alumina precursor liquids in conjunction with either pure mullite particles or mullite/alumina particle mixtures. The latter approach has the advantage that it does not compromise the contiguity of the particle network and should yield a more stable pore structure. But it comes at the expense of additional steps in material processing, beyond that associated with particle mixtures alone. The present paper explores the former topology (based on particle mixtures); the latter is developed elsewhere.[9]

Porous mullite-alumina compacts were fabricated using a pressure infiltration technique. The compositions ranged from pure mullite to 60% mullite + 40% alumina by volume. The compositions are henceforth designated by the percentages of mullite and alumina, i.e., 80M/20A denotes 80% mullite + 20% alumina. A small number of pure alumina specimens were fabricated also, for the purpose of assessing the efficacy of the mullite network in inhibiting shrinkage associated with sintering of alumina in the mixed compacts. The mullite particulates were mullite (MU-107, Showa Denko K.K., Tokyo, Japan). The size distribution was rather broad, characterized by a mean diameter $d_{avg} = \sim 1$ μm and diameters at the 10th and 90th percentiles of the distribution of $d_{10} = 0.4$ μm and $d_{90} = 2.3$ μm, respectively. The alumina particulates (AKP-50, Sumitomo Chemical, Tokyo, Japan), had size distribution characterized by $d_{avg} = \sim 0.2$ μm, $d_{10} = 0.1$ μm, and $d_{90} = 0.3$ μm. An aqueous slurry containing the powder mixture was prepared and vacuum-infiltrated into a mold with dimensions 10 mm × 50 mm × 90 mm. The green compacts were dried and sintered at 900°C for 2 h to promote partial sintering at the particle junctions. The compacts were machined into mechanical test specimens and the specimens given a 2 h heat treatment at 1200°C. To assess the stability of the microstructure under conditions that mimic the targeted service conditions for oxide CFCCs, some test specimens were given additional aging treatments of 100 h or 1000 h at 1200°C.

The porosity, $P$, of the compacts was determined from measurements of mass, both in air and immersed in water.[10] The pertinent densities of the constituent powders needed for calculating porosity were measured using a pycnometer. The measurements on the powders were performed after the powders had been subjected to the same heat treatments as those of the compacts. Even after the longest aging treatments, the powders had not sintered together and remained free flowing. The measurements revealed a very slight increase in the density of the pure mullite powder, from 3.14 to 3.24 g/cm$^3$, as the aging time increased from 2–1000 h. The associated mechanism is unknown, although the values are in broad agreement with those reported in the literature.[11] In contrast, the alumina powder density remained unchanged over the same range of aging time, at 4.01 ± 0.01 g/cm$^3$.

The Young's modulus of the fired compacts was measured using strain-gauged flexure specimens, 5 mm × 5 mm × 50 mm long, loaded in four-point bending. The inner and outer loading spans were 20 and 40 mm, respectively. The toughness was obtained from work of fracture measurements on chevron-notched bend specimens[12] with the same dimensions, but loaded in three-point bending and instrumented with an LVDT to measure load-point displacement. In all cases, the crack grew stably across the specimen cross section. The fracture surfaces were examined subsequently via scanning electron microscopy (SEM).

Henceforth, the ˜ symbol is used to denote properties of the porous compacts, i.e., $\tilde{E}$ and $\tilde{\Gamma}$ for modulus and toughness, respectively; the subscripts $A$ and $M$ are used to denote pure alumina and pure mullite; and the absence of a subscript implies a particle mixture.

## IV. Pure Mullite

### (1) Experimental Results

The variation in the porosity of the pure mullite compacts with aging time is plotted in Fig. 2. Despite the slight change in powder density, the porosity of the compacts remains essentially constant over the entire range of aging times, within 0.2% of its initial value, $P_o$.

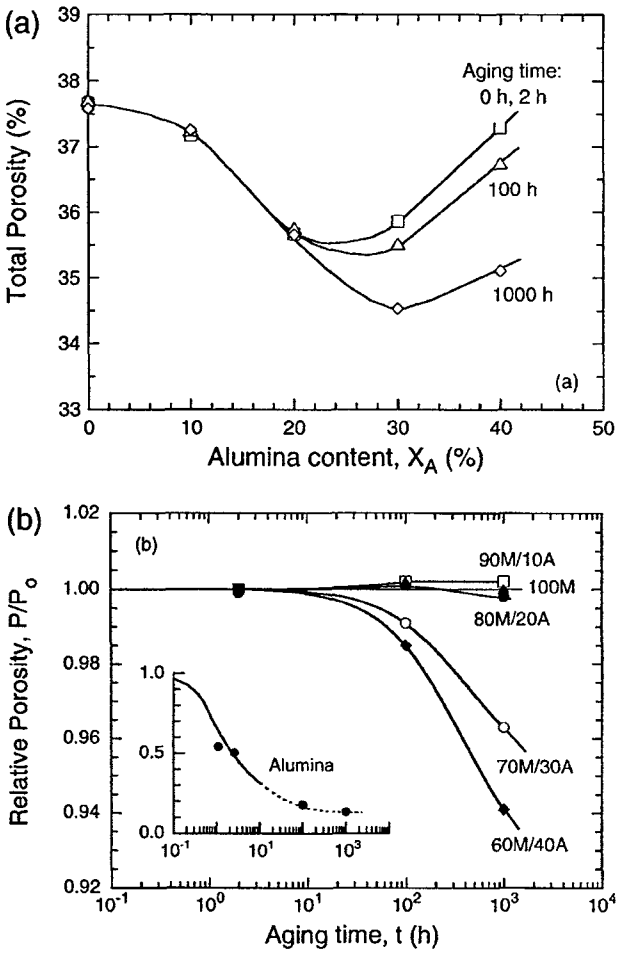


**Fig. 2.** (a) Effects of composition and aging time on compact porosity. The data for 0 h and 2 h are virtually identical to one another and are indistinguishable on the graph. (b) Results in (a), normalized by the initial (green) porosity at the same composition. The solid line for alumina in the inset was obtained by dilatometry, the symbols are based on the Archimedes measurements, and all other lines are simply curve fits through the discrete data points.

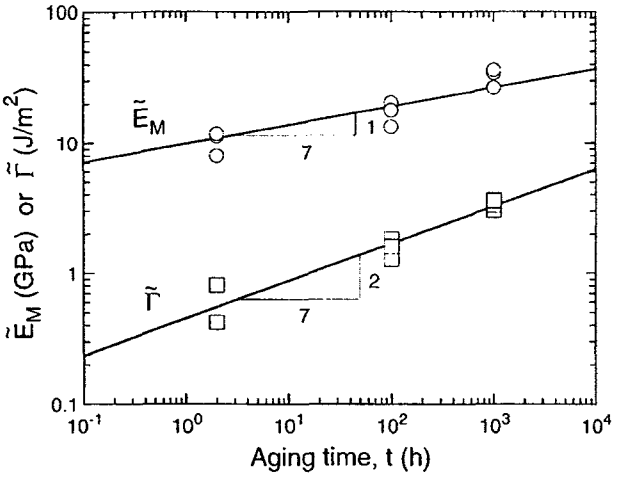


**Fig. 3.** Effects of aging time on Young's modulus and toughness of pure mullite. Power law fits of the experimental data yield exponents of 0.18 ± 0.03 and 0.28 ± 0.03 for modulus and toughness, respectively, in accord with those predicted for surface diffusion controlled sintering, notably 0.143 and 0.286.

Both the modulus and the toughness of the mullite compacts increase appreciably with aging time, by a factor of ~3–4 (Fig. 3). These property changes indicate sintering at the particle junctions, but the absence of porosity change implies a mechanism that does not involve movement of the particle centers. Possible mechanisms include transport of matter from surface sources via either surface diffusion, lattice diffusion, or vapor transport.[13] The dominant transport mechanism is inferred from sintering models and the mechanical measurements in the manner described in the following section.

SEM observations of the fracture surfaces reveal only a small number of well-defined broken junctions (Figs. 4(a) and (b)). These are somewhat more prevalent after the longest aging time because of the increase in junction size. The small number of such junctions indicates that fracture normally occurs "cleanly" without appreciable crack meandering, suggesting a low fracture energy. It also precludes direct measurement of junction size.

### *(2) Modeling*

When the junction radius, $a$, is much smaller than the particle radius, $R$, junction growth owing to sintering follows a power law of the form:[13,14]

$$\frac{a}{R} = \left(\frac{t}{t_R}\right)^{\frac{1}{n}} \tag{4}$$

where $t$ is sintering time, $t_R$ is a reference time and $n$ is a constant; both $t_R$ and $n$ depend on the transport mechanism. Sintering models yield values of $n = 3$ for vapor transport, $n = 5$ for lattice diffusion, and $n = 7$ for surface diffusion.

In turn, for monosized spherical particles with small junctions ($a/R << 1$), the Young's modulus of a bonded particle aggregate scales linearly with junction radius in accordance with:[15,16]

$$\frac{\tilde{E}}{E_p} = \xi\left(\frac{zD}{2\pi}\right)\left(\frac{a}{R}\right)g(\nu) \tag{5}$$

where $E_p$ and $\nu$ are the Young's modulus and Poisson's ratio of the particles; $z$ is the particle coordination number (~6 for random packing); $D$ is the relative packing density; $\xi$ is a numerical parameter; and $g(\nu)$ is given by

$$g(\nu) = \frac{5 - 4\nu}{(1 - \nu^2)(5 - 3\nu)} \tag{6}$$

For values of $\nu$ in the range $0 \le \nu \le 0.25$, $g(\nu) = 1 \pm 0.004$; the dependence on $\nu$ is extremely small and is subsequently neglected. This result, with $\xi = 1$, was derived by Walton,[15] using Hertzian contact mechanics to describe junction stiffness and assuming a uniform aggregate strain. A more rigorous model that accounts for finite junction size and multiparticle interactions yields results in the domain of small junctions ($a/R \le 0.3$) that are consistent with Eq. (5) when $\xi$ is taken to be ~0.76 (simulation of modulus has been performed for two limiting cases: assuming that the torsional stiffness of the junctions is either zero or infinite.[16] The two sets of results are fit well by Eq. (5), using $\xi = 0.65$ and 0.88, respectively. The average of these, $\xi = 0.76$, is used in the present work). Combining Eqs. (4) and (5) and taking $g(\nu) = 1$ yields the time-dependence of the modulus:

$$\frac{\tilde{E}}{E_p} = 0.76\left(\frac{zD}{2\pi}\right)\left(\frac{t}{t_R}\right)^{\frac{1}{n}} \tag{7}$$

The relationship between toughness and junction radius for a bonded particle aggregate has been obtained from numerical simulations of fracture, using a technique based on the discrete element method (DEM). Details of the method and its implementation are presented elsewhere.[17] Briefly, a computer-simulated sintering algorithm is used to generate a random three-dimensional array of spherical particles with a prescribed junction radius. The simulated aggregates consist of ~1000 particles. A crack is defined by a plane separating particles that have had the junctions

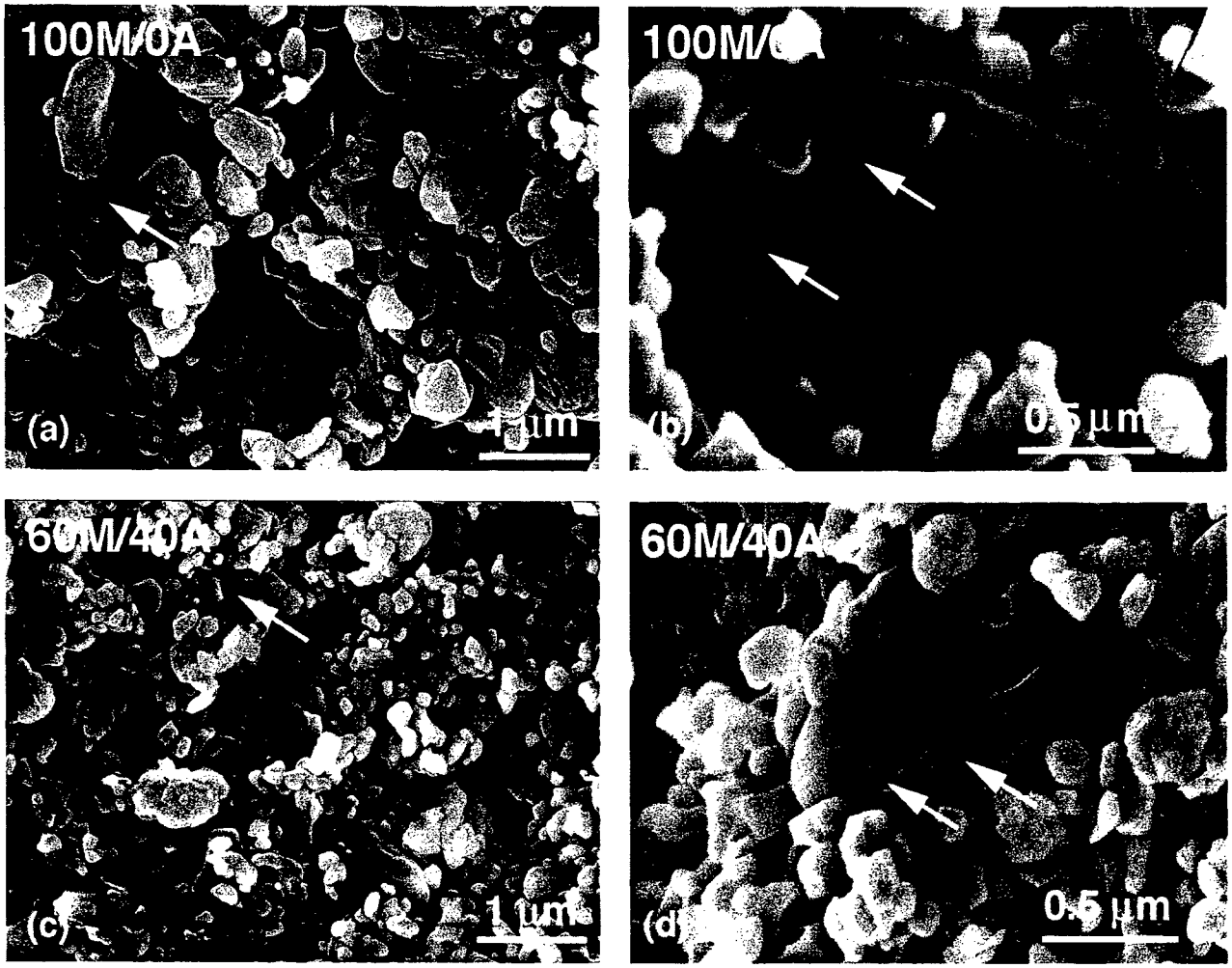


**Fig. 4.** Fracture surfaces of compacts that cover the range of alumina content, from 0% (a, b) to 40% (c, d), following a 1000 h aging at 1200°C. Examples of fractured particle junctions are highlighted by the arrows.

between them broken. The simulation proceeds by incrementally increasing the remote displacement while allowing the junctions at the crack tip to fail when the junction stress reaches a critical value, $\sigma_c$,

$$\sigma_c = 2\sqrt{\frac{E_p\Gamma_j}{\pi a}} \tag{8}$$

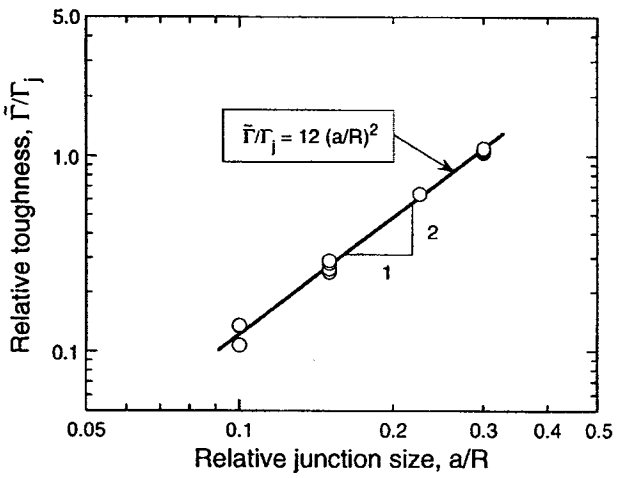


**Fig. 5.** Results of fracture simulations based on the discrete element method.

where $\Gamma_j$ is the intrinsic junction toughness. The results of the simulations (Fig. 5) are well described by

$$\frac{\tilde{\Gamma}}{\Gamma_j} = 12\left(\frac{a}{R}\right)^2 \tag{9}$$

Combining Eqs. (4) and (9) yields the time dependence of the toughness:

$$\frac{\tilde{\Gamma}}{\Gamma_j} = 12\left(\frac{t}{t_R}\right)^{\frac{2}{n}} \tag{10}$$

The predictions of modulus and toughness are compared with the experimental measurements in Fig. 4. The best correlations are obtained by taking $n = 7$ in Eqs. (7) and (10). The inference is that junction growth occurs predominantly by surface diffusion. For this mechanism, the reference time is given by[13]

$$t_R = \frac{kTR^4}{112\delta_s D_s \gamma \Omega} \tag{11}$$

where $k$ is Boltzman's constant, $T$ is absolute temperature, $\delta_s$ is the effective surface thickness, $D_s$ is the surface diffusion coefficient, $\gamma$ is the surface energy ($\approx 1$ J/m$^2$), and $\Omega$ is the molecular volume ($2.2 \times 10^{-28}$ m$^3$ for mullite).

A further assessment of the models was made in the following way: The numerical values of the various parameters for mullite

are known, with the exception of the junction toughness $\Gamma_j$ and the effective surface diffusivity $\delta_S D_S$. The diffusivity was inferred from the modulus data by equating the proportionality constant obtained from a 1/7 power law fit of the experimental measurements (Fig. 3) with the value predicted by Eq. (7). This yields $\delta_S D_S = 3.8 \times 10^{-30}$ m$^3$/s. The junction toughness was then obtained by equating the proportionality constant obtained from a 2/7 power law fit of the toughness measurements with the value predicted by Eq. (9), making use of the diffusivity inferred from the modulus measurements. The result is $\Gamma_j \approx 3$ J/m$^2$. This value is only slightly higher than the surface energy contribution, $\Gamma = 2\gamma \approx 2$ J/m$^2$, and well below the toughness of bulk polycrystalline mullite, $\Gamma \approx 20$–$30$ J/m$^2$.[11] The latter toughness has significant contributions from crack tilting and twisting and associated step formation when cracks propagate by transgranular cleavage.[18] This mechanism is not operative at the particle junctions because the particles themselves are single crystals, and the junctions between them are essentially grain boundaries.

## V. Mullite/Alumina Mixtures

### *(1) Experimental Results*

The physical properties of the mullite/alumina mixtures are summarized in Fig. 2. The initial porosity exhibits a shallow minimum at $X_A \approx 0.2$–$0.3$, a consequence of the slight size difference of the two particle types (Fig. 2(a)). However, the minimum porosity is only ~2% lower than that of pure mullite. For moderate alumina content, $X_A \leq 0.2$, the porosity remains extremely stable during aging, within 0.5% of $P_o$. For higher values ($X_A \geq 0.3$), the porosity diminishes during aging. The transition occurs near the expected percolation threshold, i.e., for monosized spheres with random dense packing, the threshold is predicted to be at ~0.25.[19] Interestingly, even beyond the threshold ($X_A > 0.25$), the porosity change occurs remarkably slowly. For example, for $X_A = 0.4$, the porosity reduction is ~6% of $P_o$ after a 1000 h aging. By comparison, pure alumina attains this porosity reduction after only 10 min at the same temperature (inset of Fig. 2(b)). The results demonstrate that the mullite network is effective in inhibiting densification even for relatively large amounts of sinterable phase, significantly beyond the percolation threshold.

For each aging treatment, the modulus increases approximately linearly with $X_A$ (Fig. 6(a)) at a rate characterized empirically by

$$\tilde{E} = \tilde{E}_M(1 + \beta X_A) \tag{12}$$

where $\beta \approx 2$–$3$. The increase is caused in part to the difference in particle moduli: $E_M = 200$ GPa vs. $E_A = 400$ GPa. But a rule-of-mixtures prediction based on modulus difference alone yields a lower modulus increase, notably:

$$\beta = \frac{E_A}{E_M} - 1 \approx 1 \tag{13}$$

The disparity is attributed to the larger junction sizes at the alumina-alumina and alumina-mullite contacts, relative to mullite-mullite, because of the more rapid sintering of alumina. Both features are incorporated in the model presented in the following section. Similar empirical trends are obtained in toughness, characterized by

$$\tilde{\Gamma} = \tilde{\Gamma}_M(1 + \gamma X_A) \tag{14}$$

where $\gamma \approx 2$.

The fracture surfaces of the mixed particle compacts are similar to those of pure mulllite in that there is little evidence of broken junctions even after the longest aging time. Some examples are shown in Figs. 4(c) and (d).

### *(2) Modeling*

The preceding models for junction growth and associated property changes in monophase aggregates have been extended to mullite-alumina mixtures. Here, three junction types are present: alumina-alumina (AA), alumina-mullite (AM), and mullite-mullite (MM). The modeling approach involves an averaging of the pertinent junction property, weighted by the number fraction of the associated junction type, to obtain the corresponding aggregate property. For simplicity, the alumina and the mullite particles are assumed to be the same size and arranged randomly in the mixture. A rudimentary statistical analysis yields the junction fractions, $f$:

$$f_{AA} = X_A^2 \tag{15a}$$

$$f_{MM} = (1 - X_A)^2 \tag{15b}$$

$$f_{AM} = 2X_A(1 - X_A) \tag{15c}$$

A model for the Young's modulus of the two-phase mixtures has been derived following an approach similar to that of Walton[15] for monophase aggregates, making appropriate changes to reflect differences in junction characteristics: (i) The description of junction stiffness is modified to account for the moduli of the particles on either side of the junction. For dissimilar particle junctions, the junction stiffness in the Hertzian limit is proportional to $2\lambda/(1 + \lambda)$ where $\lambda = E_A/E_M$.[20] (ii) The junction stiffness is further proportional to the junction radius. In light of the relative sintering rates of alumina and mullite, the radii of the three junction types are expected to rank as $a_{AA} > a_{AM} > a_{MM}$. (iii) The area of the alumina-mullite junction is assumed to be the average of the areas of the alumina-alumina and mullite-mullite junctions. This result can be expressed in nondimensional form as $a_{AM}/a_{MM}$

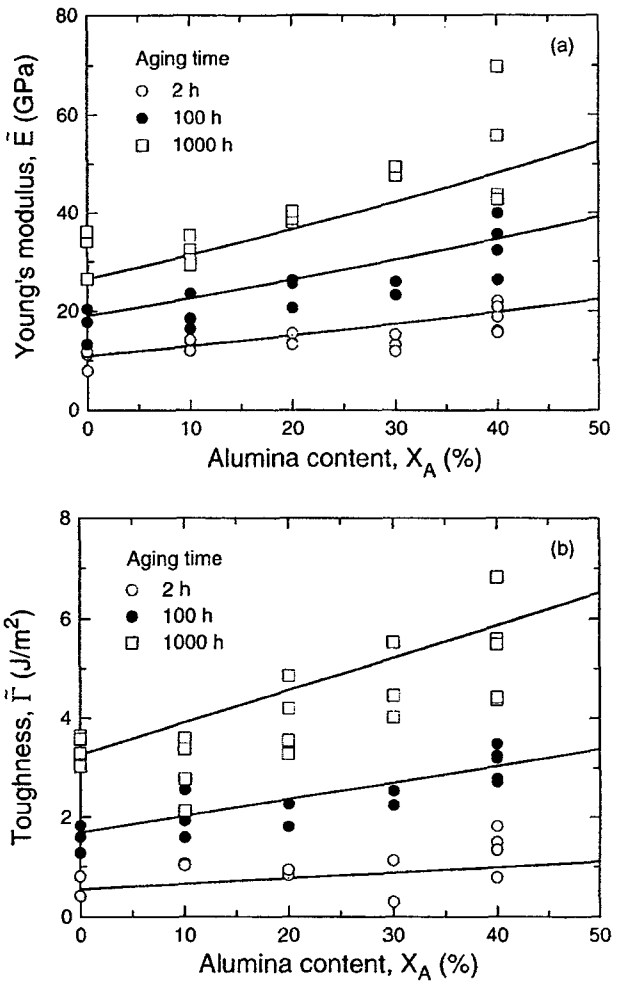


**Fig. 6.** Effects of composition and aging time on (a) Young's modulus and (b) toughness. Solid lines are model predictions (Eqs. (16) and (18)), with $\lambda = 2$, $\eta = 3$ and $\Psi = 1$.

$= \sqrt{(1+\eta)/2}$ where $\eta$ is a junction area ratio, defined by $\eta \equiv (a_{AA}/a_{MM})^2$. (iv) The modulus is determined from the mean junction stiffness, weighted by the fraction of the three junction types, given by Eq. (15). Both the arithmetic mean and the harmonic mean are considered.

Using the arithmetic mean of the junction stiffness, the resulting aggregate modulus is predicted to be:

$$\frac{\tilde{E}}{\tilde{E}_M} = X_A^2 \lambda \sqrt{\eta} + 2X_A(1-X_A)\sqrt{\frac{(1+\eta)}{2}}\left(\frac{2\lambda}{1+\lambda}\right) + (1-X_A)^2 \tag{16}$$

The three additive terms on the right side represent the contributions from alumina-alumina, alumina-mullite, and mullite-mullite junctions, respectively. Analogously, the modulus prediction obtained from the harmonic mean of the junction stiffness is:

$$\frac{\tilde{E}}{\tilde{E}_M} = \left[\frac{X_A^2}{\lambda\sqrt{\eta}} + 2X_A(1-X_A)\sqrt{\frac{2}{1+\eta}}\left(\frac{1+\lambda}{2\lambda}\right) + (1-X_A)^2\right]^{-1} \tag{17}$$

A preliminary assessment of these results has been made through comparisons with numerical simulations based on the discrete element method. The nature of the simulations is essentially the same as those used for determining toughness of particle aggregates, with the exception that the aggregate now consists of two particle types with elastic properties given by those of alumina and mullite ($\lambda = 2$). In the present simulations, all junctions are assumed to be of the same size ($\eta = 1$). Figure 7 shows the results for two sets of simulations, for junction radii $a/R = 0.053$ and 0.313. The results are presented in terms of a modulus parameter that varies from 0 for $X_A = 0$ to 1 for $X_A = 1$. Also shown are the predictions from the analytical models (Eqs. (16) and (17)). Over the entire range of $X_A$, the predictions from the two analytical models bound the simulation results. In the limit where the concentration of the stiffer particles approaches zero ($X_A \to 0$ in this case), the arithmetic mean method yields more accurate results. By contrast, in the limit where $X_A \to 1$, the harmonic mean method is more accurate. For the range of compositions considered in this study ($X_A = 0$–0.4), the arithmetic mean method is preferred and is used in subsequent calculations.

An analogous analytical model has been developed for the toughness of a mixed aggregate. Following Eq. (9), the contribution from each junction type is assumed to be proportional to $\Gamma_j(a/R)^2$, weighted by the corresponding number fraction (Eq. (15)). The junction toughnesses are denoted $\Gamma_{AA}$, $\Gamma_{MM}$ and $\Gamma_{AM}$; the alumina to mullite toughness ratio is defined as $\Psi \equiv \Gamma_{AA}/\Gamma_{MM}$ and the alumina-mullite junction toughness is taken to be the average of the alumina-alumina and mullite-mullite junctions. Using the arithmetic averaging method, the toughness is predicted to be:

$$\frac{\tilde{\Gamma}}{\tilde{\Gamma}_M} = X_A^2 \Psi \eta + 2X_A(1-X_A)\left(\frac{1+\eta}{2}\right)\left(\frac{1+\Psi}{2}\right) + (1-X_A)^2 \tag{18}$$

The models were implemented in the following way. The modulus $\tilde{E}_M$ of the pure mullite aggregate was obtained from Eq. (7), calibrated according to the procedures outlined above. Based on the known elastic moduli of the particles, $\lambda = 2$. In comparing Eq. (15) to the experimental data, the remaining unknown variable, $\eta$, was used as a fitting parameter. The results of this fitting are shown in Fig. 6(a). The procedure yields $\eta \approx 3 \pm 1$ for all aging times. This value is qualitatively consistent with the expectation that the alumina-containing junctions sinter more rapidly than those with only mullite, and hence their junctions are larger. A similar procedure was used to compare the toughness model predictions with the experimental measurements. For consistency, the value of $\eta$ inferred from the modulus measurements was used in Eq. (18). The remaining unknown variable, $\Psi$, was used for fitting (Fig. 6(b)). The procedure yields a junction toughness ratio $\Psi = 1.0 \pm 0.3$. This result suggests that the toughnesses of the three junction types are similar to one another and that the increase in aggregate toughness with alumina content is mainly caused by the increase in the average junction area. The quality of the fits to both the modulus and the toughness data for all three aging times appears satisfactory, especially in light of the scatter in the experimental data. Furthermore, it is recognized that the scatter precludes determination of the fitting parameters $\eta$ and $\Psi$ with high accuracy.

## VI. Implications for Crack Deflection

Both the experimental results and the model predictions have been used to calculate the variation in the crack deflection parameter, $\Sigma$, with aging time, assuming the mixtures to be combined with Nextel 720 fibers (3M Corp.) to form a composite. The results are plotted on Fig. 8. Over the entire range of parameter values considered in this study, the crack deflection condition is predicted to be satisfied: that is, $\Sigma > 1$. The experimental results are also plotted on Fig. 1, demonstrating that

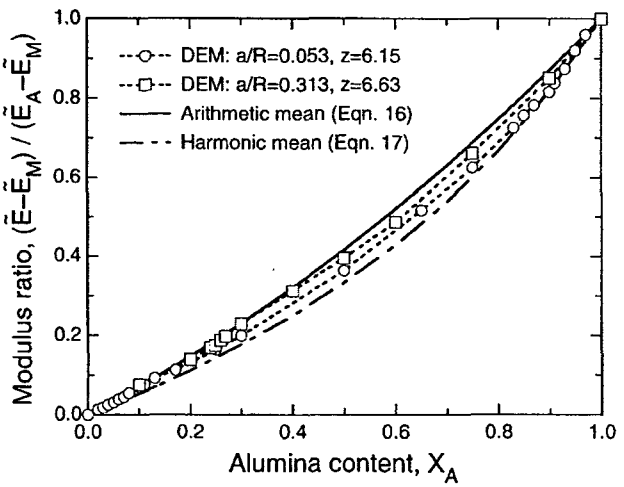


**Fig. 7.** Numerical simulations[17] and analytical results (Eqs. (16) and (17)) for Young's modulus of a mixture of spherical monosized alumina and mullite particles ($\lambda = 2$ and $\eta = 1$).

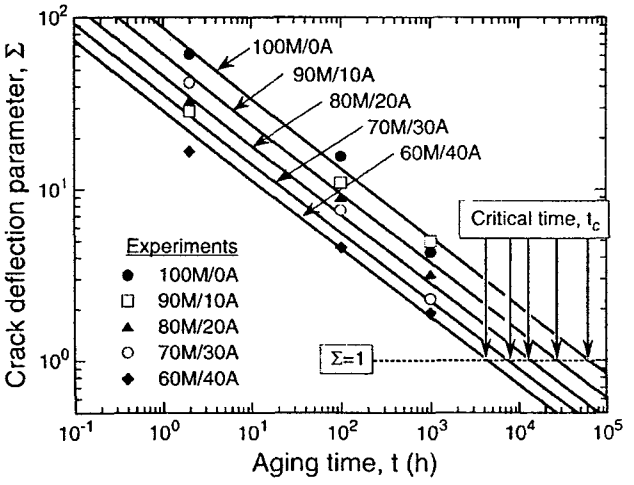


**Fig. 8.** Effects of aging time and composition on the crack deflection parameter $\Sigma$, using fiber properties $\Gamma_i = 15$ J/m² and $E_i = 260$ GPa. Solid lines are model predictions. Extrapolations of the predictions to $\Sigma = \omega = 1$ yield the critical times, $t_c$, at which crack penetration is predicted to occur.

the property combinations lie within the domain of crack deflection in the He and Hutchinson[7] diagram. These results reaffirm mullite-alumina mixtures as good candidate matrixes for use in oxide composites, even with rather high alumina content.

On extrapolation of the predictions in Fig. 8 to $\Sigma = \omega = 1$, the critical aging times $t_c$ for crack penetration are obtained. The times range from 4000 h for 60M/40A to 60 000 h for pure mullite: comparable to the targeted service times for CFCC components. Based on the differences in $t_c$, matrixes with lower alumina contents would be preferred.

## IV. Conclusion

Mullite-alumina mixtures exhibit physical and mechanical characteristics that make them attractive for use as porous matrixes in ceramic composites. The key attributes include stable porosity at the targeted service temperatures of oxide composites, especially for alumina concentrations <20%, and combinations of modulus and toughness that should lead to deflection of a matrix crack at a fiber-matrix interface. The models of mechanical properties of particle aggregates presented here coupled with the crack deflection parameter provide a means of extrapolating the experimental data to longer aging times, for the purpose of determining the critical times at which damage tolerance will be lost. With knowledge of the activation energies of the sintering mechanisms, the models could be extended to make such predictions for other temperatures.

Design of porous matrixes requires consideration of other properties, including shear and interlaminar strength, as well as compressive strength. These generally increase as the matrix is strengthened. As a result, among the mixtures considered in this study, those with higher alumina contents would be preferred, in contrast to the mullite-rich mixtures selected based on crack deflection considerations. These issues are currently being addressed.[2]

## References


[1]C. G. Levi, J. Y. Yang, B. J. Dalgleish, F. W. Zok, and A. G. Evans, "Processing and Performance of an All-Oxide Ceramic Composite," *J. Am. Ceram. Soc.*, **81**, 2077–86 (1998).

[2]M. A. Mattoni and F. W. Zok, to be published.

[3]M. A. Mattoni, J. Y. Yang, C. G. Levi, and F. W. Zok, "Effects of Matrix Porosity on the Mechanical Properties of a Porous-Matrix, All-Oxide Ceramic Composite," *J. Am. Ceram. Soc.*, **84** [11] 2594–602 (2001).

[4]J. A. Heathcote, X. Y. Gong, J. Y. Yang, U. Ramamurty, and F. W. Zok, "In-Plane Mechanical Properties of an All-Oxide Ceramic Composite," *J. Am. Ceram. Soc.*, **82** [10] 2721–30 (1999).

[5]E. A. V. Carelli, H. Fujita, J. Y. Yang, and F. W. Zok, "Effects of Thermal Aging on the Mechanical Properties of a Porous-Matrix Ceramic Composite," *J. Am. Ceram. Soc.*, **85** [3] 595–602 (2002).

[6]C. G. Levi, F. W. Zok, J. Y. Yang, M. Mattoni, and J. P. A. Lofvander, "Microstructural Design of Stable Porous Matrices for All-Oxide Ceramic Composites," *Z. Metallkd.*, **90** [12] 1037–47 (1999).

[7]M-Y. He and J. W. Hutchinson, "Crack Deflection at an Interface between Dissimilar Elastic Materials," *Int. J. Solids Struct. (UK)*, **25** [9] 1053–67 (1989).

[8]F. Zok, F. F. Lange, and J. R. Porter, "Packing Density of Composite Powder Mixtures," *J. Am. Ceram. Soc.*, **74** [8] 1880–85 (1991).

[9]H. Fujita, G. Jefferson, C. G. Levi, and F. W. Zok, "On the Use of an Alumina Precursor for Controlling the Mechanical Properties of Porous Mullite/Alumina Mixtures," *J. Am. Ceram. Soc.*, in review.

[10]ASTM Designation C 20–92. Book of ASTM Standards. American Society for Testing and Materials, West Conshohocken, PA.

[11]*Ceramic Source* **6**, The American Ceramic Society, Westerville, OH, 1990.

[12]H. G. Tattersall and G. Tappin, "The Work of Fracture and Its Measurement in Metals, Ceramics and Other Materials," *J. Mater. Sci.*, **1**, 296–301 (1966).

[13]M. F. Ashby, "A First Report on Sintering Diagrams," *Acta Metall.*, **22** [3] 275–89 (1974).

[14]R. M. German, "Fundamentals of Sintering"; pp. 260–69 in *Ceramics and Glasses, Engineered Materials Handbook* **4**, ASM International, Materials Park, OH, 1991.

[15]K. Walton, "The Effective Elastic Moduli of a Random Packing of Spheres," *J. Mech. Phys. Solids*, **35** [2] 213–26 (1987).

[16]G. Jefferson, G. K. Haritos, and R. M. McMeeking, "The Elastic Response of a Cohesive Aggregate: A Discrete Element Model with Coupled Particle Interaction," *J. Mech. Phys. Solids.*, **50** [12] 2539–75 (2002).

[17]G. Jefferson and R. M. McMeeking, to be published.

[18]B. R. Lawn, *Fracture of Brittle Solids*, 2nd Ed., Cambridge Solid State Science Series, Cambridge University Press, 1993.

[19]R. M. German, *Particle Packing Characteristics*, Metal Powder Industries Federation, Princeton, NJ, 1989.

[20]K. L. Johnson, *Contact Mechanics*, Cambridge University Press, 1985.

JOURNAL OF APPLIED PHYSICS VOLUME 95, NUMBER 1 1 JANUARY 2004

# Effective conductivity of partially sintered solids

J. R. Dryden
*Department of Mechanical and Materials Engineering, The University of Western Ontario, London, Ontario N6A 5B9, Canada*

F. W. Zok[a)]
*Department of Materials, The University of California, Santa Barbara, California 93106*

(Received 28 May 2003; accepted 7 October 2003)

An analytical model to predict the effective conductivity of a partially sintered solid is presented. It is based on an analysis of heat flow through a spherical particle embedded in a self-consistent matrix. Determination of the effective conductivity reduces to solving an integral equation, and a numerical solution of this equation is presented. In the limiting cases wherein the contact size is either small or comparable to the particle size, approximate analytical results are obtained which agree very well with the numerical solution. Furthermore, when pieced together, the two solutions are found to describe the effective conductivity over the entire range of contact sizes. © *2004 American Institute of Physics.* [DOI: 10.1063/1.1630360]

## I. INTRODUCTION

There has been a considerable amount of research directed toward predicting the effective thermal conductivity of porous and granular solids.[1–10] In most of these treatments,[3–7] it has been assumed that contacts between particles are sufficiently small so that the constriction resistance to heat flow corresponds to a contact spot separating two infinite half spaces.[11] This treatment is reasonable in the analysis of granular solids where the contact areas depend upon Hertzian mechanics. However, in the case of partially sintered solids, the finite contact size must be taken into account. Although there have been two numerical studies,[9,10] this problem has received less attention.

Here, a calculation of the self-consistent type, where the heat flow through a sphere embedded in a self-consistent matrix, is presented. No other shape for equiaxed particles seems to offer any chance of an analytical solution. Similar to the calculation done by Argento and Bouvard,[9] we take two contacts per sphere. These two caps are held at a self-consistent temperature, and the remaining portion of the sphere surface is adiabatic.

## II. PRELIMINARY COMMENTS

From a macroscopic viewpoint, the porous solid is isotropic with respect to heat flow and its effective conductivity is $k_e$. Consequently, only heat flow in one direction needs to be analyzed. Here, heat flow in the $Z$ direction is considered, and the apparent temperature is written as $\mathcal{T}_e = CZ$. On a finer scale, the microstructure is nonuniform, and flow pattern is tesellated. In the simplest case, there are two phases: Solid particles with thermal conductivity $k$, and a gas phase with thermal conductivity $k_g$. A typical particle has a portion of its surface surrounded by gas with the remainder of its surface being in contact with its nearest neighbors. Let $\rho$ be equal to the ratio of the contact radius to solid particle radius. For sufficiently small values of $\rho$, the flow constriction through the solid contacts becomes severe and the heat flow is predominantly through the gas phase. On the other hand, it has been shown by Batchelor,[4] that when $k\rho \gg k_g$, the heat flow through the gas phase is negligible. This condition is satisfied in most partially sintered solids.

Initially, the individual solid particles are approximately spherical. However, as sintering proceeds, the shape of each particle becomes irregular. If the particles remain equiaxed, it is useful to consider a "test" region that contains an average representative particle. The analysis presented here is concerned with analyzing the temperature field in this representative test region, and then relating this field to obtain an estimate for the effective conductivity. In a calculation of this type, neither the particle radius $a$ nor the magnitude $C$ of the thermal gradient, affects the estimate for $k_e$. Consequently, it is convenient to define dimensionless variables $z \equiv Z/a$, and $T_e \equiv \mathcal{T}_e/Ca$. Using these definitions,

$$T_e \equiv \frac{\mathcal{T}_e}{Ca} = z. \tag{1}$$

From this point onward in the article, all spatial variables and temperatures are dimensionless.

## III. TEMPERATURE WITHIN THE TEST PARTICLE

To make the problem tractable, the shape of the test particle is taken as being a sphere having a radius equal to $a$. In view of the spatial scaling, the sphere has a dimensionless unit radius, and the dimensionless temperature in the particle is designated by $T$. For simplicity, the origin is placed at the center of the particle. Spherical coordinates $(r, \theta)$ are used where $r$ is the distance from the center of the sphere and $\theta$ is the angle measured from the $z$ axis. The temperature $T$ must satisfy Laplace's equation

$$\nabla^2 T = 0. \tag{2}$$

a)Electronic mail: zok@engineering.ucsb.edu

 

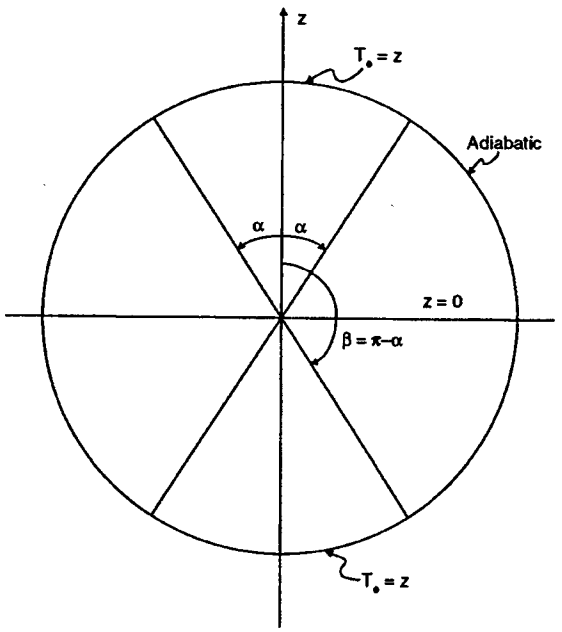


FIG. 1. Spherical test particle where the polar caps are symmetrical, i.e., $\beta=\pi-\alpha$ so that the temperature is an odd function of $z$.

The test particle is shown in Fig. 1, and on the surface, $r=1$, the following boundary conditions are imposed. Within the equatorial region, i.e., $\alpha<\theta<\beta$, there is no radial flow and the boundary condition is then

$$\frac{\partial T}{\partial r}=0 \quad (\beta>\theta>\alpha). \tag{3}$$

The apparent overall temperature $T_e=z$, and the surface of the sphere corresponds to $z=\cos\theta$. Therefore, on the north and south polar caps subtending the cone of angle $2\alpha$, the boundary condition

$$T=\cos\theta \quad (\alpha>\theta\geqslant 0,\pi\geqslant\theta>\beta), \tag{4}$$

is imposed. The temperature in the test sphere is written in the form

$$T=rP_1(\cos\theta)-\sum_{n=1}^{\infty}\frac{1+2n}{n}C_nP_n(\cos\theta)r^n, \tag{5}$$

where the terms $P_n(\cos\theta)$ are Legendre's polynomials. The temperature is an odd function of $z$ so that only the terms, $n=1,3,5,\cdots$ are taken. The expression for $T$ satisfies Laplace's equation, and the coefficients $C_n$ are found using the two boundary conditions that are prescribed above. Using these two boundary conditions, it is found that the coefficients $C_n$ must satisfy the following conditions:

$$\sum_{n=1}^{\infty}C_n(1+H_n)P_n(\cos\theta)=0 \quad (\alpha>\theta\geqslant 0,\pi\geqslant\theta>\beta) \tag{6}$$

$$\sum_{n=1}^{\infty}C_n(1+2n)P_n(\cos\theta)=6\lambda P_1(\cos\theta) \quad (\beta>\theta>\alpha), \tag{7}$$

where the various coefficients are defined by

$$H_n=\frac{1}{2n}, \tag{8}$$

$$\lambda=\frac{1}{6}. \tag{9}$$

The relations in Eqs. (6) and (7) are referred to as triple series relations.[12,13] The adjective "triple" arises from the fact that there are three different zones: (i) $\alpha>\theta\geqslant 0$, (ii) $\beta>\theta>\alpha$, and (iii) $\pi\geqslant\theta>\beta$. These mixed boundary value problems are generally more difficult than the standard problems where there is only a single condition over the entire surface. The aim is to find the coefficients $C_n$ that satisfy the triple relations.

Owing to the symmetry of the present problem, the temperature is antisymmetric with respect to the plane $z=0$ so that the Legendre coefficients $C_0$, $C_2$, $C_4,\cdots C_{2n}$ must vanish. As described by Collins,[12] in order to determine the Legendre coefficients, it is necessary to write $C_n=A_n+B_n$ and it follows that

$$C_n=A_n+B_n \quad \text{and} \quad B_n=-(-1)^nA_n. \tag{10}$$

The triple relations in Eqs. (6) and (7) are written as

$$\sum_{n=0}^{\infty}(A_n+B_n)(1+H_n)P_n(\cos\theta)=0 \quad (\alpha>\theta\geqslant 0), \tag{11}$$

$$\sum_{n=0}^{\infty}A_n(1+2n)P_n(\cos\theta)-3\lambda P_1(\cos\theta)=0 \quad (\pi\geqslant\theta>\alpha), \tag{12}$$

$$\sum_{n=0}^{\infty}B_n(1+2n)P_n(\cos\theta)-3\lambda P_1(\cos\theta)=0 \quad (\beta>\theta\geqslant 0), \tag{13}$$

$$\sum_{n=0}^{\infty}(A_n+B_n)(1+H_n)P_n(\cos\theta)=0 \quad (\pi\geqslant\theta>\beta). \tag{14}$$

The coefficients $A_0$, $B_0$ are not equal to zero so that the lower limit on the summation has been changed. To avoid objection over the possibility of division by zero, the term $H_0\equiv 1$; this definition is inconsequential because $A_0+B_0=0$. Owing to the symmetry of the problem, only the first two equations [Eqs. (11) and (12)] need to be considered.

It is known that the Legendre polynomials can be represented by the Mehler–Dirichlet integrals

$$P_n(\cos\theta)=\frac{\sqrt{2}}{\pi}\int_{t=0}^{\theta}\frac{\cos[(n+1/2)t]dt}{\sqrt{\cos t-\cos\theta}}, \tag{15}$$

$$=\frac{\sqrt{2}}{\pi}\int_{t=0}^{\pi}\frac{\sin[(n+1/2)t]dt}{\sqrt{\cos\theta-\cos t}}. \tag{16}$$

The representation for $P_n(\cos\theta)$ in Eq. (15) is used in Eq. (11) and, after interchanging the order of integration and summation, it follows that

$$\int_{t=0}^{\theta} \frac{dt}{\sqrt{\cos t-\cos\theta}} \left\{ \sum_{n=0}^{\infty} (A_n+B_n)(1+H_n) \times \cos(n+1/2)t \right\} = 0. \tag{17}$$

Similarly, the representation for $P_n(\cos\theta)$ in Eq. (16) is used in Eq. (12) and, after interchanging the order of integration and summation, it follows that

$$\int_{t=0}^{\pi} \frac{dt}{\sqrt{\cos\theta-\cos t}} \times \left\{ \frac{d}{dt} \left[ \sum_{n=0}^{\infty} A_n \cos(n+1/2)t - \lambda \cos 3t/2 \right] \right\} = 0. \tag{18}$$

Equations (17) and (18) can be solved using Eqs. (2.3.5) and (2.3.6) in Ref. 13. In both cases, the quantities within the $\{\cdots\}$ must vanish. In Eq. (18), the portion within $[\cdots]=D$ and the constant $D=0$; this follows by noting that the expression within $[\cdots]$ vanishes at $t=\pi$. Thus, the two results

$$\sum_{n=0}^{\infty} (A_n+B_n)(1+H_n)\cos[(n+1/2)t]=0 \quad (\alpha>t\geq 0), \tag{19}$$

$$\sum_{n=0}^{\infty} A_n \cos[(n+1/2)t]-\lambda\cos(3t/2)=0 \quad (\pi\geq t>\alpha), \tag{20}$$

are obtained. Here, the coefficient $A_n$ is found and once this is known the other two coefficients, $C_n$, $B_n$ can be found by use of Eq. (10). To find $A_n$, an unknown function $j(t)$ is defined as follows

$$\sum_{n=0}^{\infty} A_n \cos\left[\left(n+\frac{1}{2}\right)t\right] = \begin{cases} \lambda\cos(3t/2)-j(t)/2 & (\alpha>t\geq 0) \\ \lambda\cos(3t/2) & (\pi\geq t>\alpha) \end{cases}. \tag{21}$$

The functions $\cos(n+1/2)t$ are orthogonal over the interval $(0\leq t\leq\pi)$ and thus the coefficient $A_n$ is

$$A_n=\lambda\delta_{1n}-\frac{1}{\pi}\int_{u=0}^{\alpha} j(u)\cos\left[\left(n+\frac{1}{2}\right)u\right]du, \tag{22}$$

where $\delta_{1n}=0$ when $n\neq 1$. Expressions (21) and (10) are then substituted into Eq. (19) to obtain

$$j(t)+2\sum_{n=0}^{\infty} A_n\{(-1)^n-H_n[1-(-1)^n]\}\cos\left[\left(n+\frac{1}{2}\right)t\right] = 2\lambda\cos\left(\frac{3t}{2}\right). \tag{23}$$

Using the expression for $A_n$, and interchanging the order of summation and integration, Eq. (24) is found for the determination of $j(t)$:

$$j(t)=\cos(3t/2)+\frac{1}{\pi}\int_0^{\alpha} j(u)J(u,t)du \quad \text{where} \quad (\alpha>t\geq 0). \tag{24}$$

The kernel $J(u,t)=K(t-u)+K(t+u)$ and $K(\xi)$ is

$$K(\xi)=\sum_{n=0}^{\infty}\{(-1)^n-H_n[1-(-1)^n]\}\cos\left[\left(n+\frac{1}{2}\right)\xi\right] = \frac{1}{4}\left\{2\sec\left(\frac{\xi}{2}\right)+\pi\sin\left|\frac{\xi}{2}\right|+\cos\left(\frac{\xi}{2}\right)\ln\left[\tan^2\left(\frac{\xi}{2}\right)\right]\right\}. \tag{25}$$

The closed forms for the infinite summations in Eq. (25) can be found from the results given in standard tables.[14] For general values of $\alpha$, the function $j(t)$ can only be found by a numerical treatment.

To summarize this section, the function $j(t)$ is a solution of the integral Eq. (24). The coefficients $A_n$ are then found from Eq. (22) and the odd Legendre–Fourier series coefficients $C_{2n+1}=2A_{2n+1}$. Finally, these coefficients are used in Eq. (5) to find the temperature.

## IV. POWER EQUIVALENT CONDUCTIVITY

On the macroscopic level, the dimensionless apparent temperature, $T_e=z$, is given in Eq. (1). The thermal "power" $P$ (which here has the same units as the conductivity), expended within the test volume $V$ is expressed by the integral

$$P=k_e\int_V \text{grad}\,T_e\cdot\text{grad}\,T_e dV=k_e V.$$

The test volume $V$ is comprised of two phases and, if there is negligible flow through the gas phase, then $P$ is due to the power expended in the solid sphere. The power $P$ can be alternatively written as

$$P=k\int_{V_s}\text{grad}\,T\cdot\text{grad}\,T dV,$$

where $V_s=4\pi/3$ is the dimensionless volume of the sphere. Upon equating these two expressions for $P$, the power equivalent thermal conductivity is

$$k_e=kf\sigma, \tag{26}$$

where $f=V_s/V$ is the volume fraction of solid, and the conductance $\sigma$ is defined as

$$\sigma=\frac{1}{V_s}\int_{V_s}\text{grad}\,T\cdot\text{grad}\,T dV. \tag{27}$$

The conductance $\sigma$ is equal to the average squared magnitude of the temperature gradient within the sphere. In this expression, the volume integral can be converted to an integral over the surface of the sphere by the use of the divergence theorem. In view of the boundary conditions in Eqs. (3) and (4), along with the orthogonal nature of the Legendre polynomials, it follows after substituting the series in Eq. (5) into the surface integral that $\sigma=1-3C_1$. The coefficient $C_1=2A_1$ and using the expression for $A_1$ in Eq. (22), the expression for $\sigma$ is found as

$$\sigma=\frac{6}{\pi}\int_{u=0}^{\alpha} j(u)\cos\left(\frac{3u}{2}\right)du. \tag{28}$$

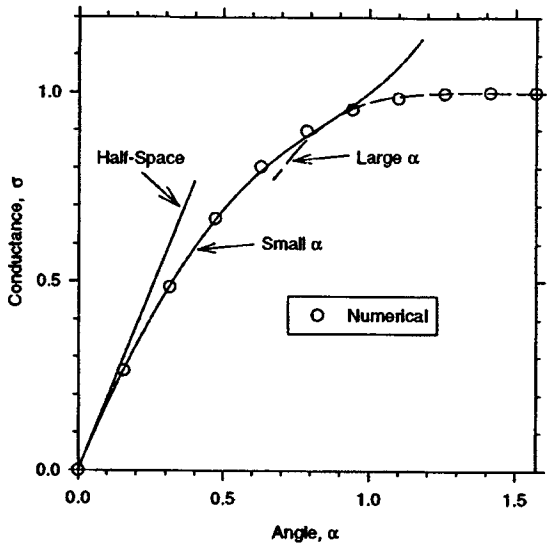


FIG. 2. The conductance $\sigma$ as a function of the cap angle $\alpha$. The symbols O are obtained by numerical integration. [The solid line labeled "small $\alpha$" is obtained from Eq. (30). The results of Eq. (31) represent the half-space approximation. Finally, the dashed line labeled "large $\alpha$", represents the prediction of Eq. (36)].

To evaluate this conductance, the function $j(t)$ is found by numerically solving the integral Eq. (24) for the following ten values of $\alpha$: $\pi/20$, $2\pi/20$, $3\pi/20,\cdots\pi/2$. For each value of $\alpha$, the region $0<u<\alpha$ is subdivided into 60 segments (this is found to give sufficiently accurate results), and a set of 60 linear equations is generated using Eq. (24). This set of 60 equations is then solved to find $j(t)$ at the discrete increments, $t=t_1,t_2,\cdots t_{60}$, within the interval $0<t<\alpha$. The values, $j(t_1),j(t_2),\cdots j(t_{60})$, are then used to evaluate $\sigma$ and the results are shown by the symbols in Fig. 2.

### A. Approximate solution for $\sigma$ when $\alpha<1$

If $\alpha$ is small, the integral equation is amenable to an iterative solution. Using the expression for $j(t)$ given in Eq. (24), the conductance can be rewritten as

$$\sigma=\frac{3}{\pi}\left\{\alpha+\frac{\sin 3\alpha}{3}\right\}+\frac{6}{\pi^2}\int_0^\alpha\int_0^\alpha J(u,t)j(u)\cos\left(\frac{3t}{2}\right)dudt. \tag{29}$$

When $\alpha$ becomes sufficiently small, the function $j(u)\approx\cos(3u/2)$, and the kernel can be approximated by its singular portion $J(u,t)\sim\ln|u^2-t^2|/2$. Neglecting the higher-order terms, the conductance is

$$\sigma\sim\frac{3}{\pi}\left\{\alpha+\frac{\sin 3\alpha}{3}+\frac{\alpha^2\ln\alpha^2}{\pi}\right\}. \tag{30}$$

As shown in Fig. 2, this estimate for $\sigma$ is reasonably accurate for values of $\alpha<1$. In the limit when $\alpha\ll1$, the estimate for $\sigma$ reduces to linear equation

$$\sigma\sim\frac{6\alpha}{\pi}. \tag{31}$$

As discussed later, this represents the half-space approximation, and is shown in Fig. 2.

### B. Approximate solution for $\sigma$ when $\alpha>1$

For larger values of $\alpha$, the integral equation is not amenable to an iterative solution of the type described above. On the other hand, when $\alpha$ becomes large, the perturbation of the heat flow from the uniform flux is not very severe and it is possible to find fairly accurate approximate solutions.

To begin, it is known from the theory of variational calculus that a lower bound for $\sigma$ can be obtained by suitable mathematical manipulation of the functional given in Eq. (27). To obtain this bound it is necessary to find a vector, say s, that has its divergence equal to zero, and also has no component crossing $r=1$ in the region $\beta>\theta>\alpha$. This vector can be obtained as the gradient of a function $F$ and the function is harmonic so that $\nabla^2F=0$. Such a function can be expressed as a Legendre–Fourier series

$$F=\sum_{n=0}^{\infty}\left\{\frac{4n+3}{2n+1}\right\}I_{2n+1}P_{2n+1}(\cos\theta)r^{2n+1}. \tag{32}$$

The coefficients $I_{2n+1}$ are chosen so that $F$ satisfies the boundary conditions

$$\frac{\partial F}{\partial r}=\begin{cases}\cos\theta & \alpha>\theta>0\\ 0 & \beta>\theta>\alpha\\ \cos\theta & \pi>\theta>\beta\end{cases}. \tag{33}$$

To satisfy this boundary condition, the coefficients $I_{2n+1}$ are expressed by the integrals

$$I_{2n+1}=\int_0^\alpha P_{2n+1}(\cos\theta)\cos\theta\sin\theta d\theta. \tag{34}$$

According to standard treatment,[15] the lower bound for $\sigma$ is found by suitable mathematical manipulation upon the functional given in Eq. (27). After doing these manipulations, and using the divergence theorem, the bound for $\sigma$ is given by the following integral which is evaluated on the spherical surface $r=1$,

$$\sigma=\int_0^\alpha(6T_e-3F)\cos\theta\sin\theta d\theta,$$
$$=6I_1-3\sum_{n=0}^{\infty}\left\{\frac{4n+3}{2n+1}\right\}I_{2n+1}^2. \tag{35}$$

When $\alpha\to\pi/2$, the summation can be represented by its first term and the estimate for $\sigma$ reduces to the simple expression

$$\sigma\sim1-\cos^6\alpha. \tag{36}$$

This bound can be improved by multiplying $F$ by a constant say $D$ and then adjusting this constant so as to maximize $\sigma$. However, when $\alpha\approx\pi/2$, this refinement does not make much improvement to the estimate for $\sigma$. The behavior of this bound is shown in Fig. 2 and, for large values of $\alpha$, it is in very good agreement with the numerical results.

## V. DISCUSSION AND CONCLUSIONS

In a real material, each particle is surrounded on average by $N$ nearest neighbors and $\bar{\alpha}$ is the average cap angle of the contacts. According to their outward normal, these contacts can be partitioned into six different directions $\pm(\hat{i},\hat{j},\hat{k})$. In the analysis presented here, the cap angle $\alpha$ is expressed by $\alpha \equiv \bar{\alpha}N/6$. When the contacts are very small in comparison with the size of the particles, the conductance is given by Eq. (31), and $\sigma = \bar{\alpha}N/\pi$. The effective conductivity is then written as

$$k_e = \frac{kfN\bar{\alpha}}{\pi}. \tag{37}$$

This is the same result for the effective conductivity that has previously been deduced by Batchelor and O'Brien.[4] As the cap angle $\alpha$ increases, the conductance becomes a nonlinear function of $\alpha$ and $\sigma$ is given approximately by either Eq. (30) or (36).

The present analysis can be related to a unit-cell treatment where the particles are arranged in a simple cubic array. When $\alpha \ll 1$, the spherical particles are barely touching each other and the volume fraction, $f = \pi/6$, then corresponds to simple cubic packing of spheres. Furthermore, according to Eq. (31), the limiting behavior of the conductance is given by $\sigma \sim 6\alpha/\pi$ so that the effective conductivity is $k_e = kf\sigma \sim k_e\alpha$. Now, consider the vertical flow of heat through a simple cubic array. Taking symmetry into account, the four lateral faces are adiabatic while the top and bottom cube faces are isothermal. Thus, when $\alpha \ll 1$, each isothermal contact has a radius approximately equal to $\alpha$, and, neglecting the curvature of the sphere, the total constriction resistance is $R_c = 1/2k\alpha$. The unit-cell cube has dimensions $2\times2\times2$, and if its conductivty is $k_e$ then its resistance is $R_e = 1/2k_e$. Upon equating these two resistances, it follows that $k_e = k\alpha$ and this is in agreement with the treatment given here.

As sintering progresses the size of the necks between neighboring particles increases. In the unit-cell model the particle shape has cubic symmetry; the initially spherical particle acquires six facets corresponding to the cube faces. There is no analytical method for deducing the thermal field in such a truncated shape, and it is necessary to resort to a numerical solution. Selecting a spherical test particle has the advantage that it allows a semianalytic solution for the thermal field.

The effective conductivity in Eq. (26) has the simple form $k_e = kf\sigma$, and up to this point, only the behavior of $\sigma$ has been considered. The conductance $\sigma$ depends on the neck growth, whereas the volume fraction $f$ depends on the degree of densification. Ashby[16] points out that there are six distinguishable sintering mechanisms, all causing neck growth. In contrast, only some of mechanisms lead to densification. Although obtaining a general relationship between $\alpha$ and $f$ is beyond the scope of this article, a few remarks are possible. First, during the early stages of sintering there is only neck growth while the $f$ remains constant. Second, at later stages of sintering, corresponding in the analysis to $\alpha \to \pi/2$, the conductance $\sigma \sim 1$. The effective conductivity is then approximately given as $k_e = kf$ and the model reduces to the law of mixtures. In almost fully dense sintered solids, the porosity exists as isolated spheres and the effective thermal conductivity is better described using Maxwell's[17] estimate instead of the law of mixtures.

## ACKNOWLEDGMENTS

Funding for one of the authors (J.R.D.) was provided by NSERC, and, for another author (F.W.Z.), by the Air Force Office of Scientific Research under Contract No. F49620-02-1-0128, monitored by Dr. B. L. Lee.

[1] M. Kaviany, *Principles in Heat Transfer in Porous Media* (Springer, New York, 1966).
[2] S. Torquanto, *Random Heterogeneous Materials* (Springer, Berlin, 2002).
[3] C. K. Chan and C. L. Tien, ASME J. Heat Transfer **95**, 302 (1973).
[4] G. K. Batchelor and R. W. O'Brien, Proc. R. Soc. London, Ser. A **355**, 313 (1977).
[5] Y. Ogniewicz and M. M. Yovanovich, *Aerodynamic Heating and Thermal Protection Systems*, Progress in Astronautics and Aeronautics, Vol. 59, edited by L. S. Fletcher (American Institute of Aeronautics and Astronautics, 1977).
[6] A. Jagota and C. Y. Hui, J. Appl. Mech. **57**, 789 (1990).
[7] J. B. Keller, J. Appl. Phys. **34**, 991 (1963).
[8] I. H. Tavman, Int. Commun. Heat Mass Transfer **23**, 169 (1996).
[9] C. Argento and D. Bouvard, ASME J. Heat Transfer **39**, 1343 (1996).
[10] W. W. M. Siu and S. H.-K. Lee, ASME J. Heat Transfer **43**, 3917 (2000).
[11] H. S. Carslaw and J. C. Yaeger, *Conduction of Heat in Solids* (Oxford University Press, Oxford, UK, 1959).
[12] W. D. Collins, Arch. Ration. Mech. Anal. **11**, 122 (1962).
[13] I. N. Sneddon, *Mixed Boundary Value Problems in Potential Theory* (North-Holland, Amsterdam, 1966), p. 41.
[14] A. P. Prudnikov, Y. A. Brychkov, and O. I. Marichev, *Integrals and Series* (Gordon and Breach, New York, 1966), Vol. 1.
[15] A. M. Arthurs, *Complementary Variation Principles*, 2nd ed. (Oxford University Press, Oxford, UK, 1980).
[16] M. F. Ashby, Acta Metall. **22**, 275 (1974).
[17] J. C. Maxwell, *A Treatise on Electricity and Magnetism*, 3rd ed. (Oxford University Press, Oxford, UK, 1904), Vol. 1.

journal

J. Am. Ceram. Soc., 87 [5] 914–922 (2004)

# Notch Sensitivity of Ceramic Composites with Rising Fracture Resistance

Michael A. Mattoni* and Frank W. Zok*

Materials Department, University of California, Santa Barbara, California 93106

**A theoretical framework is developed for the notched strength of ceramic composites that exhibit rising fracture resistance. It is based on established concepts of crack stability under stress-controlled loadings. On using a linear representation of the resistance curve (expressed in terms of an energy release rate), straightforward analytical solutions are obtained for the strength as well the amount of stable crack growth preceding fracture and the associated fracture resistance. Calculations are performed for several test configurations commonly used for material characterization, including single- and double-edge-notched tension, center-notched tension, and single-edge-notched bending. The results reveal salient trends in strength with notch length and specimen geometry. An assessment of the theory is made through comparison with experimental measurements on an all-oxide fiber composite. Transitions in the degree of notch sensitivity with notch length are identified and explored. The utility of the theoretical results both for rationalizing the trends in measured notched strength and for guiding experimental studies of notch sensitivity is demonstrated.**

## I. Introduction

Crack growth in continuous fiber ceramic composites (CFCCs) is characterized by a rising fracture resistance beyond the initiation toughness, $G_0$, a manifestation of fiber bridging in the crack wake. When the bridging fibers furthest from the crack tip disengage, the resistance reaches a steady-state value, $G_{ss}$, independent of further crack growth. The steady-state bridging toughness is $\Delta G_b = \beta\sigma_* u_*$, where $u_*$ is the critical crack opening displacement to disengage the bridging fibers, $\sigma_*$ is a measure of the pullout stress, and $\beta$ is a nondimensional parameter of order unity.[1] The amount of crack growth $\Delta a_{ss}$ needed to achieve steady state is dictated by a characteristic bridging length scale: $a_{ch} = \bar{E}u_*/\sigma_*$, where $\bar{E}$ is the plane strain Young's modulus.[1,2] For typical values of the material parameters ($\bar{E}$ = 100 GPa, $u_*$ = 30–100 μm, and $\sigma_0$ = 30–100 MPa), the bridging toughness is $10^3$–$10^4$ J/m$^2$ and the characteristic length scale is 10–100 mm. The implications are 2-fold. (i) Significant toughening can be obtained at steady state, relative to the initiation toughness. (ii) Because of the large amount of crack growth needed to achieve steady state, the benefits of the rising resistance curve in composite strength are not fully realized. That is, crack growth becomes unstable with respect to the applied stress long before steady state is achieved.

The objective of this paper is to address the related issues of crack stability and notch sensitivity of strength in ceramic composites that exhibit a rising fracture resistance, both theoretically and experimentally. On the theoretical front, an analytical framework is developed for describing crack stability in an orthotropic material. It is based on comparisons of the energy release rates of common notched test configurations with the material's fracture resistance. Analogous treatments of notch sensitivity have been used previously for other materials that exhibit rising fracture resistance, including metal-, whisker- and fiber-reinforced ceramics[3,4] and ceramics toughened by grain pullout.[5,6] For our purpose, the resistance curve $G_R(\Delta a)$ is assumed to be *linear* over the range of crack growth preceding instability. Furthermore, the size of the inelastic deformation zone at the crack tip is considered to be small in relation to the geometric and the bridging length scales, i.e., small-scale yielding conditions are obtained. Effects of inelasticity are thus embodied in the initiation toughness. Elsewhere the material is assumed to be elastically orthotropic. To assess the theory, comparisons are made with experimental measurements of fracture-resistance curves and notch sensitivity of strength in a porous-matrix all-oxide CFCC.

It is emphasized that the theoretical approach is based on an assumed form of the resistance curve, notably linear; no attempt is made to model the resistance curve itself. The latter problem falls in the domain of bridging micromechanics, a field that has been explored exhaustively over the past decade. Although micromechanics provides a more fundamental link between the bridging phenomenon and the macroscopic response, it requires numerical solution of the integral equations governing the crack-opening displacement profile, the crack-tip stress intensity factor, and the bridging traction law. As a consequence, it is likely to find limited use in the engineering community. Arguably, for the purpose of predicting the strength of notched or flawed structures, micromechanics is not essential. Instead, only a convenient functional form for the resistance curve is required. This phenomenological approach has proved to be useful in addressing strength variability in ceramics.[5] Furthermore, as illustrated in the present paper, in cases where the resistance curve is linear (as it is in the oxide composite of interest), straightforward analytical solutions for notched strength are obtained. These solutions allow probing of the effects of specimen type and size on notch sensitivity and identifying transitions in behavior.

## II. Theory of Crack Stability

To begin, it is instructive to consider the case of a specimen of width $W$, containing a small center notch of length $2a_0$, and loaded in tension perpendicular to the notch plane along one of the principal material axes. In the limit where $a_0 \ll W$, the energy release rate is given by

$$G = g(\rho,\lambda)\left(\frac{\sigma^2\pi a}{\bar{E}}\right) \tag{1}$$

where $\sigma$ is the applied tensile stress, $g(\rho,\lambda)$ characterizes the effect of orthotropy,[7,8] and $\rho$ and $\lambda$ are defined by

$$\lambda \equiv \frac{E_2}{E_1} \tag{2}$$

E. Lara-Curzio—contributing editor

Manuscript No. 10234. Received May 20, 2003; approved December 12, 2003.
This work was supported financially by the Air Force Office of Scientific Research under Contract No. F49620-02-1-0128, monitored by Dr. B. L. Lee.
*Member, American Ceramic Society.

$$\rho \equiv \frac{(E_1E_2)^{1/2}}{2\mu_{12}} - (\nu_{12}\nu_{21})^{1/2} \tag{3}$$

with the subscripts 1 and 2 referring to the principal material axes, $\mu$ the shear modulus, and $\nu$ the Poisson's ratio. Composite materials with balanced symmetric fiber lay-ups exhibit cubic in-plane symmetry, whereupon $\lambda = E_1/E_2 = 1$ and $\nu_{12} = \nu_{21}$. Moreover, for $0 < \rho < 3$, the function $g(\rho)$ can be well-approximated by[8]

$$g(\rho) = 1 + 0.44(\rho - 1) \tag{4}$$

Unstable crack growth (at the stress maximum) occurs when[9]

$$G = G_R \tag{5a}$$

$$\frac{dG}{da} \geq \frac{dG_R}{da} \tag{5b}$$

These conditions are represented by the tangent construction plot shown in Fig. 1. Here, $G_R$ is plotted against the amount of crack growth, $\Delta a$, and the energy release rate, $G$, is plotted against the *total* crack length, $a_0 + \Delta a$. In this context, the right side of the abscissa is interpreted as $\Delta a$ and the left side as $a_0$. The resistance initiates at $G_0$ and subsequently increases with $\Delta a$ at a rate characterized by the tearing modulus: $T \equiv dG_R/da$. The conditions in Eq. (5) are satisfied when the curve $G(\Delta a + a_0)$ is tangent to the curve $G_R(\Delta a)$. If the resistance curve $G_R(\Delta a)$ is linear, the stability of the crack on initial growth is dictated by the slopes of the two curves *at* $G_0$ (Fig. 1(a)). That is, if $dG/da > T$ at $G = G_0$, crack growth occurs unstably under a decreasing stress. Consequently, the strength is controlled by the initiation toughness via the Griffith equation; no strength benefit is derived from the increasing resistance. Conversely, if $dG/da < T$ at $G = G_0$, continued crack growth requires an increase in stress beyond that for initiation. The transition from unstable to stable growth occurs at a critical tearing modulus, $T_c$, at which $dG/da = T$ at $G = G_0$. From Eq. (5) or inspection of Fig. 1, the critical tearing modulus in nondimensional form is

$$\frac{T_c W}{G_0} = \frac{W}{a_0} \tag{6}$$

Interestingly, since both $T_c$ and $G_0$ scale with $g(\rho,\lambda)$, the nondimensional result in Eq. (6) is *independent* of material orthotropy.

The same approach is used to address the stability of cracks in *finite* bodies. The effects of $a/W$ on the energy release rate can be described generically by

$$G = H(a/W)\, g(\rho,\lambda)\left(\frac{\sigma^2\pi a}{\bar{E}}\right) \tag{7}$$

where $H(a/W)$ is a nondimensional function that depends on both the specimen geometry and the loading configuration. Combining Eqs. (5) and (7), the critical tearing modulus becomes

$$\frac{T_c W}{G_0} = \frac{W}{a_0} + \left(\frac{1}{H(a_0/W)}\right)\frac{dH(a_0/W)}{d(a/W)} \tag{8}$$

In the limit where $a_0/W \to 0$, the first term on the right side dominates and the critical tearing modulus reduces to the 1 in Eq. (6), as required.

If $T \leq T_c$, the instability occurs at the initiation toughness at the Griffith stress, $\sigma_0$, written in nondimensional form as

$$\frac{\sigma_0^2\pi W}{\bar{E}G_0} = \frac{1}{(a_0/W)\, H(a_0/W)\, g(\rho,\lambda)} \tag{9}$$

Conversely, if $T > T_c$, stable crack growth occurs until the conditions in Eq. (5) are satisfied. This scenario is represented by the tangent construction in Fig. 1(b). Provided that instability occurs within the linear region of the resistance curve, the critical values of crack length, $a_f$, resistance, $G_f$, and stress, $\sigma_f$, are found (from Eq. (5)) to be

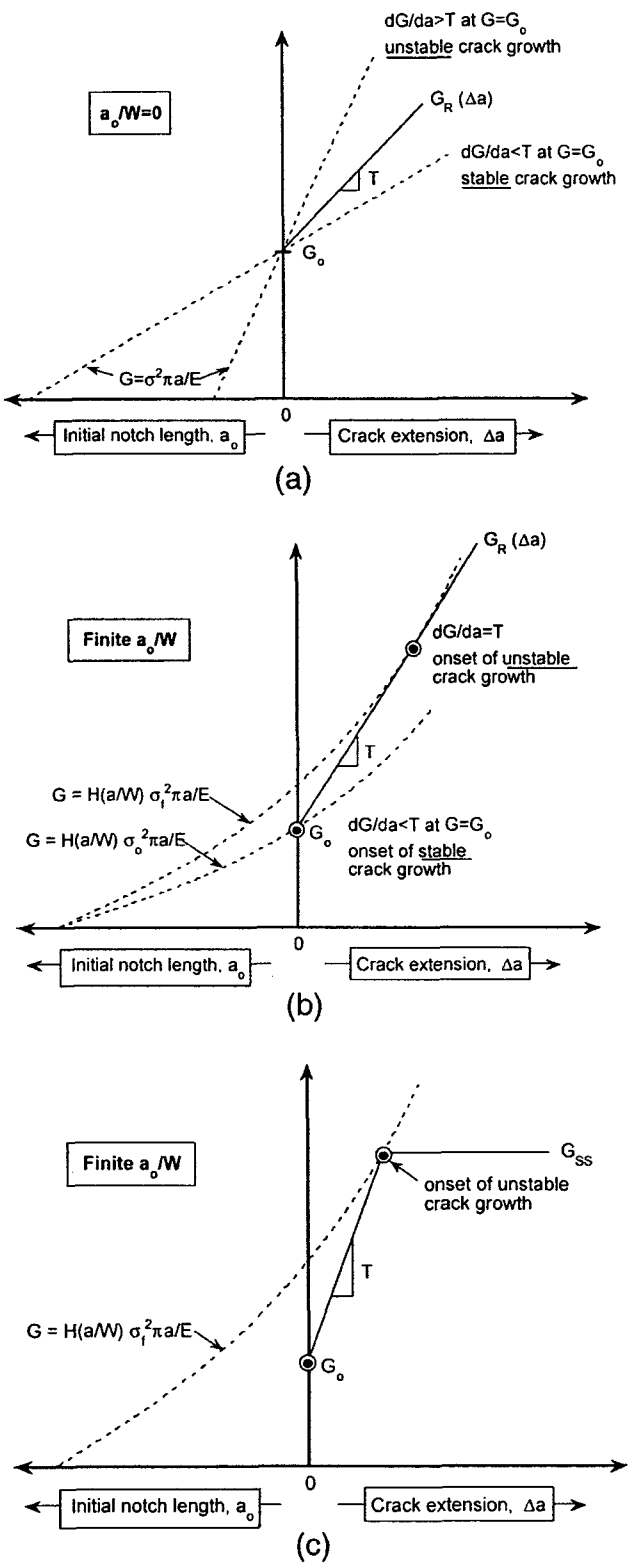


**Fig. 1.** Tangent construction plots, showing the following: (a) the transition from stable to unstable crack growth for $a_0/W = 0$; (b) stable crack growth (starting at $\sigma_0$) and onset of instability (at $\sigma_f$) in the linear portion of the resistance curve for finite $a_0/W$; and (c) unstable crack growth at the steady-state toughness. (Here the material is assumed to be elastically isotropic such that $g(\rho,\lambda) = 1$.)

$$\frac{a_0}{W} = \frac{a_f}{W} - \left(\frac{W}{a_f} + \left(\frac{1}{H(a_f/W)}\right)\frac{dH(a_f/W)}{d(a/W)}\right)^{-1} + \frac{G_0}{TW} \tag{10a}$$

$$\frac{G_f}{G_0} = \frac{WT}{G_0}\left(\frac{W}{a_f} + \left(\frac{1}{H(a_f/W)}\right)\frac{dH(a_f/W)}{d(a/W)}\right)^{-1} \quad (10b)$$

$$\frac{\sigma_f^2 \pi W}{\bar{E} G_0} = \frac{TW}{G_0}\left(\frac{1}{(a_f/W)\, H(a_f/W)\, g(\rho,\lambda)}\right) \times \left(\frac{W}{a_f} + \left(\frac{1}{H(a_f/W)}\right)\frac{dH(a_f/W)}{d(a/W)}\right)^{-1} \quad (10c)$$

If the predicted critical resistance $G_f$ exceeds $G_{ss}$ (Fig. 1(c)), the strength is obtained at $G = G_{ss}$ at a total crack length,

$$a_{ss} = a_0 + \Delta a_{ss} = a_0 + \frac{G_{ss} - G_0}{T} \quad (11)$$

The corresponding stress is

$$\frac{\sigma_f^2 \pi W}{\bar{E} G_0} = \left\{ H(a_{ss}/W)\, g(\rho,\lambda)\left[\frac{a_0}{W}\left(\frac{G_0}{G_{ss}}\right) + \frac{G_0}{TW}\left(1 - \frac{G_0}{G_{ss}}\right)\right]\right\}^{-1} \quad (12)$$

## III. Results Common Test Configurations

Results for a number of notched configurations commonly used for material characterization have been computed using the analysis in Section II along with established solutions for $H(a/W)$. The configurations of interest are as follows: (i) center-notched tension (CNT), (ii) single-edge-notched tension (SENT), (iii) double-edge-notched tension (DENT), (iv) single-edge-notched (pure) bending (SENB), and (v) single-edge-notched beam in three-point bending (SENTPB) with a span to width ratio of $S/W = 4$. Pertinent solutions for $H(a/W)$ are summarized in Table I;[10] each is accurate within 0.5% over the entire range of $a/W$.

Straightforward analytical results for the critical tearing modulus are obtained for the limiting case in which the uncracked ligament becomes small; i.e., $a_0/W \to 1$. For SENT, SENTPB, and SENB, the limiting solutions for $H(a_0/W)$ take the form[10]

$$H(a_0/W) = \frac{\beta_1}{(1 - a_0/W)^3} \quad (13)$$

where $\beta_1$ depends on the loading configuration but is independent of $a_0/W$. Combining this result with Eq. (8) yields

$$\frac{T_c W}{G_0} = \frac{2 + W/a_0}{1 - a_0/W} \quad (14)$$

Similarly, for both CNT and DENT, the limiting solutions for $H(a_0/W)$ take the form[10]

$$H(a_0/W) = \frac{\beta_2}{(1 - a_0/W)} \quad (15)$$

where $\beta_2$ is another constant, independent of $a_0/W$. Combining with Eq. (8) yields

$$\frac{T_c W}{G_0} = \frac{1}{(a_0/W)(1 - a_0/W)} \quad (16)$$

Figure 2 shows the variation in the critical tearing modulus, $T_c W/G_0$, with notch length for the five loading configurations[†] (Eq. (8) and Table I) as well as for the limiting cases of short notches and short ligaments. In each of the former cases, $T_c W/G_0$ exhibits a minimum at a notch length in the range $a_0/W \approx 0.3$–$0.5$ and becomes large in the limits $a_0/W \to 0$ and $a_0/W \to 1$. Thus, for a prescribed value of $TW/G_0$, crack stability is only obtained over an intermediate range of $a_0/W$; both short notches and long notches promote unstable growth. Furthermore, $T_c W/G_0$ approaches the short notch limit (Eq. (6)) when $a_0/W \leq 0.1$ and the pertinent short ligament limit (Eq. (14) or (16)) when $a_0/W \geq 0.9$.

The figure also shows the sensitivity of $T_c W/G_0$ to the specimen type. DENT exhibits the lowest value over the entire range of $a_0/W$ and hence the greatest propensity for stable crack growth. SENT is at the other extreme with the highest value of $T_c W/G_0$, by as much as a factor of 2–3 relative to that for DENT. CNT, SENTPB, and SENB give intermediate results.

The effects of the normalized tearing modulus, $TW/G_0$, on crack stability in the SENB specimen are illustrated in Fig. 3. For the purpose of identifying the range of notch lengths over which crack stability is obtained at initiation, the critical tearing modulus is replotted in Fig. 3(a) and compared with selected values of $TW/G_0$: 10, 20, and 30. The critical points are indicated by the solid symbols and labeled a–f. The amount of crack growth (Eq. (10a)),

[†]Results for SENTPB and SENB are almost indistinguishable from one another. For clarity, the former results are not included in the figure.

**Table I. Summary of the Functions $H(a/W)$ for Common Loading Configurations (from Ref. 8)**

| Loading configuration | $\lvert H(a/W)\rvert^{1/2}$ |
|---|---|
| CNT | $[1 - 0.025(a/W)^2 + 0.06(a/W)^4]\sqrt{\sec\left(\frac{\pi a}{2W}\right)}$ |
| SENT | $\sqrt{\frac{2W}{\pi a}\tan\left(\frac{\pi a}{2W}\right)}\left[\frac{0.752 + 2.02(a/W) + 0.37\left(1 - \sin\left(\frac{\pi a}{2W}\right)\right)^3}{\cos\left(\frac{\pi a}{2W}\right)}\right]$ |
| DENT | $\frac{1.122 - 0.561(a/W) - 0.205(a/W)^2 + 0.471(a/W)^3 - 0.190(a/W)^4}{\sqrt{1 - a/W}}$ |
| SENB | $\sqrt{\frac{2W}{\pi a}\tan\left(\frac{\pi a}{2W}\right)}\left[\frac{0.923 + 0.199\left(1 - \sin\left(\frac{\pi a}{2W}\right)\right)^4}{\cos\left(\frac{\pi a}{2W}\right)}\right]$ |
| SENTPB ($S/W = 4$) | $\frac{1.99 - (a/W)(1 - a/W)(2.15 - 3.93(a/W) + 2.7(a/W)^2)}{\sqrt{\pi}(1 + 2a/W)(1 - a/W)^{3/2}}$ |

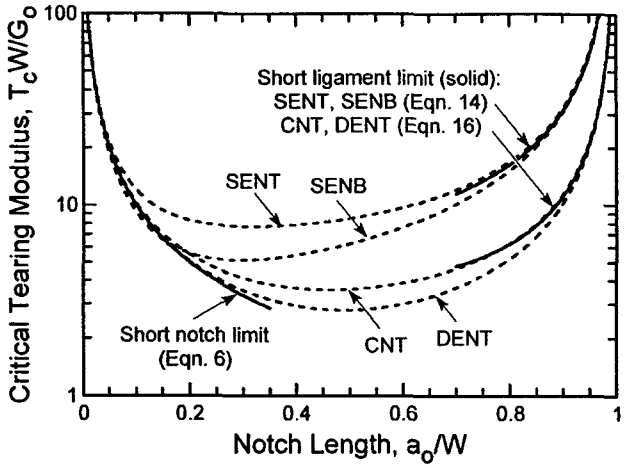


**Fig. 2.** Effects of notch length and specimen type on the critical tearing modulus above which stable crack growth occurs.

the fracture resistance (Eq. (10*b*)), and the stress at instability (Eq. (10*c*)) are plotted in Figs. 3(b–d), respectively, along with the critical points, a–f. Outside the range that leads to stable crack growth (e.g., to the left of b or to the right of e for $TW/G_0 = 20$), unstable growth occurs at $G_f/G_0 = 1$ at the Griffith stress (Eq. (9), Fig. 3(c)). In the intermediate range of $a_0/W$, some stable crack growth is obtained (Fig. 3(b)) and the strength is elevated relative to the Griffith stress. The amount of strength elevation and the range of notch lengths over which this benefit is realized increases with increasing $TW/G_0$.

It is noteworthy that when viewed over an intermediate range of $a_0/W$, the *shapes* of the strength curves (Fig. 3(d)) are not strikingly different from one another. Consequently, experimental measurements of strength for several notch sizes could be misinterpreted using linear elastic fracture mechanics (LEFM), assuming a uniquely valued toughness, and thus the effects of the resistance curve could be overlooked. A more critical distinction can be made by also performing tests on specimens of different widths to vary $TW/G_0$, or on other specimen types, especially ones that yield substantially different values of $T_cW/G_0$.

To illustrate the effects of specimen type, results are presented in Fig. 4(a) for the two extreme cases: SENT and DENT. To distinguish the results from those obtained from LEFM, they are replotted in Fig. 4(b) in terms of $\sigma_f/\sigma_0$. The latter ratio represents the strength elevation above the Griffith stress due to the resistance curve. The results demonstrate that the beneficial effects of the rising fracture resistance are more pronounced in DENT than in SENT. For instance, for $TW/G_0 = 20$, the maximum strength elevation above the initiation stress is only about 18% at $a_0/W \approx$

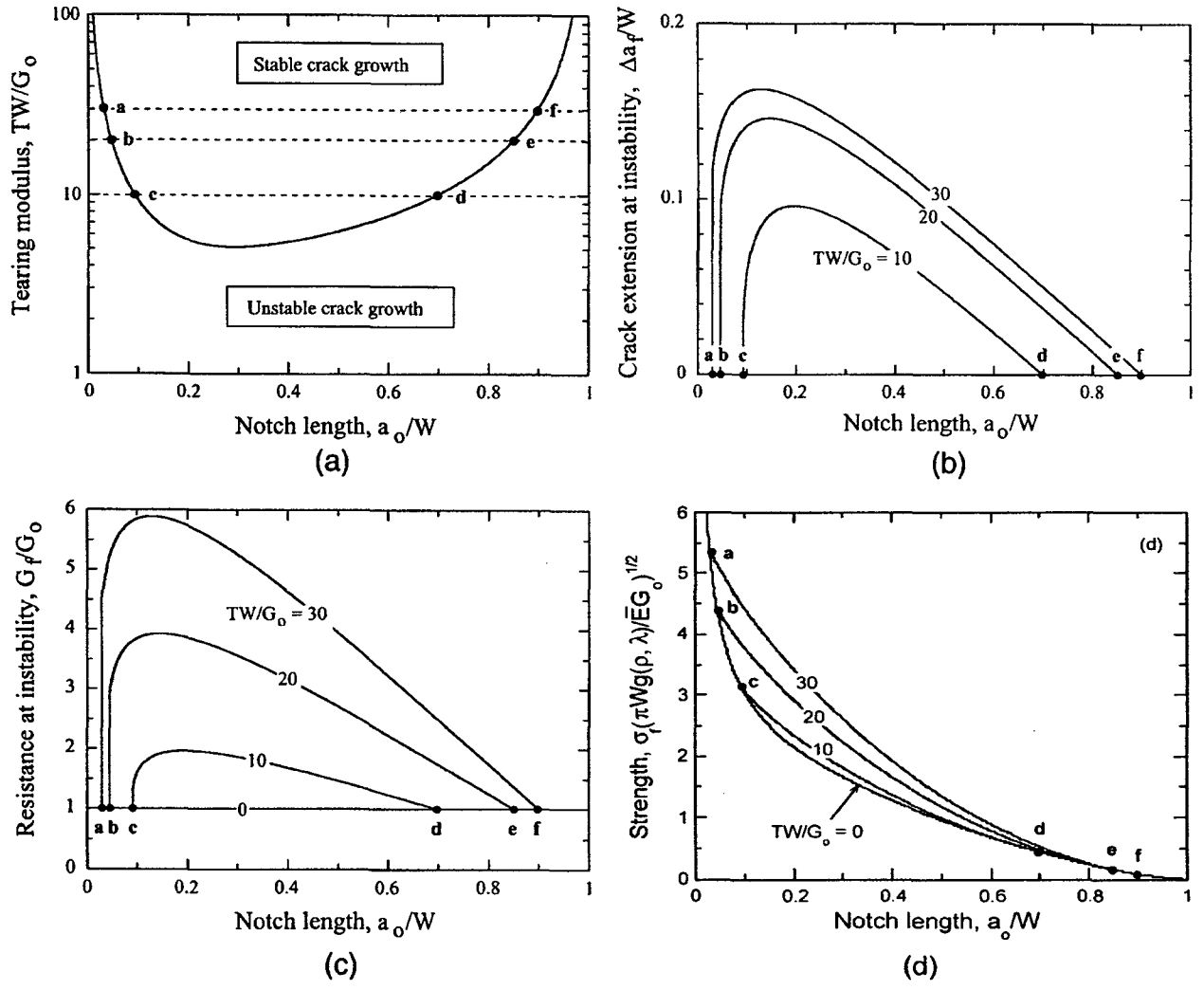


**Fig. 3.** Effects of tearing modulus on crack stability and strength for SENB.

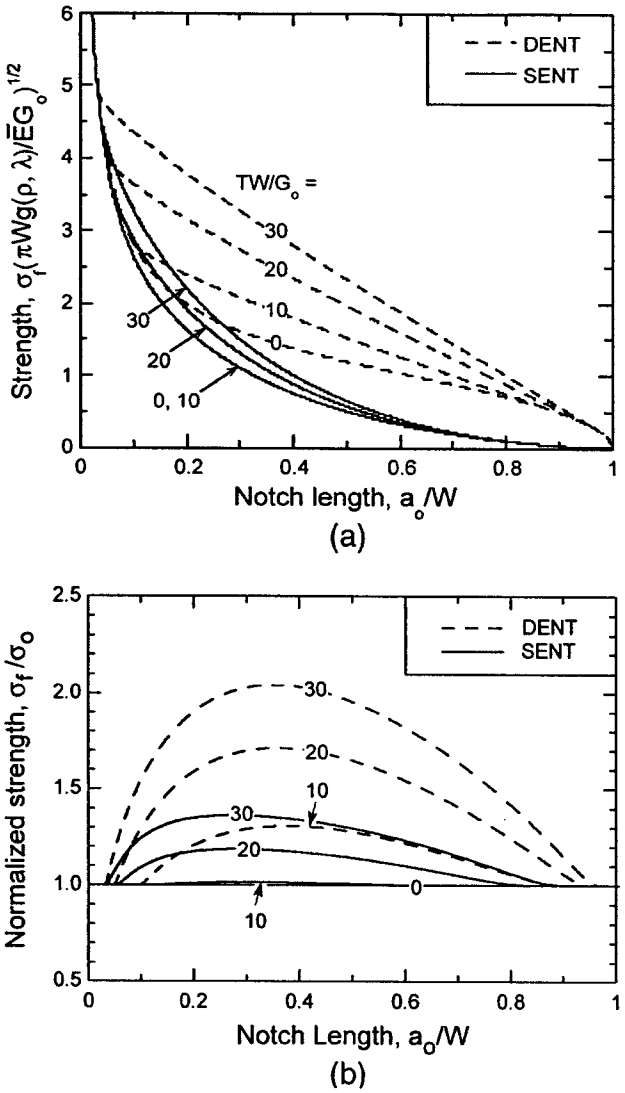


**Fig. 4.** Effects of specimen type on strength. Note that the benefits of the resistance curve are significantly greater for DENT than for SENT in the intermediate range of $a_0/W$, consistent with the differences in the critical tearing moduli shown in Fig. 2.

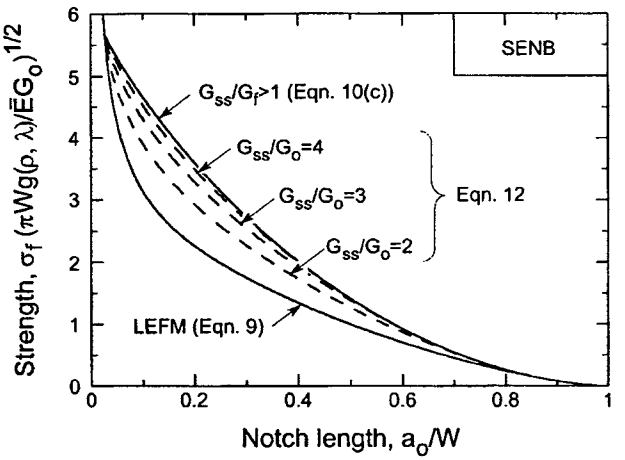


**Fig. 5.** Effects of steady-state toughness on notched strength, when $G_{ss} < G_f$. When $G_{ss} > G_f$ over the entire range of $a_0/W$, the instability occurs in the rising part of the resistance curve and hence the strength is independent of $G_{ss}$.

0.3; the corresponding value for DENT at the same notch length is 70%. It is expected that performing comparative experiments such as these would allow a critical evaluation of the contributions to strength from the resistance curve. Indeed, results of this type are used in designing some of the experiments described below.

The preceding results are based on the assumption that the resistance at fracture is below the steady-state toughness and hence the strength is given by Eq. (10*c*). Otherwise, the strength is given by Eq. (12). One set of illustrative results for the latter case, where $G_f > G_{ss}$, is shown in Fig. 5. They correspond to the SENB geometry for several values of $G_{ss}/G_0$ at a fixed value of $TW/G_0$. The results from Eqs. (9) and (10*c*) bound those from Eq. (12) when $G_{ss}/G_0$ falls below the maximum value of $G_f/G_0$ (Fig. 3(c)).

## IV. Experimental Procedure

The CFCCs used for experimental measurements comprise seven layers of 3000 denier Nextel 720 fiber cloth in an 8-harness satin weave and a porous mullite–alumina matrix. The matrix was introduced in two steps: (i) pressure-assisted infiltration of a mullite–alumina slurry through the fiber preform and (ii) impregnation and pyrolysis of an $Al_2Cl(OH)_5$ solution (an alumina precursor). Processing details were essentially identical to those described earlier[11] with two exceptions. First, the concentration of the precursor solution was increased to give a volumetric yield of 6.4%, compared with 3% in previous studies. The more concentrated solution allows a prescribed matrix density to be achieved with fewer impregnation and pyrolysis cycles. In the present study, four such cycles were used, yielding a final matrix porosity of 32%. Second, to prevent segregation of the precursor during drying, the panels were gelled immediately after precursor impregnation by immersing them in an $NH_4OH$ environment for 6 h. The absence of segregation was confirmed through a series of matrix hardness measurements across the plate thickness. The composite panel thickness was 3.3 mm.

As a parenthetical note, the matrix in the present composite had been designed to be considerably harder than that in composites described in earlier studies.[12,13] This selection was motivated by the attendant improvements in the off-axis properties, e.g., 0°/90° shear strength. Although not reported here, significant elevations in shear properties are indeed obtained with increasing matrix hardness. A comparative study on the effects of matrix hardness on the composite performance in both matrix- and fiber-dominated loadings will be reported elsewhere.

In-plane elastic properties were obtained from unnotched tension and Iosipescu shear tests, performed parallel to the fiber directions. The tensile specimens were of a dog-bone configuration with a gauge section 8 mm wide and 60 mm long. The Iosipescu specimens were 19 mm wide and contained a pair of V-notches with an included angle of 105°, to a depth of 3.8 mm. Both specimen types were instrumented with strain gauges. The key results from these tests are as follows: $E_1$ = 64 GPa, $\nu_{12}$ = 0.13, and $\mu_{12}$ = 14 GPa. Combining with Eqs. (3) and (4) yields $\rho$ = 2.15 and $g(\rho)$ = 1.51.

Additional mechanical tests were performed in the 0°/90° orientation on three types of notched specimens: SENTPB, SENT, and DENT. The geometric parameters were selected to probe the effects of $W$ at fixed $a_0/W$ and the effects of $a_0/W$ at fixed $W$. The pertinent values are listed in Table II. For SENTPB, the span length was $S/W$ = 4. The length of the SENT specimens was $H/W$ = 1.0; for the DENT specimens, $H/W \geq 3$. Crack-growth measurements were made using crack gauges affixed to the specimen surface (Krak-Gauge, model A05-CE, Hartrun Corp., St. Augustine, FL). These measurements were checked against direct optical measurements on the opposing surface. Image contrast was enhanced by coating the viewing surfaces with Au–Pd. The cracks were observed to be essentially planar, with no evidence of inelastic deformation or damage away from the crack tip. The nominal fracture resistance was calculated via Eq. (7), using the

**Table II. Notched Loading Configurations Used in the Experiments**

| | $a_0/W$ | $W$ (mm) | $S/W$ | $H/W$ |
|---|---|---|---|---|
| SENTPB | 0.5 | 6, 12, 24 | 4 | – |
| SENT | 0.5 | 6, 12, 24 | – | 1.0 |
| | 0.35, 0.5, 0.65 | 24 | – | 1.0 |
| DENT† | 0.5 | 6, 12 | – | ≥3 |

†Following the usual convention for DENT specimens, the full specimen width is denoted $2W$, its length is $2H$, and the length of each of the two notches is $a_0$.

measured load and crack length, coupled with the computed value of $H(a/W)$ and $g(\rho) = 1.51$. For SENT, the effects of specimen rotation in the gripped sections were incorporated using the approach described in the Appendix. The SENTPB specimens were also instrumented with a spring-loaded one-armed extensometer to monitor load–line displacement. The work of fracture, obtained from the area under the load–displacement curve, was used as a measure of the steady-state toughness.[14] Base-line values of unnotched strength were obtained from uniaxial tension tests (described above) and four-point bend tests. The bend specimens were either 6 or 12 mm wide and loaded with a span $S/W \approx 9$.

The experimental results are summarized in Figs. 6 and 7. In all cases, stable crack growth had been observed before the stress maximum and the resistance curves were essentially linear. All the tensile geometries yielded common resistance parameters:‡ notably, $G_0 \approx 900 \pm 200$ J/m$^2$ and $T = 400 \pm 100$ kJ/m$^3$. In contrast, the SENTPB specimens exhibited significantly higher fracture resistance, characterized by $G_0 \approx 1500 \pm 150$ J/m$^2$ and a tearing modulus $T = 950 \pm 100$ kJ/m$^3$. It is surmised that the differences are associated with the $T$-stresses and their effect on inelasticity in the notch tip region. That is, for SENTPB, the $T$-stress is positive over the range of $a_0/W$ used in the present experiments.[9] When positive, the $T$-stress promotes matrix microcracking ahead of the notch tip which, in turn, reduces the normal stress along the incipient fracture plane and hence increases fracture resistance.[13] In contrast, for the tensile geometries, the $T$-stress is negative over the pertinent range of $a_0/W$, suppressing the inelasticty that leads to increased resistance.

The one notable exception to the behavior described above pertains to the narrowest SENTPB specimens. In this case, the fracture resistance was anomalously low (relative to that measured on the wider specimens) and the notched strength was essentially equal to the unnotched strength. Evidently, fracture is controlled by the net-section stress rather than the $K$-field associated with the notch. Consequently, the analysis presented here does not apply.

## V. Comparisons between Experiment and Theory

Notched strength predictions were made using the analysis presented in Section II and the range of resistance parameters shown in Fig. 7: $G_0 = 1500 \pm 150$ J/m$^2$ and $T = 950$ kJ/m$^3$ for flexure and $G_0 = 900 \pm 200$ J/m$^2$ and $T = 400$ kJ/m$^3$ for tension. The results are plotted in Fig. 6. Also shown for comparison are the values obtained from LEFM: notably, the Griffith stress (Eq. (9)), calculated using the initiation toughness. The transition between the two corresponds to $T_c W/G_0$. Broadly, the predictions correlate well with the experimental measurements

Viewed collectively, the results provide insights into the transitions in behavior with increasing notch length. For instance, for the SENT specimens with $a_0/W = 0.5$, three domains exist: (i) net-section-stress-dominated, denoted I, for $a_0 \leq 1$ mm, (ii)

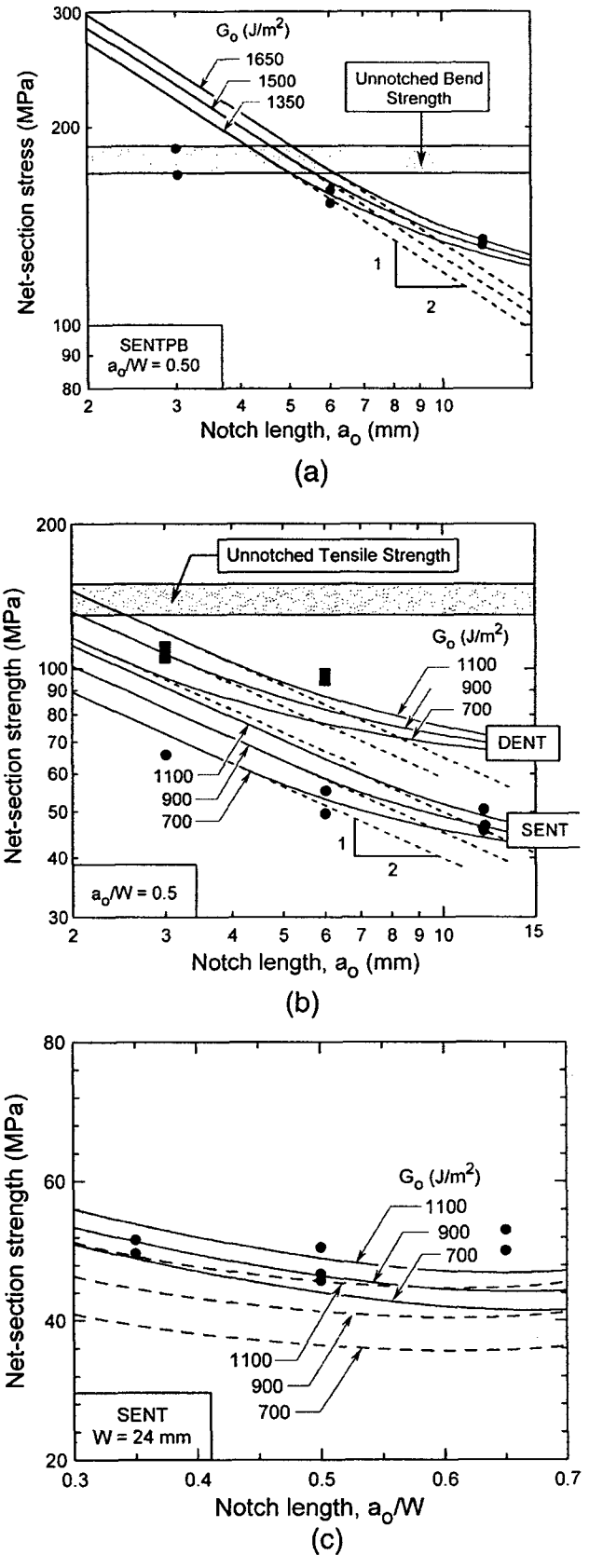


**Fig. 6.** Notched strength of oxide composite: (a) SENTPB, $a_0/W = 0.5$; (b) DENT and SENT, $a_0/W = 0.5$; and (c) SENT, $W = 24$ mm. Solid symbols represent individual experimental measurements, solid lines are values predicted from the model, and dashed lines are from LEFM.

‡The tearing modulus was obtained through a linear regression analysis of the resistance curve for crack growth up to $\Delta a/W \approx 0.25$. The curves exhibited nonlinearity beyond this point, a manifestation of large-scale bridging. In all pertinent cases, the peak stress was attained when the crack was within the linear portion of the resistance curve.

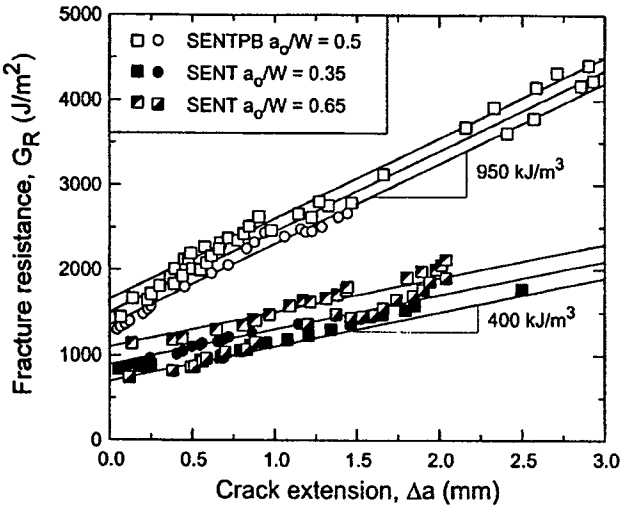


**Fig. 7.** Typical fracture resistance curves obtained from SENTPB and SENT tests. Lines represent envelope of fit values, with $G_0$ = 1500 ± 150 J/m² and $T$ = 950 kJ/m³ for flexure and $G_0$ = 900 ± 200 and $T$ = 400 for tension. The steady-state toughness obtained from SENTPB tests is $G_{ss}$ = 5300 ± 400 J/m², well beyond the values relevant to the regime where instability occurs.

initiation-dominated, denoted II, for 1 mm ≤ $a_0$ ≤ 5 mm, and (iii) $T$-dominated, denoted III, for $a_0$ ≥ 5 mm. For the SENTPB specimens, the transition from I to II occurs at stresses that are essentially the same as the unnotched strength. The implication is that the behavior transitions directly from I to III without passing through II.

To further explore these transitions, calculations have been performed for other values of $a_0/W$. Representative results for the SENTPB geometry with $a_i/W$ in the range 0.25–0.75 are plotted in Fig. 8; similar trends are obtained for the other geometries. For clarity, results are presented only for the *average* values of the initiation toughness ($G_0$ = 1500 J/m²), the tearing modulus ($T$ = 950 kJ/m³), and the steady-state toughness ($G_{ss}$ = 5300 J/m²). Furthermore, they are presented over a broad range of notch lengths to capture the full range of behavior. Two new features are notable. First, there exists an

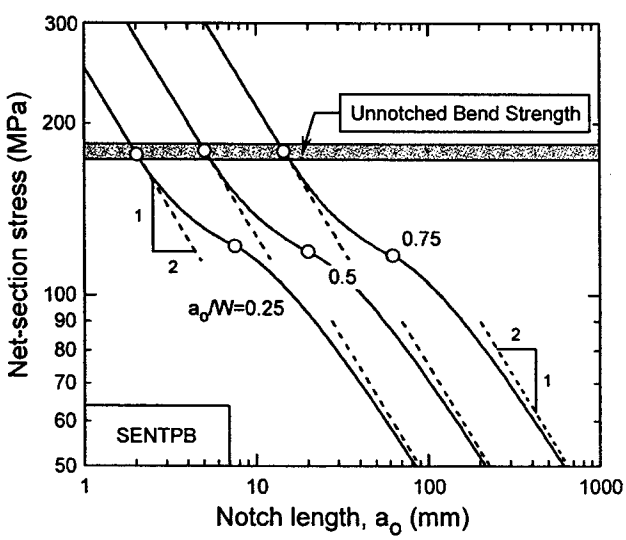


**Fig. 8.** Effects of $a_0/W$ on notched strength of SENTPB specimen. The open circles show the behavioral transitions. For the transition II → III (top row of circles), the critical notch length is given by Eq. (8); for the transition III → IV (lower row of circles), it is given by Eq. (11).

additional domain, denoted IV, for the longest notches, where the strength is dictated by the steady-state toughness. In this domain, the notched strength asymptotically approaches an inverse square root dependence on notch length, analogous to that of the initiation-dominated domain. Second, the notch lengths corresponding to the transitions increase substantially with increasing $a_0/W$. For instance, for a very deep notch, characterized by $a_0/W$ = 0.75, the transition from I to II occurs for $a_0$ ≈ 14 mm. In contrast, with notches of this length in a specimen with $a_0/W$ = 0.25, the behavior is well within domain IV. As a consequence, striking differences in behavior would be obtained over the practical range of notch lengths, from 2 to 14 mm. In the former case ($a_0/W$ = 0.75), the strength would be indistinguishable from the unnotched strength; in the latter ($a_0/W$ = 0.25), significant notch sensitivity would be apparent. The latter tests are recommended to most critically probe notch effects.

## VI. Concluding Remarks

A theoretical framework for predicting the notch sensitivity of strength of ceramic composites with rising fracture resistance has been presented. An attractive feature of the resulting solutions is their relatively simple analytical form: a consequence of the assumed linear form of the resistance curve. The framework provides a consistent description of the strength of the oxide composite studied here when the notch length is large and the corresponding strength is low in relation to the unnotched strength. Parametric studies illustrate the salient features in the transitions in fracture behavior and their dependence on both the notch length and its normalized value ($a_0/W$).

In addition to its use in rationalizing experimental results, the theoretical framework should find utility in designing critical experiments to probe notch sensitivity of other composite materials. For instance, with preliminary estimates of $G_0$ and $T$, calculations could be performed to identify the specimen sizes and types for which stable crack growth should occur and experiments performed accordingly. This combined theoretical/experimental approach is expected to yield significantly improved understanding of notch sensitivity relative to that obtained through an *ad hoc* experimental program.

On a cautionary note, the framework is not expected to apply to composites that exhibit large-scale inelasticity in the notch-tip region. In composites with weak (porous) matrixes, such inelasticity can occur through a shear mode parallel to the loading direction.[15] Alternatively, in systems with strong (dense) matrixes, it can occur in a tensile mode through multiple matrix cracking.[15,16] When the spatial extent of the inelasticity becomes comparable to the structural dimensions, the inelasticity must to be taken into account explicitly[13,16] and not simply embodied in the initiation toughness.

Finally, the degree of notch sensitivity displayed by the present oxide composite is significantly greater than that in systems with weaker matrixes.[12,13] However, the lower notch sensitivity associated with weaker matrixes is accompanied by reductions in off-axis properties, notably the 0°/90° shear strength. Trade-offs between fiber-dominated and matrix-dominated properties are the subject of a current investigation.

## Appendix

Experience with the SENT geometry indicates that small amounts of specimen rotation can occur under nominally fixed grip conditions, thereby altering the associated stress intensity factor. The magnitude of this effect is determined from measurements of the crack-mouth-opening displacement (CMOD) coupled with the following analysis.[17]

The stresses at the specimen ends can be partitioned into two components: (i) a uniform tensile stress, $\sigma_T$, equal to the average measured stress and (ii) a bending stress, $\sigma_B$, proportional to $\sigma_T$,

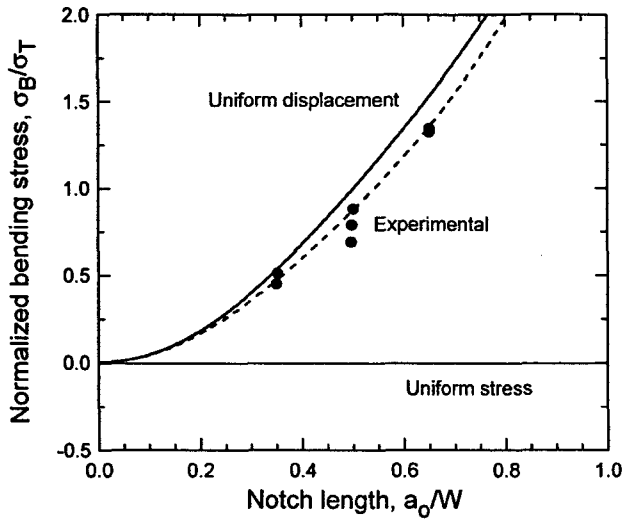


**Fig. 9.** Effects of specimen rotation on the normalized bending stress. Solid symbols represent individual experimental measurements, solid lines are values predicted from the two limiting end conditions, and the dashed line is an empirical fit to the experimental data.

but of unknown magnitude. The stress intensity factor associated with these two stress components is

$$K = F_T(a/W)\, Y(\rho)\sigma_T \sqrt{\pi a} - F_B(a/W)\, Y(\rho)\sigma_B \sqrt{\pi a}$$
$$\equiv F_E(a/W)\, Y(\rho)\sigma_T \sqrt{\pi a} \qquad \text{(A-1)}$$

where

$$Y(\rho) = 1 + 0.1(\rho - 1) - 0.016(\rho - 1)^2 + 0.002(\rho - 1)^3 \qquad \text{(A-2)}$$

Here, $F_T(a/W)$ and $F_B(a/W)$ are the nondimensional functions for SENT and SENB given in handbooks,[10] $F_E(a/W)$ is the function that characterizes the stress intensity factor in the present test configuration, and $Y(\rho)$ accounts for material orthotropy.[7,8] The corresponding CMOD is

$$\delta = \frac{g(\rho,\lambda)}{Y(\rho)}\left[ V_T(a/W)\left(\frac{4\sigma_T a}{\bar{E}}\right) - V_B(a/W)\left(\frac{4\sigma_B a}{\bar{E}}\right)\right] \qquad \text{(A-3)}$$

where $V_T(a/W)$ and $V_B(a/W)$ are the nondimensional functions for CMOD obtained from handbooks, and $g(\rho,\lambda)$ characterizes the material orthotropy as described in Section II. Rearranging Eq. A-3 yields the stress ratio:

$$\frac{\sigma_B}{\sigma_T} = \frac{V_T}{V_B} - \frac{Y(\rho)}{V_B g(\rho,\lambda)}\left(\frac{\delta \bar{E}}{4a\sigma_T}\right) \qquad \text{(A-4)}$$

Combining Eqs. A-1 and A-4 gives the normalized stress intensity factor as

$$F_E = \frac{K}{\sigma_T \sqrt{\pi a}}$$
$$= F_T - F_B\left(\frac{\sigma_T}{\sigma_B}\right)$$
$$= F_T - \frac{F_B}{V_B}\left[V_T + \frac{Y(\rho)}{g(\rho,\lambda)}\left(\frac{\delta \bar{E}}{4a\sigma_T}\right)\right] \qquad \text{(A-5)}$$

The stress intensity factor had been obtained from Eq. A-5 coupled with measurements of $\delta$ in the elastic regime and the known values of the other parameters.

The degree to which the bending stress had been reduced relative to the uniform displacement condition was ascertained from a comparison of the experimentally determined stress ratio in Eq. A-4 with the predicted value. The results are plotted in Figure 9. Evidently the experimental results lie close to, but slightly below, those for the uniform displacement condition.[18] The dashed line in the figure shows an empirical fit through the data, given by the product of the uniform displacement solution and $m(a/w) = 1 - 0.5(a/w)(1 - a/W)$. This fit accurately represents the experimental data and provides the correct limits to the stress ratio in the limits of $a/W \to 0$ and $a/W \to 1$.

## Nomenclature

| | |
|---|---|
| $a$ | Crack length |
| $a_0$ | Initial crack or notch length |
| $a_f$ | Total crack length at unstable crack growth |
| $a_{ss}$ | Total crack length at onset of steady state |
| $a_{ch}$ | Characteristic bridging length scale |
| $E$ | Young's modulus |
| $\bar{E}$ | Plane strain Young's modulus |
| $g(\rho, \lambda)$ | Orthotropy function (Eqs. 1 and 4) |
| $G$ | Energy release rate |
| $G_f$ | Fracture resistance at unstable crack growth |
| $G_0$ | Initiation toughness |
| $G_R$ | Fracture resistance |
| $G_{ss}$ | Steady-state toughness |
| $H$ | Nondimensional function (Table I) |
| $S$ | Loading span |
| $T$ | Tearing modulus |
| $T_c$ | Critical tearing modulus |
| $u_*$ | Critical crack opening displacement |
| $W$ | Specimen width |
| $Y(\rho)$ | Orthotropy function (Eq. A-2) |
| $\Delta a$ | Crack growth |
| $\Delta a_{ss}$ | Crack growth at onset of steady state |
| $\lambda$ | Elastic orthotropy parameter (Eq. 2) |
| $\mu$ | Shear modulus |
| $\nu$ | Poisson's ratio |
| $\rho$ | Elastic orthotropy parameter (Eq. 3) |
| $\sigma$ | Stress |
| $\sigma_f$ | Stress at onset of unstable crack growth |
| $\sigma_0$ | Stress at onset of crack growth |
| $\sigma_u$ | Unnotched strength |
| $\sigma_*$ | Characteristic bridging stress |

## References


[1]Z. Suo, S. Ho, and X. Gong, "Notch Ductile-to-Brittle Transition Due to Localized Inelastic Band," *J. Eng. Mater. Technol.—Trans. ASME*, **115** [3] 319–26 (1993).

[2]B. N. Cox, "Extrinsic Factors in the Mechanics of Bridged Cracks," *Acta Metall. Mater.*, **39** [6] 1189–201 (1991).

[3]G. Bao and F. Zok, "On the Strength of Ductile Particle Reinforced Brittle Matrix Composites," *Acta Metall. Mater.*, **41** [12] 3515–24 (1993).

[4]B. Budiansky and Y. L. Cui, "Toughening of Ceramics by Short Aligned Fibers," *Mech. Mater.*, **21** [2] 139–46 (1995).

[5]R. F. Cook and D. R. Clarke, "Fracture Stability, *R*-Curves and Strength Variability," *Acta Metall.*, **36** [3] 555–62 (1988).

[6]B. Lawn, *Fracture of Brittle Solids*, 2nd ed. Cambridge University Press, Cambridge, U.K., 1993.

[7]Z. Suo, G. Bao, B. Fan, and T. C. Wang, "Orthotropy Rescaling and Implications for Fracture in Composites," *Int. J. Solids Struct.*, **28** [2] 235–48 (1991).

[8]G. Bao, S. Ho, Z. Suo, and B. Fan, "The Role of Material Orthotropy in Fracture Specimens for Composites," *Int. J. Solids Struct.*, **29** [9] 1105–16 (1992).

[9]T. L. Anderson, *Fracture Mechanics: Fundamentals and Applications*, 2nd ed. CRC Press, Boca Raton, FL, 1995.

[10]H. Tada, *The Stress Analysis of Cracks Handbook*, 2nd ed. Paris Productions Inc., St. Louis, MO, 1985.

[11]M. Mattoni, J. Y. Yang, C. G. Levi, and F. W. Zok, "Effects of Matrix Porosity on the Mechanical Properties of a Porous-Matrix, All-Oxide Ceramic Composite," *J. Am. Ceram. Soc.*, **84** [11] 2594–602 (2001).

[12]C. G. Levi, J. Y. Yang, B. J. Dalgleish, F. W. Zok, and A. G. Evans, "Processing and Performance of an All-Oxide Ceramic Composite," *J. Am. Ceram. Soc.*, **81** [8] 2077–86 (1998).

[13]J. A. Heathcote, X. Y. Gong, J. Y. Yang, U. Ramamurty, and F. W. Zok, "In-Plane Mechanical Properties of an All-Oxide Ceramic Composite," *J. Am. Ceram. Soc.*, **82** [10] 2721–30 (1999).

[14]H. G. Tattersall and G. Tappin, "The Work of Fracture and Its Measurement in Metals, Ceramics and Other Materials," *J. Mater. Sci.*, **1**, 296–301 (1966).

[15]A. G. Evans and F. W. Zok, "The Physics and Mechanics of Fibre-Reinforced Brittle Matrix Composites," *J. Mater. Sci.*, **29** [15] 3857–96 (1994).

[16]J. C. McNulty, F. W. Zok, G. M. Genin, and A. G. Evans, "Notch-Sensitivity of Fiber-Reinforced Ceramic-Matrix Composites: Effects of Inelastic Straining and Volume-Dependent Strength," *J. Am. Ceram. Soc.*, **82** [5] 1217–28 (1999).

[17]M. Mattoni and F. W. Zok, "A Method for Determining the Stress Intensity Factor of a Single Edge-Notched Tensile Specimen," *Int. J. Fract. Lett.*, **119**, L3–L8 (2003).

[18]R. John and B. Rigling, "Effect of Height to Width Ratio on K and CMOD Solutions for a Single Edge Cracked Geometry with Clamped Ends," *Eng. Fract. Mech.*, **60** [2] 147–56 (1998).

journal

J. Am. Ceram. Soc., 88 [2] 367–375 (2005)
DOI: 10.1111/j.1551-2916.2005.00061.x

# Controlling Mechanical Properties of Porous Mullite/Alumina Mixtures Via Precursor-Derived Alumina

Hiroki Fujita, Carlos G. Levi, and Frank W. Zok†

Materials Department, University of California, Santa Barbara, CA 93106-5050

George Jefferson

Materials and Manufacturing Directorate, AFRL, Wright-Patterson AFB, OH 45433

**This study focuses broadly on synthesis and characterization of porous mullite/alumina mixtures for use as matrices in oxide fiber composites. Specifically, an assessment is made of the utility of a precursor-derived alumina (PDA) in controlling both the modulus and the toughness of mullite-rich particle mixtures. Property changes are probed through models of the mechanical behavior of bonded particle aggregates. Consideration of the conditions needed to cause crack deflection at a fiber–matrix interface yields an upper allowable limit on the concentration of PDA to ensure damage tolerance in a fiber composite. The predicted critical concentration lies in the range of about 7–9%, depending on the mullite/alumina ratio in the particle slurry and the subsequent aging treatment. Values slightly below this limit should yield composites that exhibit a desirable balance between fiber- and matrix-dominated properties.**

## I. Introduction

DAMAGE tolerance can be enabled in oxide ceramic composites through the use of a controlled amount of fine-scale matrix porosity, obviating the need for a fiber coating.[1–4] For successful implementation, the matrix must satisfy three criteria: (i) pore retention at the targeted use temperature, (ii) phase compatibility with the fibers (because of the intimate fiber–matrix contact in the absence of a coating), and (iii) adequate mechanical integrity to ensure acceptable off-axis composite properties. When the reinforcements are either alumina or mullite/alumina fibers, the requisite matrix characteristics can be achieved through the use of mullite/alumina mixtures. Typically, the mullite is in the form of particles, introduced by infiltration of a slurry into the fiber preform. Its main role is to form a contiguous nondensifying network. In contrast, the alumina serves as a binder to impart mechanical strength. It can be introduced in one of two ways: by mixing alumina particles into the slurry, or by subsequent impregnation and pyrolysis of a liquid alumina precursor.[5] These lead to two distinct matrix topologies, illustrated in Fig. 1. The primary objective of the present paper is to compare the efficacy of the two approaches in controlling matrix properties. This is achieved largely through a series of experiments on porous mullite/alumina compacts with varying amounts of precursor-derived alumina (PDA) and comparisons with previously reported measurements on mullite/alumina particle mixtures (without precursor additions).[6] A second objective is to develop and assess models of bonded particle aggregates for use in describing the mechanical properties of compacts containing a precursor-derived phase.

The two routes for introducing alumina have three attributes: (i) The use of a mixed mullite/alumina particle slurry allows both matrix phases to be introduced simultaneously. By contrast, the precursor route requires additional steps, beyond that of slurry infiltration. From a cost viewpoint, the former method is preferred. (ii) The presence of alumina particles in the slurry can compromise the stability of the mullite network, especially if its proportion exceeds the percolation threshold.[6] Conversely, if the slurry is comprised of only mullite and the alumina is introduced subsequently via the precursor route, the contiguity of the mullite network is ensured. (iii) The slurry processing route results in an essentially fixed (high) porosity. Consequently, a modest upper limit on the strength of the network is expected. In contrast, the precursor route allows for filling of the void space between the particles in the network, with attendant elevations in both the relative density and the mechanical properties. A further benefit of the precursor route might be obtained, if, because of capillarity, the PDA forms preferentially at the junctions of the mullite particles. The present experiments were designed to address some of these issues.

To motivate the mechanical measurements, a crack deflection parameter, $\Sigma$, is used, defined by[6,7]

$$\Sigma \equiv 0.134 \left(\frac{\Gamma_f}{\Gamma_m}\right)\left(1+\frac{E_f}{E_m}\right)^{0.9} \quad (1)$$

where $\Gamma$ is the toughness, $E$ is Young's modulus, and subscripts m and f refer to matrix and fiber, respectively. A matrix crack is predicted to arrest or deflect at the fiber–matrix interface when $\Sigma$ exceeds a critical value, defined by $\omega \equiv \Gamma_i/\Gamma_m$, where $\Gamma_i$ is the interface toughness. Since the nature of bonding at the fiber–matrix interface is similar to that between particles in the matrix, the interface toughness is expected to be comparable with that of the matrix, i.e. $\omega \approx 1$. Thus, upon setting $\Sigma = \omega = 1$, the critical combination of $\Gamma_m/\Gamma_f$ and $E_m/E_f$ is obtained. In light of this prediction, the subsequent experimental study focuses on the matrix properties $\Gamma_m$ and $E_m$. An assessment is then made of whether the crack deflection condition is satisfied when a candidate matrix is combined with the targeted fiber, namely Nextel 720.

Despite an extensive literature on the mechanical properties of porous ceramics, only a small fraction of the effort has been devoted to the development and assessment of mechanistic models based on realistic representations of pore topology. Perhaps the greatest deficiency lies in the low porosity domain, wherein the materials consist of particle aggregates bonded to one another at discrete contact points. In this case, macroscopic properties are extremely sensitive to changes in contact size, even when unaccompanied by changes in macroscopic porosity.[6,8,9] Elastic properties of such aggregates have been successfully modeled by treating the particle junctions as Hertzian contacts

K. T. Faber—contributing editor

Manuscript No. 10709. Received December 9, 2003; approved August 2, 2004.

Funding for this work was provided by the Air Force Office of Scientific Research under Contract number F49620-02-1-0128, monitored by Dr. B. L. Lee, as well as a gift from NGK Insulators.

†Author to whom correspondence should be addressed. e-mail: zok@engineering.ucsb.edu

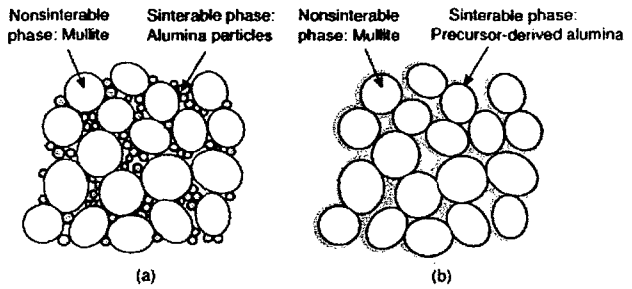


**Fig. 1.** Schematics showing the two matrix topologies produced by (a) mullite/alumina particle mixtures and (b) mullite particles bonded by precursor-derived alumina.

and analyzing the aggregate response accordingly.[10–13] A similar approach has been used in conjunction with the discrete element method (DEM) for simulating the fracture process.[6] Otherwise, most previous studies have relied on purely empirical relations to rationalize experimental measurements, usually couched solely in terms of the porosity level.[8,14–16] Others have implemented models based on rather simplistic (arguably unrealistic) microstructural representations, e.g. a collection of aligned cylinders of varying diameters, each represented mechanically as a one-dimensional spring with stiffness dictated by cylinder diameter.[17,18] Although models of this type can be readily analyzed, they lack the realism needed for establishing connections between microstructure and properties. Analogous phenomenological approaches[19] have proved to be of similarly limited utility in modeling fracture energy.

The present article is organized as follows. Section II describes the nature of the materials systems, the processing route, and the measurement procedures. The resulting physical properties and microstructures are presented in Section III. The key mechanical properties—modulus and toughness—are addressed in Sections IV and V. Section VI considers the implications on crack deflection in fiber composites. For this purpose, the calibrated models are used to establish the critical concentration of the precursor-derived phase at which the crack deflection condition is no longer satisfied. Conclusions are summarized in Section VII. A comprehensive list of key symbols and their definitions is presented in Table I.

## II. Materials and Test Procedures

Porous mullite compacts, 10 mm × 50 mm × 90 mm in size, were fabricated by vacuum filtration, following procedures detailed elsewhere.[5] The particles were MU-107 mullite (Showa Denko K.K., Tokyo, Japan), with an average diameter of 1 μm, dispersed in aqueous $HNO_3$ at a pH of 3. Following filtration, the compacts were dried, sintered at 900°C for 2 h to promote partial sintering at the particle junctions, and machined into mechanical test specimens. Some specimens were subsequently impregnated with an alumina precursor solution, following the procedures described below, and pyrolyzed at 900°C for 2 h. All were subjected to a final aging treatment of either 2 h at 1200°C (representing the as-processed condition) or 1000 h at 1200°C (to assess thermal stability).

The precursor solution was made by slowly digesting Al powder in a solution of $AlCl_3 \cdot 6H_2O$ in deionized water at 85°C. The fractional volumetric yield of alumina was determined by firing known quantities of the precursor solution at either 900° or 1200°C and subsequently measuring both the mass and the density of the pyrolyzed product. The corresponding densities, 3.48 and 3.99 g/cm,[3] are consistent with γ- and α-alumina, respectively. The subsequent yield measurements are reported on the basis of the γ-alumina; the two yields are related by $y_\alpha/y_\gamma = \rho_\gamma/\rho_\alpha \approx 0.87$ where $y$ is the volumetric yield, $\rho$ is the mass density, and the subscripts refer to the two phases.

**Table I. Symbols and Definitions**

| | |
|---|---|
| $a$ | Junction radius |
| $a_0$ | Initial junction radius (before precursor impregnation) |
| $A$ | Surface area per particle |
| $A_0$ | Initial surface area per particle (before precursor impregnation) |
| $E_f$ | Fiber Young's modulus |
| $E_m$ | Matrix Young's modulus |
| $E_s$ | Young's modulus of solid phase |
| $h_0$ | Height of truncated spherical cap (Fig. A1) |
| $n$ | Sintering exponent |
| $p_0$ | Initial compact porosity (before precursor impregnation) |
| $p$ | Final porosity |
| $t$ | Time |
| $t_R$ | Reference time |
| $R$ | Particle radius |
| $R_{eff}$ | Effective particle radius |
| $V_{PDA}$ | Volumetric concentration of precursor-derived alumina |
| $V_0$ | Particle volume |
| $y_\alpha$ | Fractional volumetric yield (α-phase) |
| $y_\gamma$ | Fractional volumetric yield (γ-phase) |
| $\alpha$ | Normalize junction size ($a/R_{eff}$) |
| $\alpha_0$ | Normalize initial junction size ($a_0/R$) |
| $\beta$ | Nondimensional precursor "segregation" parameter |
| $\Gamma_f$ | Fiber toughness |
| $\Gamma_m$ | Matrix toughness |
| $\Gamma_i$ | Interface toughness |
| $\Gamma_j$ | Junction toughness |
| $\rho$ | Mass density |
| $\Sigma$ | Crack deflection parameter (Eq. (1)) |
| $\omega$ | Toughness ratio ($\Gamma_i/\Gamma_j$) |

The precursor concentration was selected in the following way. To achieve large porosity reductions with minimal impregnation cycles, concentrated solutions are preferred. However, a practical upper limit on the allowable solution concentration is obtained because of solution viscosity and compact permeability. That is, solution impregnation into the compact at atmospheric pressure becomes impractical when the concentration, and hence viscosity, are excessively high. An experimental determination of this limit was made by impregnating samples of known porosity with solutions of varying concentrations, firing at 900°C, and measuring the weight gain because of the addition of the PDA. The results are plotted in Fig. 2. Initially, the weight increases linearly with solution concentration. The rate is consistent with a prediction based on the measured precursor yield, assuming that all of the pore space within the compact is filled by the solution. Beyond a critical concentration ( ≈ 340 mg $Al_2O_3/cm^3$ of solution) corresponding to a precursor yield of about 9.5%, the weight gain diminishes rapidly, implying minimal impregnation. Based in part on these results, two solution concentrations were selected for subsequent experiments: $y_\gamma \approx 3\%$ and 8%. The latter value lies somewhat below the maximum dictated by permeability. The former value was selected to be consistent with that used in previous studies on porous matrix composites.[3,4] The number of impregnation cycles was varied from 2 to 10. As shown later, the properties were found to depend only on the total amount of PDA, independent of the specific combination of precursor concentration and number of impregnation cycles.

Previous work on composite fabrication had revealed some benefits in using a hybrid approach involving both alumina particle additions to the slurry and subsequent precursor impregnation and pyrolysis.[1,2] The alumina particles were found to improve the mechanical integrity of the green panels following the initial low-temperature heat treatment, relative to that containing pure mullite, and allowed handling during subsequent precursor impregnation without imparting damage to the panel. Furthermore, density measurements on various mullite/alumina slurries showed some evidence of densification for alumina contents exceeding 20%. With this experience, the composites had

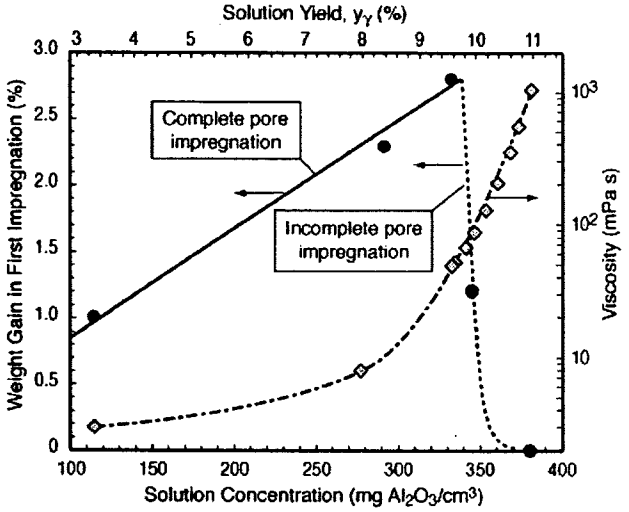


**Fig. 2.** Effects of precursor solution concentration on viscosity and, in turn, on the degree of solution impregnation into a porous matrix composite. Solid line shows the predicted trend in weight gain assuming all of the pores within the matrix are filled by the solution.

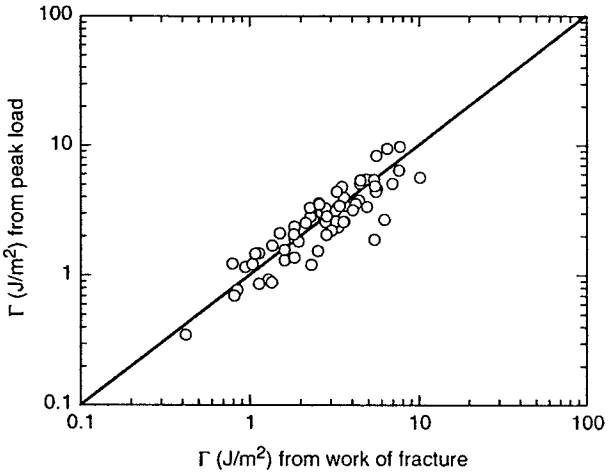


**Fig. 3.** Comparisons of toughness values determined from work of fracture and from the peak load in chevron-notched bend specimens.

been fabricated using a matrix slurry of 80% mullite and 20% alumina (80M/20A), followed by precursor impregnation and pyrolysis. Consequently, the effects of the PDA on the properties of compacts with the latter composition (80M/20A) were also assessed in the present study.

The open and closed porosities were determined from a combination of Archimedes measurements on the compacts[20] and density measurements on the constituent particles using a pycnometer. In some cases, the surface area was measured using the BET method.[21] The microstructures were probed in two ways: by scanning electron microscopy of fracture surfaces, and by energy-dispersive spectroscopy (EDS) of foils in a transmission electron microscope (TEM).

Young's modulus of each fired compact was measured using strain-gauged flexure specimens, 5 mm × 5 mm × 50 mm long, loaded in four-point bending. The inner and outer loading spans were 20 and 40 mm, respectively. Toughness was obtained from three-point bend tests on chevron-notched specimens with the same dimensions and instrumented with an LVDT to measure load-point displacement. In cases where the crack grew stably across the specimen cross-section, the toughness $\Gamma$ was calculated from the work of fracture.[22] In the few instances where fracture occurred catastrophically at the load maximum, the fracture toughness, $K_c$, was calculated from the peak load and the stress intensity solutions developed by He and Evans.[23] It was then converted to $\Gamma$ through the Irwin relation using the average measured Young's modulus from the unnotched tests. Figure 3 shows comparisons of the results from the two methods for cases in which stable growth had occurred. In the vast majority of cases, the two values are within about 30% of one another. This difference coincides closely with the variability in the modulus measurements for a given material, indicating that the two measurement techniques are consistent with one another.

## III. Physical Properties and Microstructures

The effects of precursor impregnation and pyrolysis on compact porosity are summarized in Fig. 4. Also shown for comparison is a prediction, assuming that: (i) all of the pore space is filled by the precursor solution on each impregnation cycle; (ii) during pyrolysis (900°C), the precursor solution is converted to γ-alumina; and (iii) during the final heat treatment (1200°C), the γ-alumina is converted to α-alumina. The predicted porosity is given by

$$\frac{p}{p_0} = 1 - (1 - [1 - y_\gamma]^N)\frac{\rho_\gamma}{\rho_\alpha} \qquad (2)$$

where $p_0$ is the porosity of the compact before impregnation and $N$ is the number of impregnation cycles. Upon fitting Eq. (2) to the experimental data, the volumetric yields of the two precursors are inferred to be 2.4% and 6.7%. These are about 20% lower than the values obtained from the precursor solutions alone (3% and 8%). The discrepancy may arise from one or more sources. Losses of precursor solution from the compact may occur: notably, during the period between the completion of precursor impregnation and the onset of gelation. While no significant closed porosity was detected in the final compacts, it is possible that closed porosity could have arisen during the conversion of the dried precursor to transient alumina. In that event, the net amount of open porosity susceptible to impregnation would decrease, and hence the amount of alumina that can be incorporated in each impregnation cycle. This "transient" closed porosity could be subsequently reopened by shrinkage of the precursor-derived oxide during the final conversion to corundum, and/or densified in part as the typically nanocrystalline transient alumina is heated to higher temperatures during the conversion stage.

Representative EDS maps of two prototypical microstructures are shown in Fig. 5. One is of the 80%M/20%A particle mixture (without precursor addition), and the other comprises particles of pure mullite and about 15% PDA, the latter coming from 10 impregnation cycles of the concentrated precursor. The maps are produced by separately mapping out regions containing Al and Si and then superimposing the two images in such a

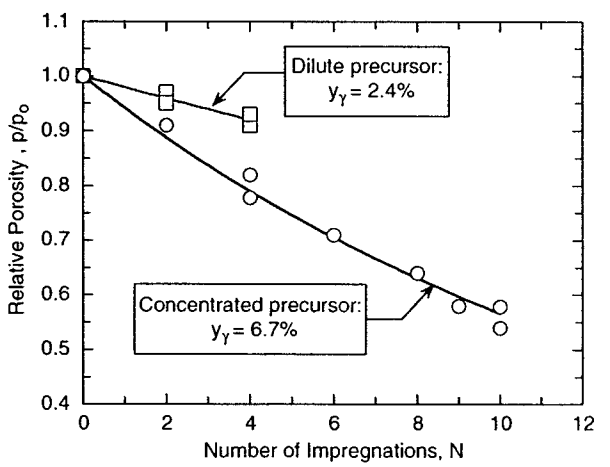


**Fig. 4.** Reduction in porosity following precursor impregnation and pyrolysis. Solid lines are fits of Eq. (2) to the experimental data.

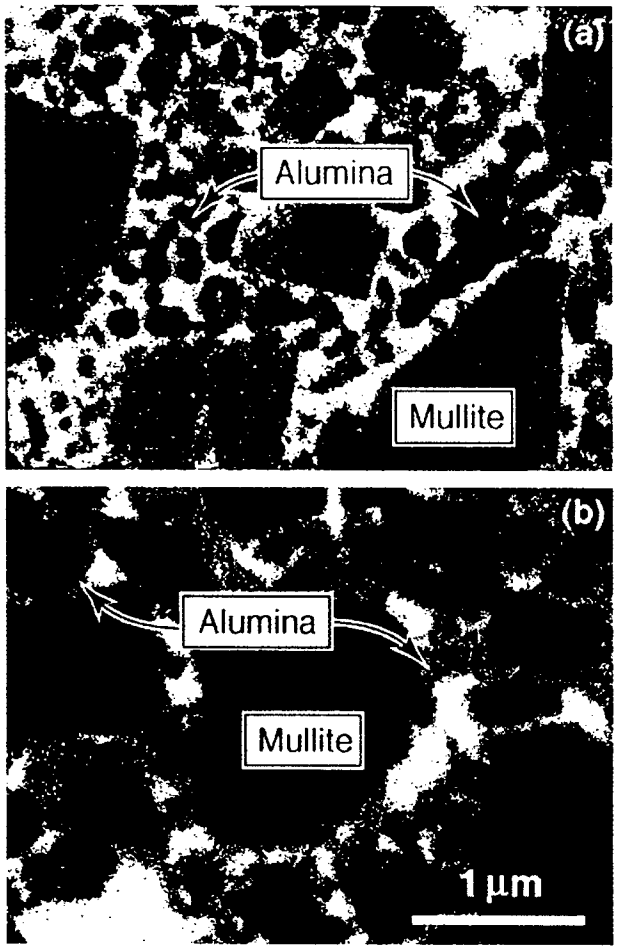


Fig. 5. Energy-dispersive spectroscopy/transmission electron microscope maps of thin foils of (a) 80% mullite/20% alumina (without precursor addition) and (b) pure mullite compact impregnated 10 times with the concentrated precursor, yielding $V_{PDA} = 15.8\%$.

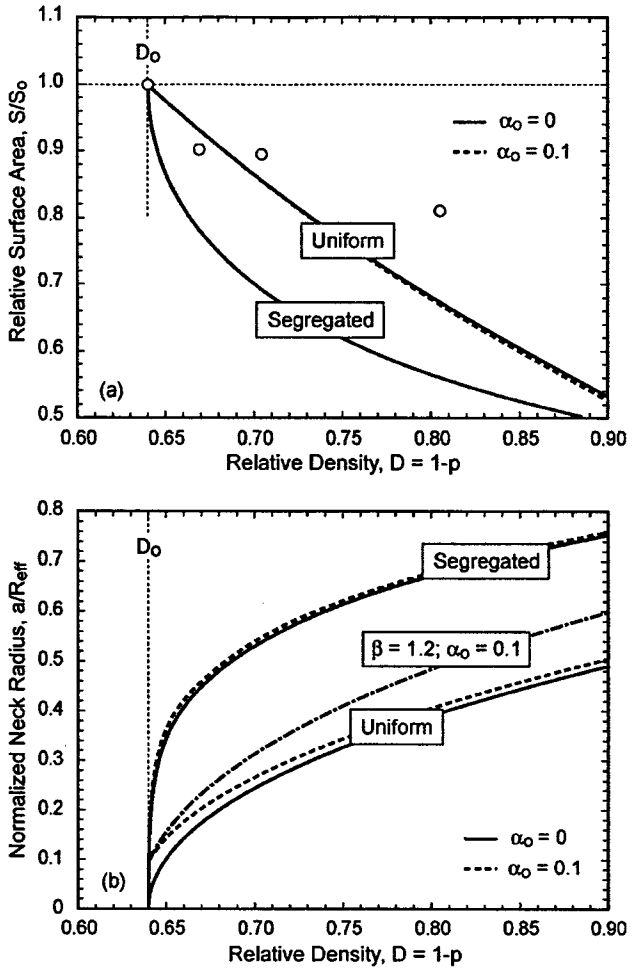


Fig. 6. Effects of precursor-derived alumina on (a) normalized specific surface area and (b) neck size. Details of the model predictions are given in the Appendix A. (Uncertainty in each measurement in (a) is less than the symbol size.)

way that alumina appears red and mullite appears blue. In the former case, the distinct nature of the two particle types and their distribution are evident; in the latter, the alumina forms a coating (albeit somewhat nonuniform) on the mullite particles, roughly consistent with the schematic shown in Fig. 1(b).

The results from a series of surface area measurements showing the effect of the PDA are plotted in Fig. 6. Here the specific surface area is normalized by the value, $S_0$, prior to precursor impregnation. The results show a reduction in specific surface area with precursor addition, but generally lower than that expected from simple geometric models based on randomly packed spherical powders. Two extreme scenarios are analyzed (Appendix A). One assumes that the precursor-derived oxide is uniformly distributed over the surfaces of the powders, building up the necks as its thickness increases (Fig. A-1(a)). The other considers the precursor to segregate completely to the inter-particle contacts, with no material added to the surface of the powders away from the necks (Fig. A-1(b)). The models allow for the presence of an initial neck size, produced during the matrix-strengthening treatment prior to the first precursor impregnation. These two scenarios, albeit idealized, provide useful bounds to the reduction of pore surface area with increasing densification, as well as to the rate of buildup of the necks between particles (Fig. 6(b)). Comparison with the experimental results in Fig. 6(a) reveals that, in the early stages of the process, the normalized area falls within these bounds and is closer to the uniform distribution model. There is, however, evidence that some amount of segregation occurs, as discussed in Section IV. The implication is that the experimental points should continue to fall within the boundaries as densification proceeds, but in reality the pore area decreases at a slower rate than that expected from either model.

Further insight into the sources of the above discrepancy can be obtained from the fracture surfaces of the broken porous compacts (Fig. 7). For moderate PDA additions, the fracture surfaces are seemingly indistinguishable from those of the particle aggregates alone; compare, for example, Fig. 7(a) and (b) with (c) and (d). This result suggests that the coating is thin and uniform, in qualitative agreement with the specific surface area measurements for low PDA loadings in Fig. 6. For larger PDA additions (Fig. 7(e) and (f)), the PDA coating breaks up into small discrete islands on the larger mullite particles. Such island formation leads to an increase in specific surface area and hence a lower rate of pore surface reduction with densification than that expected from the model predictions in Fig. 6(a).

## IV. Young's Modulus

### *(1) Experimental Measurements*

The modulus measurements are plotted in Fig. 8 as a function of the percentage of total volume occupied by the PDA: $V_{PDA} = p_0 - p$. In this context, the PDA is extremely effective. For instance, a 10% addition of PDA to a pure mullite particle aggregate leads to about a 10-fold increase in modulus. In contrast, the particulate alumina in the slurry plays only a minor role; the results for the two slurry compositions—100%M and 80%M/20%A—are similar to one another.

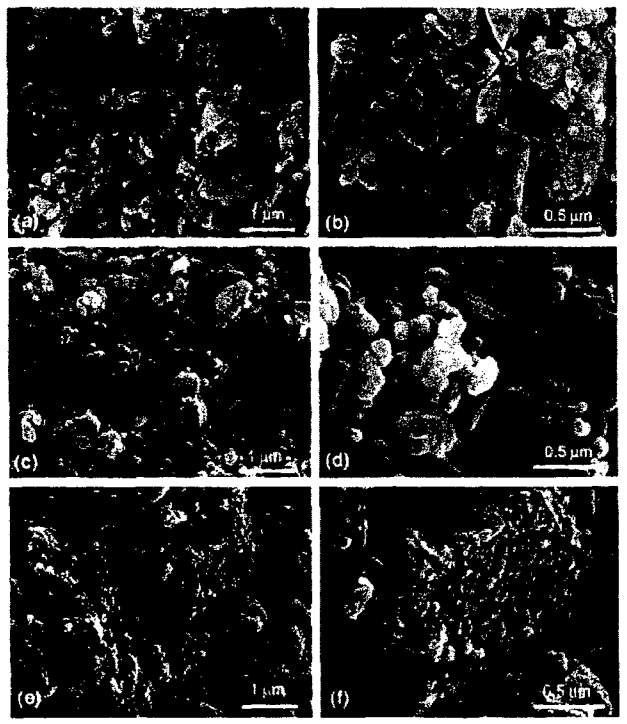


**Fig. 7.** Fracture surfaces of three representative porous compacts, all with pure mullite particle slurry, but with varying amounts of precursor-derived alumina (PDA): (a, b) $V_{PDA} = 0$; (c, d) $V_{PDA} = 8.3\%$; (e, f) $V_{PDA} = 15.8\%$. All had been aged for 2 h at 1200°C.

The effects of the aging treatment are most pronounced in the particle compacts that are free of the PDA. For instance, for $V_{PDA} = 0$, the modulus of the pure mullite compact increases by a factor of about 3 during aging, despite the absence of measurable density change.[6] The change has been attributed to sintering at the particle junctions by a (nondensifying) surface diffusion mechanism.[6] The large relative increase in modulus results from the very small junction size (and hence modulus) in the starting material such that even modest amounts of junction growth yield large increases in modulus. Similar trends are obtained in compacts of 80%M/20%A. The relative magnitude of the sintering effect becomes progressively smaller as $V_{PDA}$ increases. Indeed, for $V_{PDA} \geq 8$–10%, the effect is overshadowed by statistical variations in the measurements. This implies that the increase in modulus because of the PDA is much greater than that associated with sintering.

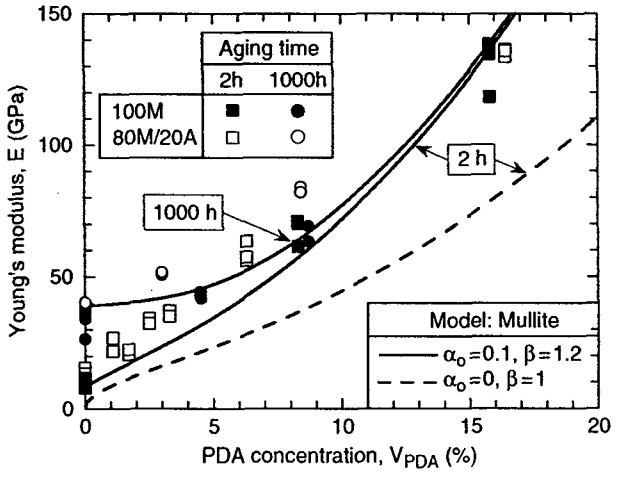


**Fig. 8.** Summary of Young's modulus measurements and model predictions. The predictions are based on the results of the discrete element simulations, shown in Fig. 9 and described in the text. Strictly, these predictions pertain only to the pure mullite slurries. Consequently, valid comparisons can only be made between the two solid lines and the two sets of filled symbols.

### *(2) Simulations and Modeling*

Effects of the PDA on the modulus of the compacts formed from 100% mullite particles have been computed using simulations based on the DEM.[13] In this method, the material is modeled as a collection of particle elements. The junction response that defines the particle element properties is derived from a finite-element analysis (FEA) of a single particle in a periodic array. The interaction between particle junctions, characterized by the displacement of one junction because of the force acting on another, is also derived from the FEA. Next, an isotropic random aggregate of touching spherical particles is generated using a computer algorithm. To ensure equilibrium, each particle is required to touch at least three neighbors upon placement onto the existing aggregate. The final particle packing density is about 55% and the average coordination number is about 6. For monophase systems, junction growth is simulated by uniformly expanding the particles and redistributing the overlapping material uniformly over the free surface of the particles. For the two-phase system comprising a contiguous particle network and a precursor-derived phase, the material is modeled as an aggregate of touching particles, all coated with a uniform layer, thickness $h$, of the second phase. This idealization is depicted in Fig. A1. The analyses described in the Appendix A show that the coating thickness can be related to the normalized junction size $\alpha$ and the volume fraction of PDA. The predicted values are plotted in Fig. 6(b) for a coordination number of 6 and two values of the initial neck size ($\alpha_0 = 0$, 0.1). To first order, the junction size is given by

$$\alpha \approx \sqrt{\frac{2V_{PDA}}{3(1-p_0)} + \alpha_0^2} \tag{3}$$

For the two-phase system, the elastic response of the junctions is calculated using a periodic array FEM model, with the two phases explicitly discretized. For both mono- and two-phase systems, the random particle network is then subjected to a prescribed macroscopically uniform strain field and the effective elastic response is determined using the DEM.[13] In the present calculations, Young's moduli $E$ and Poisson's ratios v of the two phases are taken to be $E_A = 400$ GPa, $E_M = 200$ GPa, and $\nu_A = \nu_M = 0.2$, where the subscripts A and M refer to alumina and mullite, respectively.

Figure 9 shows the results of these simulations for the two-phase system (with $\alpha_0 = 0$) as well as for monophase aggregates

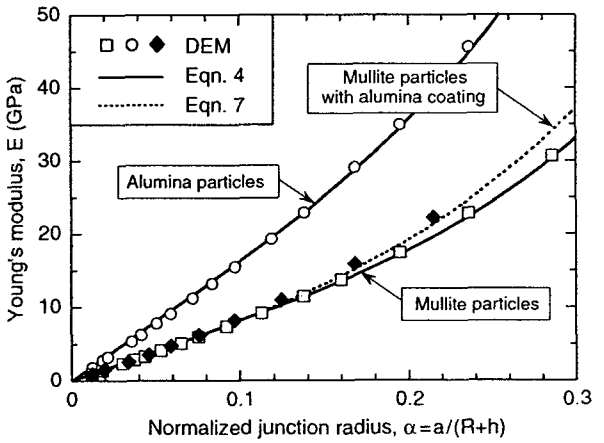


**Fig. 9.** Discrete element method (DEM) simulations of Young's modulus of monophase particle aggregates (either alumina or mullite) and mullite particle aggregates with a uniform coating of alumina.

of pure mullite and pure alumina, plotted against α. The latter results are well described by the empirical formula

$$\frac{\bar{E}}{E_s} = 0.4\alpha(1 + 14\,\alpha^3) \tag{4}$$

where $E_s$ is the modulus of the solid. Moreover, the modulus of the two-phase aggregate can be estimated by the volume fraction-weighted average of the moduli of the two monophase aggregates, evaluated at the same value of α. This estimate is obtained by replacing $E_s$ in Eq. (4) with the volume-weighted average of the moduli of the two solid phases. Upon calculating the volume ratios from geometry, the estimated modulus of the two-phase system becomes

$$\bar{E} = 0.4\alpha(1 + 14\,\alpha^3)\,[E_M \upsilon_M + E_A(1 - \upsilon_M)] \tag{5}$$

where

$$\upsilon_M = \frac{1 - p_0}{1 - p_0 + V_{PDA}} \tag{6}$$

Upon calculating $V_{PDA}$ as a function of α from Eq. (3), with $\alpha_0 = 0$, and combining Eqs. (4), (5), and (6), the estimated modulus of the two-phase system becomes

$$\bar{E} = 0.4\alpha(1 + 14\,\alpha^3)\,E_M\left[\frac{(1 - p_0) + (E_A/E_M)V_{PDA}}{(1 - p_0) + V_{PDA}}\right] \tag{7}$$

The modulus estimates for the mullite/alumina system obtained by this averaging procedure, shown by the dashed line in Fig. 9, agree well with the results of the DEM simulations.

The model results are replotted in Fig. 8, for comparison with the experimental measurements. Several features are noteworthy. Because the junctions between the mullite particles are modeled as point contacts when $\alpha_0 = 0$, the predicted modulus goes to zero when $V_{PDA} = 0$. This behavior differs from that obtained experimentally. That is, the modulus of the mullite particle aggregate is finite, at about 10 GPa: a consequence of the finite (but small) junction size. The predicted modulus subsequently increases with $V_{PDA}$, but at a rate that is significantly lower than that of the measurements. The rather large discrepancy at large values of $V_{PDA}$ (approaching 60 GPa) suggests that other sources of error must be present, apart from the neglect of the initial junction size. It is surmised that, because of capillarity, the PDA forms preferentially at the mullite particle contacts, rather than as a uniform particle coating, thereby stiffening the particle junctions and elevating the composite modulus.

The effects of both the initial junction size and the nonuniformity of the PDA can be taken into account through an approximate modification to the DEM results. For this purpose, Eq. (3) is modified to read as

$$\alpha' \approx \sqrt{\beta^2 \frac{2V_{PDA}}{3(1 - p_0)} + \alpha_0^2} \tag{8}$$

where β is a nondimensional parameter, $\geq 1$, that accounts for preferential alumina formation at the particle junctions. In this context, the normalized junction size α in both Fig. 9 and Eq. (8) is reinterpreted as α′. Combining Eqs. (7) and (8) then yields the variation in $\bar{E}$ with $V_{PDA}$. The resulting predictions for $\beta = 1.2$ and $\alpha_0 = 0.1$ are shown in Fig. 8. This combination yields a good fit to the data for the 2 h aging over the entire range of $V_{PDA}$. The corresponding buildup in neck size is compared in Fig. 6(b) with those resulting from the two extreme scenarios analyzed in the Appendix A. It is noted that the inferred level of segregation, reflected in the value of β, is modest. The neck size curve in Fig. 6(b) is closer to the uniform distribution scenario than to the full segregation model, in qualitative agreement with the specific area measurements discussed in the context of Fig. 6(a). Furthermore, although this prediction is strictly applicable to the compacts containing pure mullite particles, it appears to underestimate only slightly the results for the 80M/20A mixtures.

The effects of the extended (1000 h) aging treatment on the modulus of compacts containing the PDA are treated in the following way. In an approximate sense, the addition of PDA can be viewed as being equivalent to a sintering treatment, provided both yield the same changes in junction size without affecting interparticle spacing. This equivalence stems from the fact that the modulus is dictated by the current junction size, essentially independent of the route taken to achieve it (notwithstanding slight differences in the moduli of the two phases). In the sintering case, the junction size evolves according to a power law of the form:[6]

$$\alpha = \left(\frac{t}{t_R}\right)^{1/n} \tag{9}$$

where $t$ is the sintering time, $t_R$ is a reference time, and $n$ is a constant, the latter two depending on the transport mechanism. (For mullite, junction growth occurs by surface diffusion, whereupon $n = 7$.[6]) The junction size α′ that results from precursor addition (according to Eq. (8)) can be viewed as having been developed through a sintering treatment of the monophase particle aggregate, for an equivalent sintering time, $t_{eq}$, given by

$$t_{eq} = t_R(\alpha')^n \tag{10}$$

After additional sintering for time $t$, the final junction size is evaluated from Eq. (9), using the *total* sintering time, $t + t_{eq}$. The result is

$$\alpha = \alpha'\left[1 + \left(\frac{t}{t_R}\right)\left(\frac{1}{\alpha'}\right)^n\right]^{1/n} \tag{11}$$

The model prediction (Eqs. (7) and (11)) is plotted in Fig. 8, using a reference time $t_R = 2 \times 10^6$ h. This adequately captures the trend for the pure mullite particle aggregates with added PDA. It is of interest to note that the corresponding reference time inferred from sintering treatments of pure mullite (absent PDA) is $t_R = 8 \times 10^6$ h:[6] the fourfold difference reflecting the higher sinterability of the alumina in the PDA-containing mixtures. Indeed, it is for this reason that the present model predictions (using the lower value of $t_R$) slightly overestimate the modulus for the pure mullite ($V_{PDA} = 0$).

In light of the rather weak sensitivity of the modulus to the slurry composition (100M vs 80M/20A), no attempt was made to explicitly model a two-phase particle aggregate containing a precursor-derived phase. Models for the behavior of the two-phase aggregate alone are presented elsewhere.[6]

## V. Toughness

The toughness measurements are plotted in Fig. 10. For the as-processed materials, the toughness increases approximately linearly with $V_{PDA}$, almost independent of the slurry composition (100M vs 80M/20A). Furthermore, the toughness increases slightly following the additional 1000 h aging. These results are consistent with the associated increases in junction size because of both addition of PDA and sintering.

Also shown in Fig. 10 are the predictions of numerical simulations of fracture, again using the DEM. The results of the simulations for monophase aggregates are well described by:[6]

$$\frac{\Gamma}{\Gamma_j} = 12\alpha^2 \tag{12}$$

where $\Gamma_j$ is the intrinsic junction toughness. This result is adapted to the PDA-containing aggregates by using the junction size

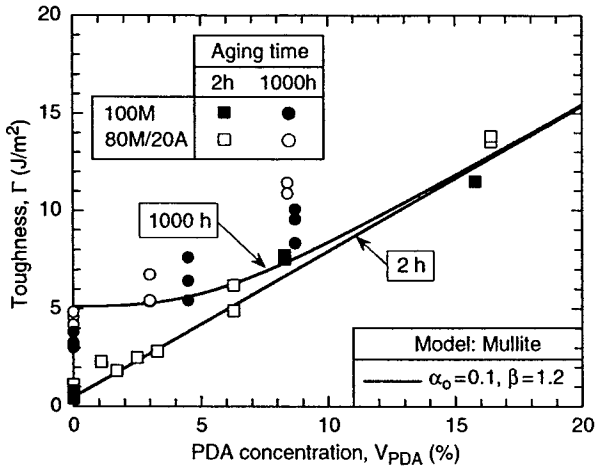


**Fig. 10.** Summary of toughness measurements and model predictions. The model predictions are based on the parameter values used to calculate Young's modulus in Fig. 8.

given in Eq. (8), whereupon the toughness becomes

$$\frac{\Gamma}{\Gamma_j} = 12\left(\beta^2 \frac{2V_{PDA}}{3(1-p_0)} + \alpha_0^2\right) \tag{13}$$

For consistency with the modulus predictions, simulations for the 2 h aging treatment were performed using $\alpha_0 = 0.1$ and $\beta = 1.2$, with $\Gamma_j$ being a fitting parameter. This procedure yields $\Gamma_j = 4$ J/m$^2$: only slightly greater than the value (3 J/m$^2$) that had been inferred previously from measurements on pure mullite.[6]

The effects of extended aging are taken into account in the same manner described above for the modulus. That is, junction growth is assumed to follow in accordance with Eq. (11), with a reference time, $t_R = 2 \times 10^6$ h. Combining this result with Eq. (12) yields the predicted curve in Fig. 10. Although the prediction yields the correct qualitative trends, the scatter in the experimental measurements precludes a more critical assessment of the model. Indeed, some discrepancy is expected, since the pertinent reference time should depend on the amounts of the two phases present at the particle junctions, as dictated by the PDA concentration.

## VI. Crack Deflection

The measured values of modulus and toughness have been used to compute the crack deflection parameter Σ (Eq. (1)), assuming that the aggregates are combined with Nextel 720 fibers to form a composite. The results are plotted against $V_{PDA}$ in Fig. 11. Here, again, the two slurry compositions yield similar results. For the as-processed materials, Σ decreases with increasing $V_{PDA}$ and eventually falls below the critical value, $\omega \approx 1$, at $V_{PDA} \approx 9\%$. This point is expected to mark the onset of crack penetration into the fibers and essentially a complete loss in damage tolerance. Extended aging causes a reduction in Σ, especially at low values of $V_{PDA}$. Furthermore, it reduces the critical value associated with crack penetration, to $V_{PDA} \approx 7$–$8\%$.

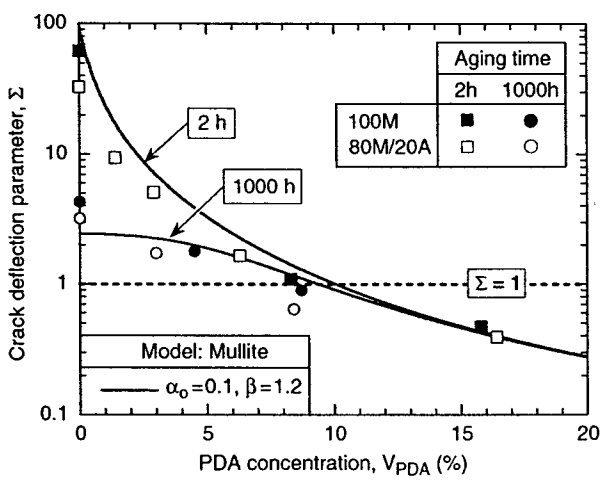


**Fig. 11.** Effects of precursor-derived alumina (PDA) concentration and aging on the crack deflection parameter, Σ, calculated using fiber properties $\Gamma_f = 15$ J/m$^2$ and $E_f = 260$ GPa.

The predicted results from the models for modulus and toughness (calibrated accordingly) are also shown in Fig. 11. A satisfactory correlation with the experimental measurements is obtained. Most notably, the predicted critical value, $V_{PDA} \approx 9$–$10\%$, is broadly in line with that inferred from the measurements.

## VII. Conclusions

The mechanical properties of mullite particle aggregates can be effectively tailored by the addition of PDA. Tenfold changes in both modulus and toughness can be obtained through the addition of moderate amounts of alumina, in the range of 10–15%. Significantly smaller changes can be effected through the use of alumina particle additions. The precursor-derived route has the additional advantage over the mixed mullite/alumina particle route in that the contiguity of the mullite particle network is not compromised. Consequently, the structure is relatively immune from densification at the targeted upper use temperature for the corresponding fiber composites.

The mechanical properties of the two-phase aggregates can be described using idealizations of the particle and precursor topology coupled with simulations based on the DEM. Comparisons between predicted and measured properties suggest that the precursor-derived phase exhibits some degree of segregation to the particle junctions, yielding larger property elevations relative to that for a uniform precursor distribution.

Limits have been established on the maximum acceptable concentration of the precursor-derived phase, such that a composite with the candidate matrix would satisfy the crack defection condition. In order to produce composites that are damage tolerant under fiber-dominated loadings yet retain adequate off-axis properties, precursor concentrations slightly below the critical value would be preferred. Experiments are in progress to assess these predictions.

## Appendix A: Models for Precursor Buildup on Particles

### *(A.1) Preliminaries*

Models representing two extreme scenarios of precursor buildup around the matrix particles are developed. The geometrical features of the models are depicted in Fig. A1. The goal is to describe the variation in specific surface area (defined as pore area per unit mass or particles) and contact area between particles as the relative density increases with the addition of precursor-derived ceramic. The particles are assumed to be initially spherical with radius $R$ and packed in a random configuration with coordination number $z$. The models include the possibility of a finite contact area of radius $a_0$, developing during the initial heat treatment, prior to precursor impregnation. In that event, the initial surface area and volume per particle are

$$A_0 = 4\pi R^2\left[1 - \frac{z}{2}\left(\frac{h_0}{R}\right)\right] \tag{A-1a}$$

$$V_0 = \frac{4}{3}\pi R^3\left[1 - \frac{z}{4}\left(\frac{h_0}{R}\right)^2\left(3 - \frac{h_0}{R}\right)\right] \tag{A-1b}$$

where $h_0$ is the height of the spherical cap that is truncated from the particle to create an initial neck of radius $a_0$ (Fig. A1).

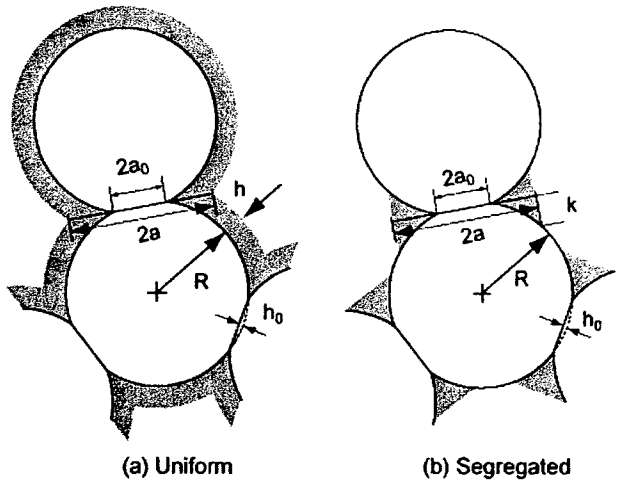


**Fig. A1.** Schematics of the two extreme scenarios in precursor topology: (a) uniform distribution on the particle surfaces, and (b) complete segregation to the particle necks.

In general, the relative (specific) surface area is given by the expression

$$\frac{S}{S_0} = \frac{A}{A_0}\left[1 + \left(\frac{\rho_A}{\rho_0}\right)\frac{\Delta V}{V_0}\right]^{-1} \tag{A-2}$$

where $\rho_0$ and $\rho_A$ are the densities of the particles and the PDA, respectively, and $A$ and $\Delta V$ are the pore area and volume of PDA added per particle, respectively. The porosity is given by

$$p = p_0 - (1 - p_0)\frac{\Delta V}{V_0} \tag{A-3}$$

where $p_0$ is the initial porosity. The normalized neck radius is defined as

$$\alpha = \frac{a}{R_{\text{eff}}} \tag{A-4}$$

where $R_{\text{eff}}$ is the current radius of the particle away from the neck area. Its initial value, before precursor impregnation, is

$$\alpha_0 = \left(\frac{2h_0}{R} - \left(\frac{h_0}{R}\right)^2\right)^{1/2} \tag{A-5}$$

### *(A.2) Uniform Distribution*

In one scenario the PDA is assumed to be distributed uniformly over the free surface of the particles as a coating with thickness $h$, except where prohibited by particle contact (see Fig. A1(a)). The analysis is based on a single representative particle and its corresponding coating and void space. The pore surface area and PDA volume per particle are given by

$$A = 4\pi R^2\left\{1 - \frac{z}{2}\left(\frac{h_0}{R}\right) + \left[2 - \frac{z}{2}\left(1 + \frac{h_0}{R}\right)\right] \times \left(\frac{h}{R}\right) + \left(1 - \frac{z}{2}\right)\left(\frac{h}{R}\right)^2\right\} \tag{A-6a}$$

$$\Delta V = \frac{4}{3}\pi R^3\left\{\left(1 + \frac{h}{R}\right)^3 - 1 - \frac{z}{4}\left[2\left(\frac{h}{R}\right)^3 + 3\left(1 + \frac{h_0}{R}\right) \times \left(\frac{h}{R}\right)^2 + 6\left(\frac{h_0}{R}\right)\left(\frac{h}{R}\right)\right]\right\} \tag{A-6b}$$

The porosity is related to the normalized thickness $h/R$ through Eqs. (A-3) and (A-6b). For this geometry $R_{\text{eff}} = R + h$ and the normalized neck radius is

$$\alpha = \left[2\left(1 + \frac{h}{R}\right)\left(\frac{h_0}{R} + \frac{h}{R}\right) - \left(\frac{h_0}{R} + \frac{h}{R}\right)^2\right]^{1/2} \times \left(1 + \frac{h}{R}\right)^{-1} \tag{A-7}$$

Combining this with Eq. (A-5) yields

$$\alpha = \left[\alpha_0^2 + \frac{2h}{R} + \left(\frac{h}{R}\right)^2\right]^{1/2}\left(1 + \frac{h}{R}\right)^{-1} \tag{A-8}$$

### *(A.3) Precursor Segregation to Necks*

In a diverging scenario, the precursor is assumed to be fully segregated to the necks. For simplicity, the PDA buildup is taken to have a cylindrical geometry as illustrated in Fig. A1(b). The half thickness at the edge of the neck is designated as $k$ and is analogous but not equivalent to the $h$ used in the earlier case. The pore surface area and PDA volume per particle are now given by

$$A = 4\pi R^2\left\{1 - \frac{z}{2}\left(\frac{h_0}{R}\right) - \frac{z}{2}\left(\frac{k}{R}\right) \times \left[1 - \sqrt{\left(\frac{h_0}{R} + \frac{k}{R}\right)\left(2 - \frac{h_0}{R} - \frac{k}{R}\right)}\right]\right\} \tag{A-9a}$$

$$\Delta V = \frac{4}{3}\pi R^3\left\{\frac{z}{4}\left(\frac{k}{R}\right)^2\left[3\left(1 - \frac{h_0}{R}\right) - 2\left(\frac{k}{R}\right)\right]\right\} \tag{A-9b}$$

As before, the porosity is related to the normalized thickness $k/R$ through Eqs. (A-3) and (A-9b). For this geometry, $R_{\text{eff}} = R$ and the normalized neck radius is

$$\alpha = \left[2\left(\frac{h_0}{R} + \frac{k}{R}\right) - \left(\frac{h_0}{R} + \frac{k}{R}\right)^2\right]^{1/2} \tag{A-10}$$

Combining with Eq. (A-5) yields

$$\alpha = \left[\alpha_0^2 + \frac{2k}{R}\sqrt{1 - \alpha_0^2} - \left(\frac{k}{R}\right)^2\right]^{1/2} \tag{A-11}$$

Comparison of the models is performed by setting a value of $p_0$ and then calculating the values of $h/R$ and $k/R$ implicitly from the combination of Eq. (A-3) and either Eq. (A-6b) or (A-9b). Once the pertinent value of the normalized thickness is known, $S/S_0$ and $\alpha$ can be readily calculated. The results of such calculations are compared with the experimental measurements in Fig. 6.

## Acknowledgments

The authors gratefully acknowledge the assistance of J. Y. Yang (UCSB) in materials processing and the Materials Research Laboratory of NGK Insulators in the TEM/EDS analysis.

## References

[1]C. G. Levi, J. Y. Yang, B. J. Dalgleish, F. W. Zok, and A. G. Evans, "Processing and Performance of an All-Oxide Ceramic Composite," *J. Am. Ceram. Soc.*, **81**, 2077–86 (1998).

[2]J. A. Heathcote, X. Y. Gong, J. Y. Yang, U. Ramamurty, and F. W. Zok, "In-Plane Mechanical Properties of an All-Oxide Ceramic Composite," *J. Am. Ceram. Soc.*, **82** [10] 2721–30 (1999).

[3]M. A. Mattoni, J. Y. Yang, C. G. Levi, and F. W. Zok, "Effects of Matrix Porosity on the Mechanical Properties of a Porous-Matrix, All-Oxide Ceramic Composite," *J. Am. Ceram. Soc.*, **84** [11] 2594–602 (2001).

[4]E. A. V. Carelli, H. Fujita, J. Y. Yang, and F. W. Zok, "Effects of Thermal Aging on the Mechanical Properties of a Porous-Matrix Ceramic Composite," *J. Am. Ceram. Soc.*, **85** [3] 595–602 (2002).

[5]C. G. Levi, F. W. Zok, J. Y. Yang, M. Mattoni, and J. P. A. Lofvander, "Microstructural Design of Stable Porous Matrices for All-Oxide Ceramic Composites," *Z. Metallk.*, **90** [12] 1037–47 (1999).

[6]H. Fujita, G. Jefferson, R. M. McMeeking, and F. W. Zok, "Mullite–Alumina Mixtures for Use as Porous Matrices in Oxide Fiber Composites," *J. Am. Ceram. Soc.*, **87** [2] 261–7 (2004).

[7]M-Y. He and J. W. Hutchinson, "Crack Deflection at an Interface Between Dissimilar Elastic Materials," *Int. J. Solids Struct. (UK)*, **25** [9] 1053–67 (1989).

[8]S. C. Nanjangud, R. Brezny, and D. J. Green, "Strength and Young's Modulus Behavior of a Partially Sintered Porous Alumin," *J. Am. Ceram. Soc.*, **78** [1] 266–8 (1995).

[9]D. Hardy and D. J. Green, "Mechanical Properties of a Partially Sintered Alumina," *J. Eur. Ceram. Soc.*, **15**, 769–75 (1995).

[10]K. Walton, "The Effective Elastic Moduli of a Random Packing of Spheres," *J. Mech. Phys. Solids*, **35** [2] 213–26 (1987).

[11]D. J. Green, C. Nader, and R. Brezny, "The Elastic Behavior of Partially-Sintered Alumina;" pp. 345–56 in *Sintering of Advanced Ceramics*, Edited by C. A. Handwerker, J. E. Blendell, and W. Kaysser. American Ceramic Society, Westerville, OH, 1990.

[12]D. J. Green, R. Brezny, and C. Nader, "The Elastic Behavior of Partially-Sintered Materials;" pp. 43–8 in *MRS Symposium Proceedings*, **Vol. 119**, Edited by D. M. Mattox, J. E. E. Baglin, R. J. Gotschall, and C. D. Batich. Materials Research Society, Pittsburgh, PA, 1988.

[13]G. Jefferson, G. K. Haritos, and R. M. McMeeking, "The Elastic Response of a Cohesive Aggregate—A Discrete Element Model with Coupled Particle Interaction," *J. Mech. Phys. Solids*, **50** [12] 2539–75 (2002).

[14]D. C. C. Lam, F. F. Lange, and A. G. Evans, "Mechanical Properties of Partially Dense Alumina Produced from Powder Compacts," *J. Am. Ceram. Soc.*, **77** [8] 2113–7 (1994).

[15]K. K. Phani and S. K. Niyogi, "Elastic Modulus–Porosity Relationship for $Si_3N_4$," *J. Mater. Sci. Lett.*, **6**, 511–5 (1987).

[16]Y. B. P. Kwan, D. J. Stephenson, and J. R. Alcock, "The Porosity Dependence of Flexural Modulus and Strength for Capsule-Free Hot Isostatically Pressed Porous Alumina," *J. Mater. Sci.*, **35**, 1205–11 (2000).

[17]A. S. Wagh, R. B. Poeppel, and J. P. Singh, "Open Pore Description of Mechanical Properties of Ceramics," *J. Mater. Sci.*, **26**, 3862–8 (1991).

[18]A. S. Wagh, J. P. Singh, and R. B. Poeppel, "Dependence of Ceramic Fracture Properties on Porosity," *J. Mater. Sci.*, **28** [13] 3589–93 (1993).

[19]F. Tancret and F. Osterstock, "Modelling the Toughness of Porous Sintered Glass Beads with Various Fracture Mechanisms," *Philos. Mag.*, **83** [1] 137–50 (2003).

[20]ASTM Standard C20-92, *Standard Test Methods for Apparent Porosity, Water Absorption, Apparent Specific Gravity, and Bulk Density of Burned Refractory Brick and Shapes by Boiling Water*. American Society for Testing and Materials, Philadelphia, PA, 1994.

[21]ASTM Standard C 1274-95, *Standard Test for Advanced Ceramic Specific Surface Area by Physical Adsorption*. American Society for Testing and Materials, Philadelphia, PA, 1995.

[22]H. G. Tattersall and G. Tappin, "The Work of Fracture and Its Measurement in Metals, Ceramics and Other Materials," *J. Mater. Sci.*, **1**, 296–301 (1966).

[23]M. Y. He and A. G. Evans, "Three-Dimensional Finite Element Analysis of Chevron-Notched, Three-Point and Four-Point Bend Specimens;" pp. 471–84 in *Fracture Mechanics: Twenty-Second Symposium*, **Vol. 1, ASTM STP 1131**, Edited by H. A. Ernst, A. Saxena, and D. L. McDowell. American Society for Testing and Materials, Philadelphia, PA, 1992. □

*Int. J. Appl. Ceram. Technol., 2 [2] 133–140 (2005)*

International Journal of
Applied Ceramic Technology
Ceramic Product Development and Commercialization

# Effects of Combustor Rig Exposure on a Porous-Matrix Oxide Composite

**Michael A. Mattoni, James Y. Yang, Carlos G. Levi, and Frank W. Zok***

*Materials Department, University of California, Santa Barbara, CA 93106-5050*

**Larry P. Zawada**

*Materials and Manufacturing Directorate, Air Force Research Laboratory, Wright-Patterson AFB, OH 45433-7817*

The present study explores the effects of exposure in a laboratory combustor on microstructural stability and property retention of an all-oxide fiber-reinforced ceramic composite. The material consists of a porous mullite–alumina matrix and Nextel 720 fibers in an eight-harness satin weave. To assess the effects of matrix strength, two matrix conditions are used, distinguished from one another by the amount of alumina added through precursor impregnation and pyrolysis (1.8% and 4.8%). In both cases, the dominant damage mode upon exposure involves interply delamination along the panel midplane. However, significant reductions in the rate and extent of cracking are obtained in the material with higher alumina content: a result of the higher delamination resistance. Mechanical tests performed on exposed specimens reveal a slight (10–20%) reduction in tensile strength along the fiber direction and a comparable increase in shear strength. These trends suggest some sintering of the matrix upon exposure. Examinations of fracture surfaces provide additional supporting evidence. Implications for long-term performance and strategies for imparting improvement in microstructural stability and delamination resistance are discussed.

## Introduction

The ever-increasing demands on propulsion systems for aircraft engines have spurred the development of continuous fiber ceramic composites (CFCCs). Materials systems based on all-oxide constituents are of particular interest for applications requiring long service lives in oxidizing environments. Although a number of these have been shown to exhibit good stability in ambient air at elevated temperatures,[1–4] their performance in the targeted service environments has yet to be critically assessed. The purpose of the current article is to present the results of an experimental investigation of the stability of one particular oxide CFCC upon exposure in a combustion environment.

The material of interest is a porous-matrix composite without a fiber coating.[5–8] It has been shown to exhibit excellent damage tolerance provided the modulus and the toughness of the matrix are not excessively high.[9,10] Otherwise, cracks formed within the matrix

Funding provided by the Air Force Office of Scientific Research under contract number F49620-02-1-0128, monitored by Dr. B. L. Lee.
*zok@engineering.ucsb.edu

penetrate into the fibers without deflection at the intervening interface. The main matrix constituent is mullite, chosen for its resistance to sintering at the upper use temperature of the fibers (about 1200°C). The minor constituent is alumina, present both in the form of fine particulates as well as through pyrolysis of a precursor liquid. The composite has demonstrated good retention in mechanical properties following long (1000 h) exposures at elevated temperatures (to 1200°C) in ambient air.

In the current study, annular test specimens of the composite are exposed in a laboratory-scale trapped-vortex combustor rig under conditions that simulate the pertinent heat loads and combustion environments.[11–14] Specifically, the combustor is operated using liquid JP-8+100 jet fuel and the peak material temperature is slightly above 1200°C. Coupled with complementary mechanical tests and microstructural examinations, such tests yield insights into degradation and damage mechanisms associated with the exposure, and thus provide guidance for future research activities in composite development.

## Materials

The reinforcements were 1500-denier Nextel 720 fiber tows, woven into an eight-harness satin-weave cloth. Each composite panel consisted of nine fiber layers and a porous matrix of ninemullite and alumina. The average fiber volume fraction was 38% and the panel thickness was 2.6 mm. A typical cross-section through one such panel is shown in Fig. 1.

The processing route was essentially identical to that described in earlier articles.[5,8] Briefly, the matrix was introduced in two steps: (i) vacuum infiltration of a slurry containing 80% of 1 μm mullite and 20% of 0.2 μm alumina particles into the fiber perform, and (ii) impregnation and pyrolysis of an alumina precursor solution ($Al_2Cl(OH)_5$). The latter impregnation and pyrolysis process was performed twice. Two precursor solution concentrations were used, as described below. To prevent segregation during drying, the panels were gelled by placing them in a chamber containing gaseous $NH_4OH$ for 6 h immediately following solution impregnation. After drying, the panels were fired at 900°C for 2 h. Following completion of both impregnation cycles, the panels were given a final heat treatment at 1200°C for 2 h.

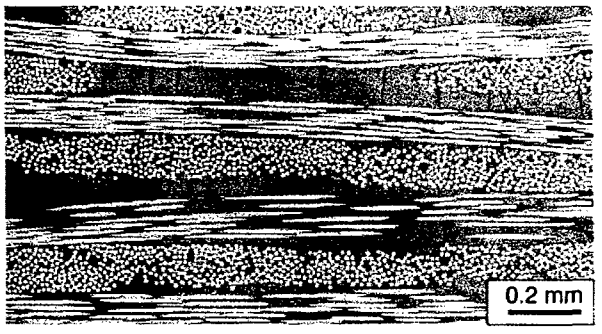


*Fig. 1. Scanning electron micrograph of polished cross-section of pristine (unexposed) composite (4.8% PDA).*

Selection of the precursor solution concentration was based in part on the results of concurrent studies, focused on the effects of the volume fraction of precursor-derived alumina, $V_{PDA}$, on both the matrix properties, and the strength and notch sensitivity of the corresponding composites.[15] The results indicate that the conditions for the deflection of matrix cracks at the fiber–matrix interface are satisfied when $V_{PDA} < 9\%$.[10] At higher concentrations, matrix cracks penetrate into the fibers, resulting in complete loss in damage tolerance. This sets limits on the allowable range of $V_{PDA}$. Moreover, within the deflection domain ($0\% < V_{PDA} < 9\%$), the in-plane notched strength decreases with increasing $V_{PDA}$: a consequence of reduced fiber pullout and reduced fracture energy.[15] In contrast, the delamination resistance increases with $V_{PDA}$.[7] Because of these divergent trends, the optimal precursor concentration is somewhat ill-defined. Consequently, in the present study, two different panels were fabricated and tested, distinguished from one another by the precursor solution concentration. Following two impregnation and pyrolysis cycles, the two solutions yielded PDA concentrations of 1.8% and 4.8%. Although both values fall within the crack deflection domain, the panel with higher PDA concentration is expected to exhibit superior delamination resistance and inferior in-plane damage tolerance, and vice versa.

## Exposure and Testing Methods

Composite specimens were exposed in a laboratory-scale ultra-compact combustor rig, shown in Fig. 2. The rig has been designed to emulate an inter-stage turbine burner. Such burners are being targeted for use in future

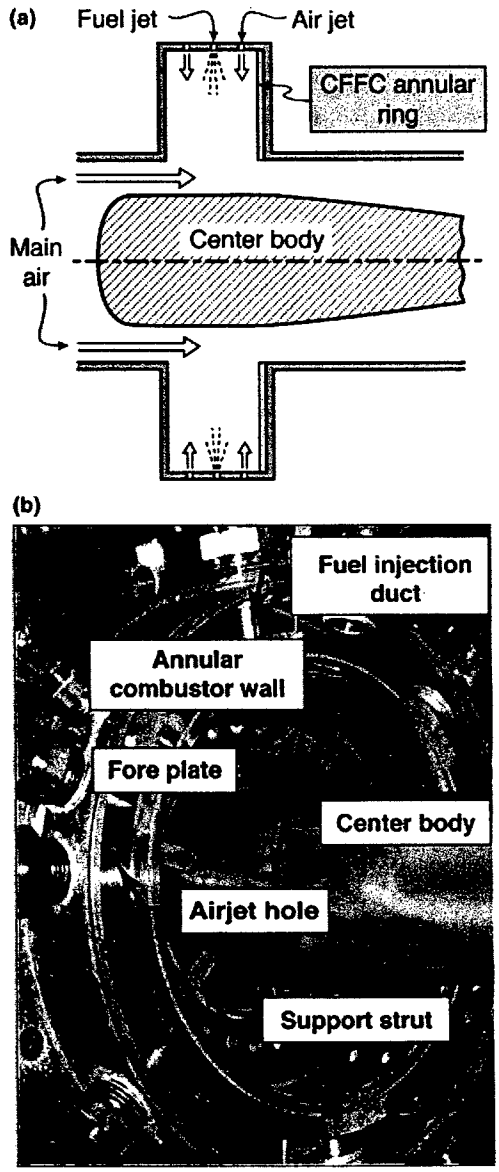


*Fig. 2. (a) Schematic of longitudinal cross-section of ultra-compact combustor rig. (b) The combustor rig, disassembled to reveal the internal parts of the combustion chamber. (For scale, the inner radius of the combustor cavity is 59 mm.)*

propulsion systems, for the purpose of improving specific thrust. The rig has also been used as a test-bed for assessment of new materials for gas turbine engines, notably ceramic composites. Its design, operation, and performance are described in detail elsewhere.[11–14] Briefly, the rig consists of an annular combustor cavity with six fuel and 24 air injection ducts, equally spaced around the circumference. The ducts drive a high-g swirling flow within the cavity. Here, the fuel mixture is partially burned before being transported to the axial main air zone. The mixture is subsequently diluted and the reaction continues to completion. Test specimens for exposure in the rig are in the form of flat annular rings, 121 mm outer diameter and 83 mm inner diameter. When inserted into the rig, they cover the entire aft face of the combustion cavity. Attachment is accomplished via a window-frame assembly. The test specimens from the two composite panels, with $V_{PDA}$ = 1.8% and 4.8%, are henceforth referred to as ring #1 and #2, respectively.

Prior to insertion into the rig, the test specimens were coated with a temperature-sensitive paint (MC 490-10, Thermographic Measurements Co. Ltd., Flintshire, UK) The paint was sprayed on and subjected to a pre-treatment of 30 min at 250°C to remove the solvent. The paint undergoes ten color changes between 490°C and 1250°C. For calibration, a series of small coated test specimens had been subjected to prescribed temperatures. Based on this calibration and the paint colors following exposure, the peak surface temperature in the combustor rig was estimated to be 1200–1225°C in localized hot spots around each fuel nozzle. These results are in close agreement with the predictions by Katta *et al.*[16]

The rig was typically operated uninterrupted for periods of 1–2 h, using liquid JP-8+100 jet fuel with essentially constant airflow rate. To evaluate combustor performance, a variety of test conditions were employed, including rich burn, lean burn, and flame blow-out. Periodically, the test specimens were extracted from the combustor rig and examined in an optical microscope. These examinations were used to guide decisions regarding further combustor rig exposure. For instance, in the case of ring #1, numerous delamination cracks were found emanating from the inner ring surface following 20 h of exposure. Consequently, the exposure experiments were discontinued and the ring then sectioned for microstructural examination. In contrast, ring #2 exhibited minimal delamination following a similar exposure and hence the rig exposure test was continued. After a considerably longer exposure time, small delamination cracks were found, including on the inner ring surface. The exposure test on this ring was terminated after 86 h.

Following exposure, the rings were examined in an optical microscope to identify the dominant damage

modes. Additionally, measurements were made of the matrix porosity (via the Archimedes method[17]) to assess potential changes associated with sintering. Finally, measurements of plate thickness, coupled with scanning electron microscope (SEM) examinations of near-surface regions of polished cross-sections, were used to determine whether any material had been volatized as a consequence of the interaction with the combustion environment.

To further assess the effects of combustor rig exposure, mechanical tests were performed to characterize both composite and matrix properties. This part of the study was restricted to the composite used to make ring #2, i.e., the one with the higher PDA concentration, because of the extensive delamination in the other ring. Comparisons were made with the corresponding properties of the pristine (as-processed) material.

The composite strength was measured using straight tensile bars cut from the rings, in the manner illustrated in Fig. 3. Each had a width of 10 mm, a gauge length of 35 mm, and was oriented with one of the fiber directions aligned with the loading axis. Longitudinal strains were measured through a strain gauge. The fracture surfaces were subsequently examined in an SEM. The shear strength was measured using Iosipescu tests, including in the 0°/90° orientation (Fig. 3). Strains were measured using gauges at +45°/−45°.

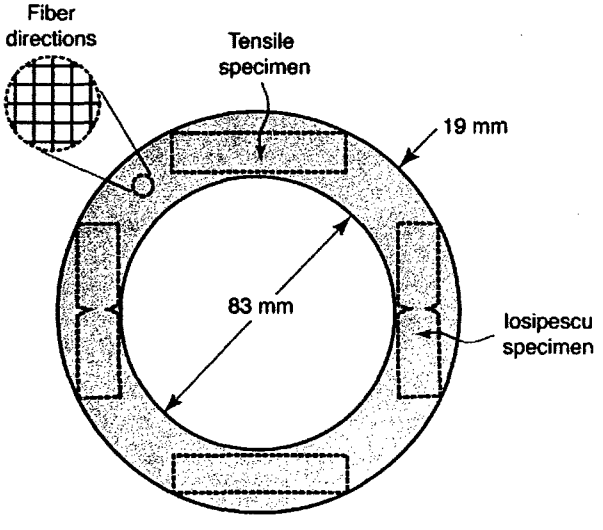


*Fig. 3. Schematic of the ring specimens used for combustor rig exposure and the locations from which the mechanical test specimens were machined.*

The matrix strength was characterized through Vickers hardness measurements. For this purpose, small specimens were machined from the panels (both pristine and exposed) and subsequently polished to a 0.1 μm finish. To facilitate polishing, the specimens were first impregnated with a low viscosity epoxy. This epoxy was burned out after polishing by heating the specimens slowly, at 5°C/min, to 550°C, holding at the temperature for 2 h, and cooling slowly to room temperature. Vickers indentations were made in two location types: (i) within matrix-rich regions between fiber cloths, and (ii) at the centers of "end-on" tows. In both cases, the indent size was restricted to one-half of the pertinent available space, i.e., either the width of the matrix region or the width of the fiber tow. This was accomplished by selecting the indentation load accordingly. Specifically, the loads were 200 and 500 g for the matrix-rich regions and the fiber tows, respectively.

The same polishing procedure was used to prepare specimens for examination of damage mechanisms. The latter were performed in an SEM.

## Measurements and Observations

The only visible microstructural damage following combustor rig exposure was in the form of delamination cracks, most emanating from the inner ring surface (Figs. 4–6); there was no evidence of fiber damage. The cracks were readily observed with the unaided eye in

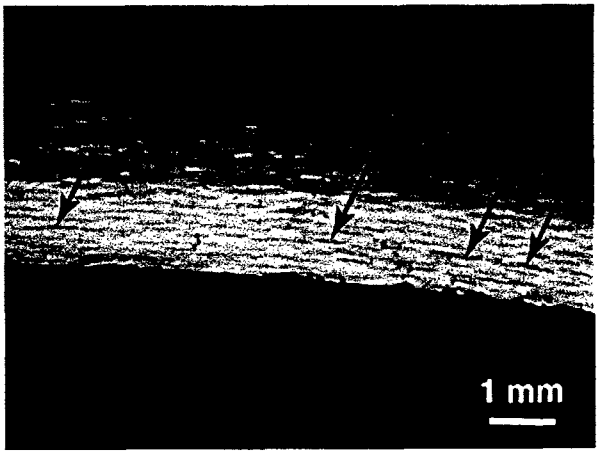


*Fig. 4. Macrophotograph of the inner surface of ring #2 following 86 h of rig exposure. Arrows highlight short segments of delamination cracks along the panel midplane.*

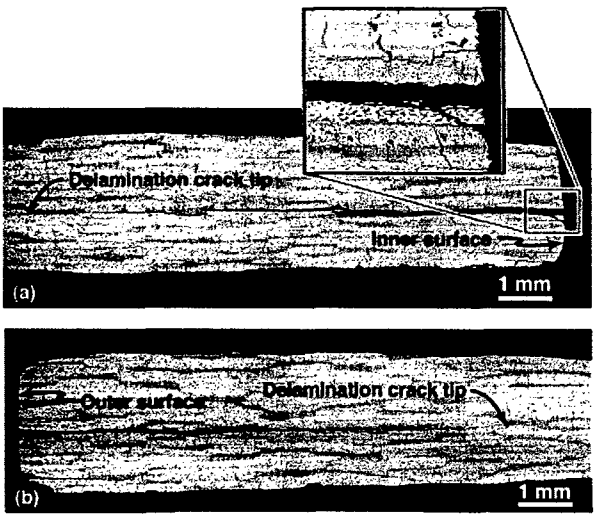


*Fig. 5. Typical delamination cracks in ring #1 ($V_{PDA}$ = 1.8%, 20 h exposure), at (a) inner and (b) outer surfaces. Inset in (a) shows the crack following an interply path as well as the extent of crack opening ( ≈ 100 μm).*

ring #1. In contrast, despite the longer exposure time, the delamination cracks in ring #2 were considerably smaller and only seen upon inspection in an optical microscope (Fig. 4). Micrographs of cross-sections also revealed periodic transverse matrix cracks (Figs. 5 and 6): a consequence of drying during processing. This type of cracking was also seen in the pristine material (Fig. 1).

The extent of delamination was significantly different in the two test specimens. For ring #1, the cracks penetrated to a depth of about 10 mm, with crack opening displacements at the inner ring surface exceeding 100 μm. In contrast, for ring #2, the cracks typically penetrated only about 1–2 mm, with correspondingly lower crack opening displacements (typically about 30 μm). This difference is attributable to the increase in matrix strength resulting from the additional PDA content in ring #2 and its effect on delamination resistance. This assertion is supported by the matrix hardness values: $30 \pm 8$ and $101 \pm 17$ kg/mm$^2$ for rings #1 and #2, respectively. Similar increases in hardness and corresponding increases in toughness have been found in neat matrix specimens of the same compositions.


*Fig. 6. Delamination in ring #2 ($V_{PDA}$ = 4.8%, 86 h exposure). In contrast to ring #1, the extent of cracking is diminished, as characterized by crack length and opening displacement.*

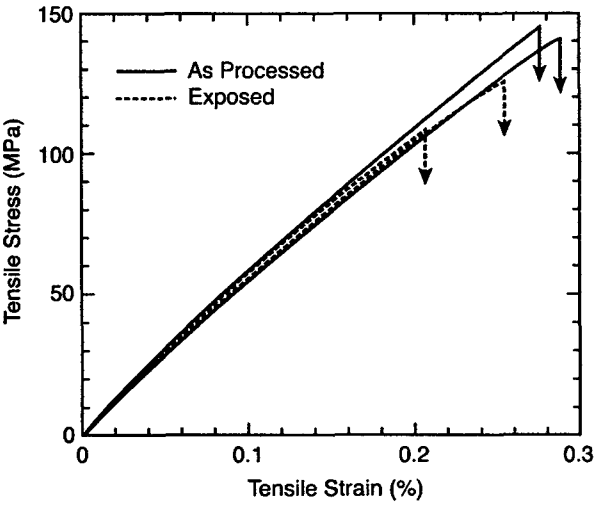


*Fig. 7. Tensile response of pristine and exposed materials.*

The in-plane tensile strength of ring #2 decreased slightly following exposure, by about 10–20% (Fig. 7). This reduction can be rationalized on the basis of observations of the fracture surfaces (Fig. 8). That is, the extent of fiber pullout within individual tows was noticeably greater in the pristine material than that in the exposed material. This indicates an increase in the strength of the fiber-matrix bond through sintering. Such sintering is also suggested by the porosity measurements. Specifically, the matrix porosity diminished slightly upon exposure, by about 1%, from $34.0 \pm 0.2\%$ to $33.0 \pm 0.2\%$. Similar trends in both strength and fiber pullout have been reported for a comparable oxide CFCC after exposure at 1200°C in air.

Increases in the strengths of both the interface bond and the matrix are also inferred from the shear tests (Fig. 9). That is, the shear strength increased slightly, by about 15%, upon exposure. Nevertheless, the large inelastic straining capability ( $\geq$ 4%) was retained.

The hardness measurements pertinent to ring #2 are summarized in Fig. 10. The values for both the matrix-rich regions and the fiber tows are uniform across the plate thickness. More importantly, the average values appear unchanged following exposure. But, since the coefficients of variation on each measurement popula-

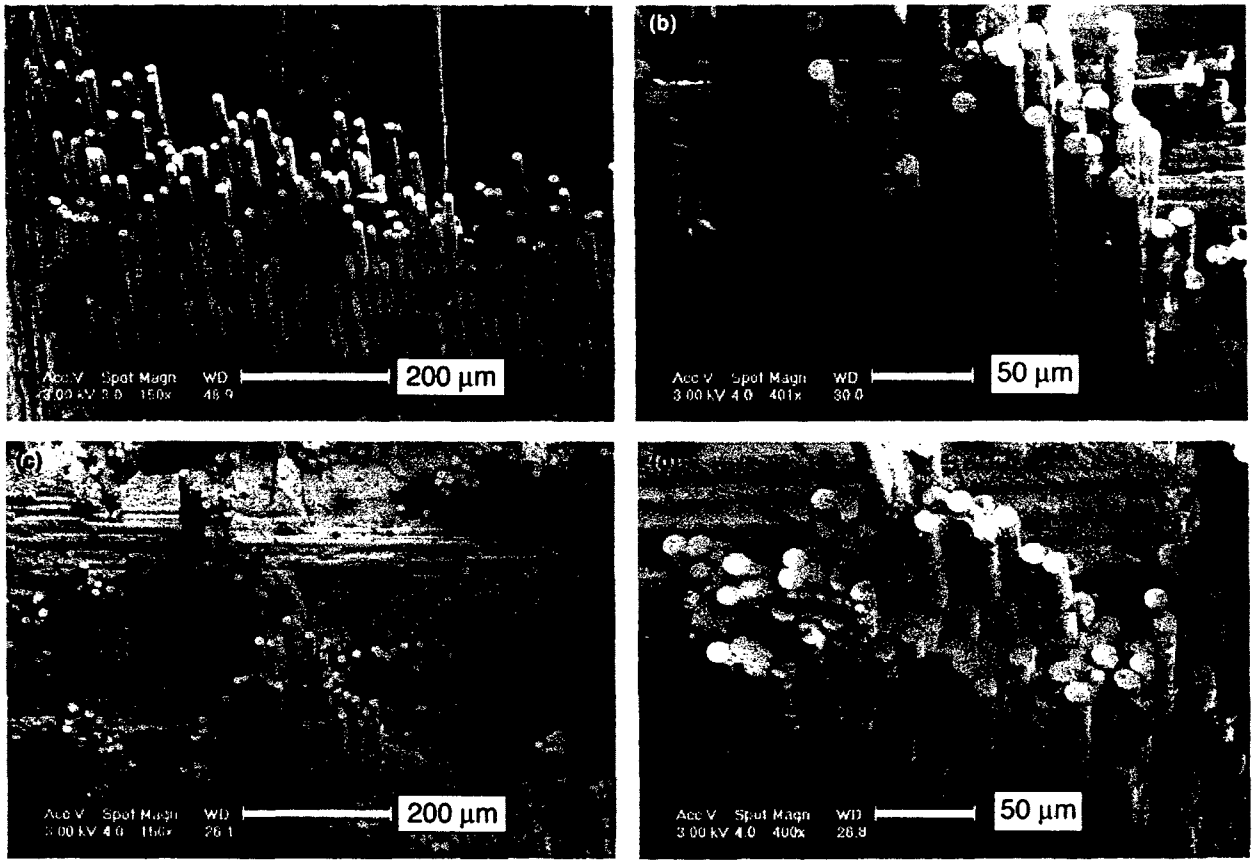


*Fig. 8. Fracture surfaces of (a, b) pristine (as-processed) material and (c, d) after exposure in the combustor (ring #2).*

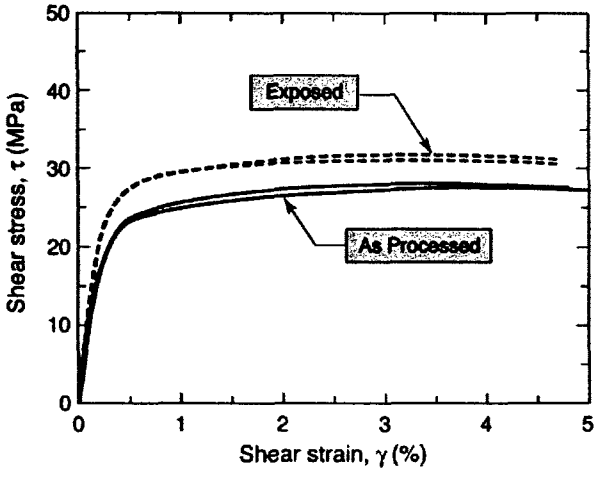


*Fig. 9. Shear response of pristine and exposed materials.*

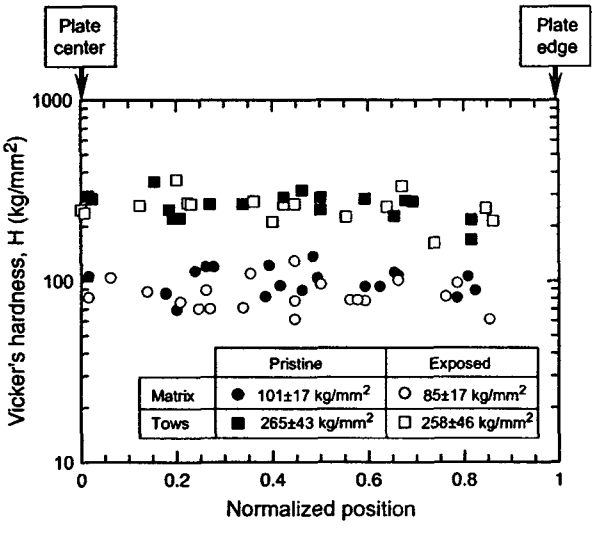


*Fig. 10. Variation in hardness across plate thickness. Inset summarizes average values and standard deviations.*

tion are about 20%, relative changes in hardness of less than this value cannot be ascertained. The inference is that changes in both matrix and interface strength are small: probably less than 20%. Indeed, the shear measurements suggest a change of only about 15%, (assuming that the composite shear strength is proportional to the matrix hardness). It should be noted that such changes are essentially negligible in relation to the three-fold change in hardness associated with the increase in precursor-derived alumina concentration over the narrow range of 1.8–4.8%.

## Discussion and Concluding Remarks

Some insights into the mechanisms of matrix sintering, especially within the fiber tows, have been obtained from independent examinations of the matrix microstructure both in the as-processed condition and after exposure at high temperature in air.[18] Three observations are particularly notable. First, in the mullite/alumina matrix systems used here, sintering of matrix particles appears to be restricted to the narrow matrix regions within fiber tows. In contrast, the larger matrix regions between tows appear to be largely unaffected, even after 1000 h at 1200°C. Second, the regions within tows show higher Al2O3/SiO2 ratios than the bulk matrix (based on energy-dispersive spectroscopy in a transmission electron microscope). This suggests a higher concentration of the more-sinterable alumina particles within the tows relative to that in the bulk. Third, the regions within the tows tend to be denuded of the larger particles, which are exclusively mullite. This observation provides additional evidence for elevated alumina levels. A working hypothesis, consistent with these observations, is that particle segregation occurs during slurry infiltration. Segregation is believed to arise from two phenomena. The first one is the physical exclusion of the larger mullite particles ($\sim 1\,\mu m$) from the narrow spaces between fibers in a tow, resulting in a higher concentration of the smaller ($\sim 0.2\,\mu m$) alumina particles. The second is the "wall effect," which constrains the packing efficiency of larger particles around fiber surfaces and creates excess void space that is preferentially filled by the finer alumina particles.[19] In combination, these phenomena should lead to increased sintering within the tows and at the interfaces with the fibers, consistent with the measurements and observations presented here.

Two strategies for improving the stability of the matrix microstructure against such sintering are envisaged: (i) To prevent segregation, the sizes of the two particle types should be more closely matched. This could be accomplished by grinding the mullite particles used in the present composites. However, this size matching has undesirable consequences in the efficiency of particle packing. (ii) The alumina particles within the matrix could be eliminated altogether, leaving just the mullite. Bonding of the particles would then be effected solely by the precursor-derived alumina. Alumina in the latter form is not subject to this type of segregation and should, in principle, yield a more uniform microstructure. Composites of this type have been successfully fabricated, although an assessment of their performance and examinations of their microstructure have yet to be performed.

The presence of delamination cracks in the exposed rings highlights the long-known problem of low transverse toughness of ceramic composites with 2D fiber architectures. The problem is exacerbated in the porous systems relative to those with fully dense matrices. Significant improvements in delamination resistance of such systems can only be achieved through the use of through thickness reinforcements, introduced, for example, by stitching 2D fiber architectures, or by using 3D weaves.

Notwithstanding the deficiencies, the present composite system has performed well in relation to other porous oxide composites, especially those with aluminosilicate matrices. In the latter systems, combustor rig tests of the type performed here have led to the development of macroscopic transverse cracks in which the fibers are broken, even after only a few hours of exposure.[20] This suggests rapid sintering of the matrix and an attendant loss in in-plane damage tolerance. For reasons not yet understood, this sintering appears to be accelerated in the presence of water vapor, such as that in the combustion environment. This presents new challenges in the design and synthesis of materials systems that retain their damage tolerance characteristics over extended service periods.

## References

1. L. P. Zawada, R. S. Hay, S. S. Lee, and J. Staehler, "Characterization and High-Temperature Mechanical Behavior of an Oxide/Oxide Composite," *J. Am. Ceram. Soc.*, 86 [6] 981–990 (2003).
2. S. G. Steel, L. P. Zawada, and S. Mall, "Fatigue Behavior of a Nextel 720/Alumina Composite at Room and Elevated Temperature," *Ceram. Eng. Sci. Proc.*, 22 [3] 695–702 (2001).

3. E. A. V. Carelli, H. Fujita, J. Y. Yang, and F. W. Zok, "Effects of Thermal Aging on the Mechanical Properties of a Porous-Matrix Ceramic Composite," *J. Am. Ceram. Soc.*, 85 [3] 595–602 (2002).
4. J. B. Davis, D. B. Marshall, and P. E. D. Morgan, "Oxide Composites of $Al_2O_3$ and $LaPO_4$," *J. Eur. Ceram. Soc.*, 19 [13–14] 2421–2426 (1999).
5. C. G. Levi, J. Y. Yang, B. J. Dalgleish, F. W. Zok, and A. G. Evans, "Processing and Performance of an All-Oxide Ceramic Composite," *J. Am. Ceram. Soc.*, 81 [8] 2077–2086 (1998).
6. J. A. Heathcote, X.-Y. Gong, J. Yang, U. Ramamurty, and F. W. Zok, "In-Plane Mechanical Properties of an All-Oxide Ceramic Composite," *J. Am. Ceram. Soc.*, 82 [10] 2721–2730 (1999).
7. M. Mattoni, J. Y. Yang, C. G. Levi, and F. W. Zok, "Effects of Matrix Porosity on the Mechanical Properties of a Porous-Matrix, All-Oxide Ceramic Composite," *J. Am. Ceram. Soc.*, 84 [11] 2594–2602 (2001).
8. C. G. Levi, F. W. Zok, J.-Y. Yang, M. Mattoni, and J. P. A. Lofvander, "Microstructural Design of Stable Porous Matrices for All-Oxide Ceramic Composites," *Z. Metallkd.*, 90 [12] 1037–1047 (1999).
9. H. Fujita, G. Jefferson, R. M. McMeeking, and F. W. Zok, "Mullite–Alumina Mixtures for Use as Porous Matrices in Oxide Fiber Composites," *J. Am. Ceram. Soc.*, 87 [2] 261–267 (2004).
10. H. Fujita, G. Jefferson, C. G. Levi, and F. W. Zok, "Controlling Mechanical Properties of Porous Mullite/Alumina Mixtures Via Precursor-Derived Alumina," *J. Am. Ceram. Soc.*, in press.
11. J. Zelina, J. Ehret, R. D. Hancock, D. T. Shouse, W. M. Roquemore, and G. J. Sturgess, "Ultra-Compact Combustion Technology Using High Swirl for Enhanced Burning Rate," *38th AIAA/ASME/SAE/ASEE Joint Conference Proceedings*, Indianapolis, IN, AIAA 2002-3725, July 2002.
12. J. Zelina, G. J. Sturgess, A. Mansour, and R. D. Hancock, "Fuel Injection Design for Ultra-Compact Combustor," *Sixteenth International Symposium on Air Breathing Engines, International Society for Air Breathing Engines*, Cleveland, OH, ISABE 2003-1089, August 2003.
13. J. Zelina, D. T. Shouse, and R. D. Hancock, "Ultra-Compact Combustors for Advanced Gas Turbine Engines," *ASME Turbo Expo 2004*, Vienna, Austria, ASME IGTI 2004-GT-53155, June 2004.
14. J. Zelina, G. J. Sturgess, and D. T. Shouse, "The Behavior of an Ultra-Compact Combustor (UCC) Based on Centrifugally-Enhanced Turbulent Burning Rates," *40th AIAA/ASME/SAE/ASEE Joint Conference Proceedings*, Ft. Lauderdale, FL, AIAA 2004-3541, July 2004.
15. M. A. Mattoni, and F. W. Zok, "Strength and Notch Sensitivty of Porous-Matrix Oxide Composites," *J. Am. Ceram. Soc.*, in press.
16. V. R. Katta, R. Anthenien, R. Mantz, W. M. Roquemore, R. A. Brockman, R. John, L. P. Zawada, T. A. Parthasarathy, and R. Kerans, "Influence of Ceramic-Matrix-Composite Wall Plates on Combustor Performance," *36th AIAA/ASME/SAE/ASEE Joint Conference Proceedings*, AIAA 2000-3351 1–10 (2000).
17. ASTM Standard C 20, *Standard Test Methods for Apparent Porosity, Water Absorption, Apparent Specific Gravity, and Bulk Density of Burned Refractory Brick and Shapes by Boiling Water*. American Society for Testing and Materials, Philadelphia, PA, 2002.
18. J. Lofvander, J. Y. Yang, F. W. Zok, and C. G. Levi, to be published.
19. F. Zok, F. F. Lange, and J. R. Porter, "The Packing Density of Composite Powder Mixtures," *J. Am. Ceram. Soc.*, 74 1880–1885 (1991).
20. T. A. Parthasarathy, L. P. Zawada, R. John, M. K. Cinibulk, R. J. Kerans, and J. Zelina, "Evaluation of Oxide–Oxide composites in a Novel Combustor Wall Application," *Int. J. Appl. Ceram. Technol.*, 2 [2] 122–131 (2005).

journal

J. Am. Ceram. Soc., 88 [6] 1504–1513 (2005)
DOI: 10.1111/j.1551-2916.2005.00299.x

# Strength and Notch Sensitivity of Porous-Matrix Oxide Composites

Michael A. Mattoni and Frank W. Zok†

Materials Department, University of California, Santa Barbara, California 93106-5050

**The effects of matrix strength on the notched and unnotched tensile properties of a family of porous-matrix oxide composites are examined both experimentally and theoretically. Experiments are performed on three composites, distinguished from one another by the amount of binding alumina within the matrix. Increases in alumina concentration produce elevations in unnotched tensile and shear strengths, but the benefits are offset by an increase in notch sensitivity. The degree of notch sensitivity is rationalized on the basis of a model that accounts for interactions between notch tip tensile and shear bands. The model predictions are cast in terms of the ratio of the notch length to a characteristic bridging length scale. These results, in turn, form the basis for a simple analytical formula for notched strength, accounting for effects of elastic anisotropy and finite sample size. The utility of this formula in predicting notched strength is assessed. Issues associated with bridging law shapes and bridging length scales are addressed. The effect of alumina concentration on notch sensitivity is discussed in terms of its influence on the bridging length scale, dictated by the interplay between the unnotched tensile strength, the longitudinal Young's modulus, the degree of in-plane elastic anisotropy, and the fracture energy. The net result is a decreasing bridging length scale and hence increasing notch sensitivity as the matrix is strengthened with alumina.**

## I. Introduction

FIBER-REINFORCED oxide composites are being targeted for use in future gas turbine engines. Their obvious advantage over monolithic ceramics is their superior damage tolerance and low notch sensitivity. Notwithstanding progress in the development of fiber coatings and environmental barrier coatings for use with SiC/SiC composites, oxide systems remain top contenders for applications requiring long service lives ($>10^4$ h) in oxidizing environments, albeit at operating temperatures (about 1200°C) that are some 100–200 K below the targeted levels for SiC/SiC. This has motivated numerous activities in material development and assessment in industrial[1–5] and government laboratories,[6–12] as well as academia.[13–19]

The present article focuses on tensile strength and notch sensitivity of one particular class of oxide composite: that in which damage tolerance is enabled by a porous matrix, rather than through the conventional route involving fiber coatings. It builds on recent experience in composite fabrication and microstructural control, through appropriate selection of matrix constituents and their topologies.[15,20] The emphasis on notch sensitivity stems from the targeted applications where holes and other stress concentrators are expected to be present, for cooling or attachment.

In notched laminates with 2D fiber architectures in a 0°/90° orientation, failure occurs through two concurrent damage processes (Fig. 1). The first involves shear deformation ahead of the notch, along bands aligned *parallel* to the loading direction.[12,16,21] This deformation occurs as a result of the shear stress acting parallel to the fiber axes coupled with the inherent anisotropy in the inelastic straining characteristics of 2D laminates. The second involves a tensile process zone, oriented *perpendicular* to the applied stress. Here, the dominant damage mechanisms are matrix cracking, interfacial debonding and sliding, and fiber fracture and pull out. These ultimately lead to the formation and propagation of a macroscopic crack. The interplay between the shear bands and the tensile process zone dictates the degree of notch sensitivity. That is, the shear deformation reduces the crack tip stresses, thereby increasing the applied stress needed for fiber fracture and composite rupture.

The subsequent study is predicated on the notion that the state of the matrix should influence the notched properties in two ways. (i) For uncoated fiber systems, the key interface properties (the debond toughness and the sliding resistance) are expected to move in tandem with the matrix mechanical properties: increasing with decreasing porosity. In the domain of global load sharing, wherein debonding and sliding occur readily at the fiber–matrix interface, elevations in interface properties increase the fiber bundle strength.[22] At the other extreme, where the interface is strong and hence strongly local-load sharing conditions are obtained, the bundle strength diminishes with increasing matrix strength and becomes inherently stochastic.[23] This implies an optimum matrix condition at which the *unnotched* composite strength achieves its maximum value. (ii) Elevations in matrix strength increase the shear strength of the composite and hence reduce the spatial extent of the shear bands in the notch tip region. As a result, the notched strength is reduced relative to the unnotched value. One of the objectives of the present study is to probe experimentally the interplay between the shear strength and the notched and unnotched tensile strengths of the composite as the state of the matrix is varied, from very weak to strong. A second objective is to assess the utility of an existing model for notch sensitivity[24] in describing the experimental results.

The article is organized in the following manner. A model for the notched strength of porous matrix composites is presented first, with a view to identifying the key governing material properties. This is followed by a description of the procedures used in composite fabrication and characterization as well as mechanical testing. The experiments are guided largely by the predictions of the model. An assessment of the model is then made through appropriate comparisons between the measurements and the predictions. The latter includes a proposed method of partitioning the fracture energy into contributions coming from two domains: before and after fiber bundle failure. Because of differences in the characteristic bridging length scales of the two bridging domains, their effects on notch sensitivity vary with notch length.

## II. A Model of Notched Strength

Numerical simulations probing the combined effects of shear and tensile bands on notch sensitivity of strength have been

D. J. Green—contributing editor

Manuscript No. 11008. Received May 5, 2004; approved December 9, 2004.
Funding for this work was provided by the Air Force Office of Scientific Research under contract number F49620-02-1-0128, monitored by Dr. B. L. Lee.
†Author to whom correspondence should be addressed. e-mail: zok@engineering.ucsb.edu

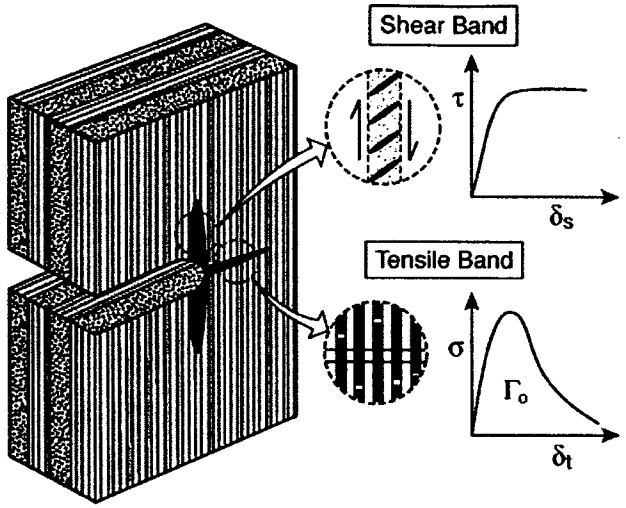


**Fig. 1.** Notch tip damage processes in porous matrix ceramic composites.

performed by He *et al.*[24] Here, the tensile band is treated as a cohesive zone and is represented mechanically by a continuous array of linear springs with a strength, $\sigma_0$, equal to the unnotched composite strength. Analogously, the shear band is treated as a rigid-perfectly plastic cohesive zone, with a shear strength, $\tau_0$. Two types of simulations have been performed. In the first, an infinite, elastically isotropic specimen with a semi-infinite notch is subjected to a remote displacement field prescribed by the square root singular solution and scaled with the stress intensity factor, $K$. The fracture toughness, $K_c$, is obtained when the maximum stress within the tensile band reaches its strength, $\sigma_0$. The corresponding fracture energy, $\Gamma$, is calculated from $K_c$ using the Irwin relation. The results of these simulations are plotted in Fig. 2(a). When $\tau_0/\sigma_0 \leq 0.2$, the fracture energy increases rapidly with decreasing $\tau_0/\sigma_0$, in approximate accordance with the power law indicated in the figure. In contrast, when $\tau_0/\sigma_0 \geq 0.2$, the fracture energy rapidly approaches the value intrinsic to the tensile band, $\Gamma_0$; the beneficial effect of the shear band on the fracture energy is lost.

In the second, a semi-infinite, elastically isotropic specimen with a *finite* notch of length $a_0$ is subjected to a uniform remote tension. The objective is to ascertain the degree of notch sensitivity of strength as the notch length and the material properties are varied. When plotted against the normalized notch length, $a_0\sigma_0^2/\bar{E}\Gamma$ ($\bar{E}$ being the plane strain modulus), the results for the normalized notch strength fall essentially onto a single, monotonically decreasing band, only weakly dependent on $\tau_0/\sigma_0$. Evidently, the beneficial effects of the shear band are embodied in the fracture energy, $\Gamma$, in the sense that reductions in $\tau_0/\sigma_0$ lead to an increase in $\Gamma$ and hence a reduction in notch sensitivity. Furthermore, the trend can be well described by the empirical formula

$$\frac{\sigma_N}{\sigma_0} = \left(1 + \frac{\pi\sigma_0^2 a_0}{\bar{E}\Gamma}\right)^{-1/2} \tag{1}$$

This formula is obtained essentially by interpolating between the strengths for the two limiting cases of very short and very long notches. In these limits, Eq. (1) yields: (i) $\sigma_N/\sigma_0 \rightarrow 1$ as $\pi\sigma_0^2 a_0/\bar{E}\Gamma \rightarrow 0$ (the notch insensitive domain) and (ii) $\sigma_N/\sigma_0 \rightarrow (\bar{E}\Gamma/\pi\sigma_0^2 a_0)^{1/2}$ (the Griffith stress) when $\pi\sigma_0^2 a_0/\bar{E}\Gamma \gg 1$.

The same formula has found use in describing notched strength in cases where fracture occurs exclusively through a tensile band (the shear band being absent). Here, again, Eq. (1) provides an accurate representation of numerical (finite element) results, within about 10%, for a variety of simple monotonic

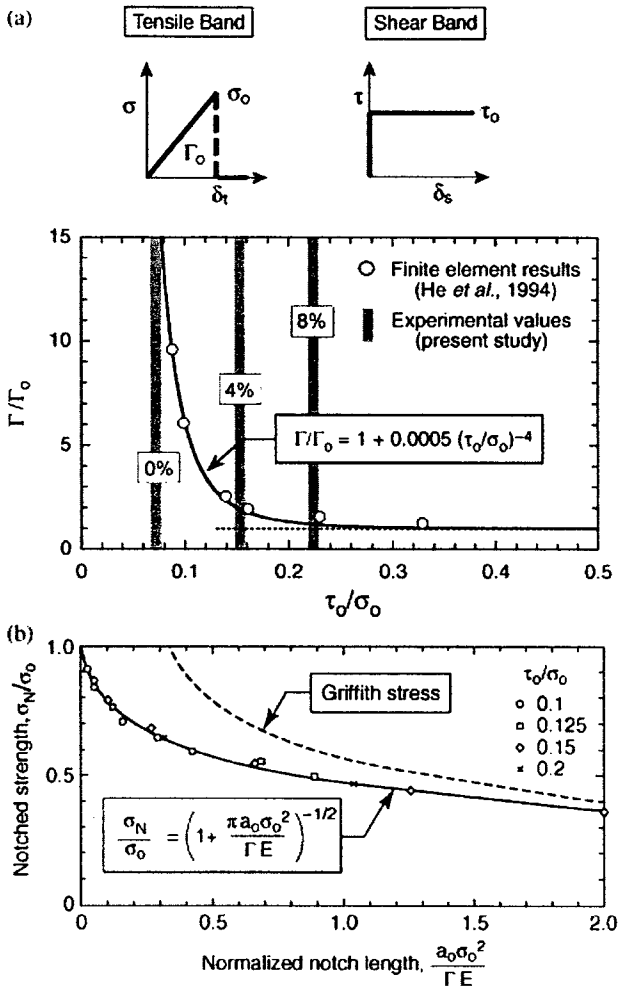


**Fig. 2.** Effects of strength ratio, $\tau_0/\sigma_0$, on: (a) normalized composite toughness (obtained in an infinite notched specimen) and (b) strength of an edge-notched semi-infinite specimen (adapted from He *et al.*[24]). Also shown in (a) are the pertinent strength ratios of the materials tested in this study, designated by the concentration of precursor-derived alumina in the matrix.

traction laws, including linear and parabolic hardening, linear softening, and rectilinear.[25] For more complex traction laws, *shape* plays an important role. For instance, when bridging is characterized by a two-level rectilinear law, there are two bridging stress levels and two fracture energies: features not embodied in Eq. (1). The ramifications of this deficiency are addressed further in Section VI.

Inspection of Eq. (1) reveals a characteristic length scale that dictates notch sensitivity, defined by

$$a_{ch} \equiv \frac{\bar{E}\Gamma}{\sigma_0^2} \tag{2}$$

With this definition, the notched strength formula can be written more compactly as

$$\frac{\sigma_N}{\sigma_0} = \left(1 + \frac{\pi a_0}{a_{ch}}\right)^{-1/2} \tag{3}$$

In this form, the role of $a_{ch}$ in the notch sensitivity can be ascertained. Two notable results emerge. (i) When $a_0 = a_{ch}$, the predicted strength ratio is very close to 0.5: a rather significant reduction, relative to unity. Only when $a_0 \ll a_{ch}$ is the notch sensitivity small, i.e. $\sigma_N/\sigma_0 \rightarrow 1$. In this context, $a_{ch}$ represents the pertinent length against which notch or flaw lengths must be compared in assessing the degree of notch sensitivity. (ii) A

complementary view of $a_{ch}$ is obtained by comparing the predictions of Eq. (3) with the Griffith stress. For instance, when $a_0 = a_{ch}$, the normalized Griffith stress (assuming all of the fracture energy is fully utilized in notched strength), is about 0.57: only 12% higher than the value predicted by Eq. (3). Thereafter, for $a_0 > a_{ch}$, the two predictions converge, allowing use of the Griffith stress in failure prediction. In this context, $a_{ch}$ can be viewed as the critical notch length beyond which Griffith-like behavior is obtained, with the associated inverse square root sensitivity of strength to notch length.

To compare the preceding predictions with experiment, Eq. (1) is modified to account for both finite specimen dimensions and elastic anisotropy. In the limit where $\pi\sigma_0^2 a_0/\bar{E}\Gamma \to 0$, the normalized notched strength (expressed on a *net-section* basis) approaches the same value, notably $\sigma_N/\sigma_0 \to 1$. In the Griffith limit, where $\pi\sigma_0^2 a_0/\bar{E}\Gamma \gg 1$, the energy release rate is modified to read as

$$G = \frac{\pi a_0 \sigma_0^2}{\bar{E}} g(\rho,\lambda) F^2\left(\frac{a_0}{W'}\frac{H}{W}\right)(1 - a_0/W)^2 \tag{4}$$

where $W$ is the specimen width, $H$ is the specimen length, $F(a_0/W, H/W)$ is a non-dimensional function that depends on both the specimen geometry and the loading configuration,[26] $g(\rho,\lambda)$ characterizes the effect of orthotropy,[27,28] and $\rho$ and $\lambda$ are defined by

$$\lambda \equiv \frac{E_1}{E_2} \tag{5}$$

$$\rho \equiv \frac{(E_1 E_2)^{1/2}}{2\mu_{12}} - (\nu_{12}\nu_{21})^{1/2} \tag{6}$$

with the subscripts 1 and 2 referring to the principal material axes, $\mu$ the shear modulus, and $\nu$ Poisson's ratio. Composites with balanced symmetric fiber lay-ups exhibit cubic in-plane symmetry, whereupon $\lambda = E_1/E_2 = 1$ and $\nu_{12} = \nu_{21}$, and $g(\rho,\lambda)$ is given by

$$g(\rho,\lambda) = \left(\frac{1+\rho}{2}\right)^{1/2}(1 + 0.1(1-\rho) - 0.016(1-\rho)^2 + 0.002(1-\rho)^3) \tag{7}$$

Upon setting $G = \Gamma$, the notched strength becomes

$$\frac{\sigma_N}{\sigma_0} = \left(\frac{\Gamma\bar{E}}{\pi a_0 g(\rho,\lambda)\left[\sigma_0 F\left(\frac{a_0}{W'}\frac{H}{W}\right)(1 - a_0/W)\right]^2}\right)^{1/2} \tag{8}$$

Interpolating between the two limits, in a manner analogous to that used to obtain Eq. (1), gives the notched strength as

$$\frac{\sigma_N}{\sigma_0} = \left(1 + \frac{\pi a_0 g(\rho,\lambda)\left[\sigma_0 F\left(\frac{a_0}{W'}\frac{H}{W}\right)(1 - a_0/W)\right]^2}{\Gamma\bar{E}}\right)^{-1/2} \tag{9}$$

In light of this result, the definition of the characteristic bridging length $a_{ch}$ is modified to take into account both the elastic anisotropy as well as the finite specimen width:

$$a_{ch} \equiv \frac{\bar{E}\Gamma}{g(\rho,\lambda)\left[\sigma_0 F\left(\frac{a_0}{W'}\frac{H}{W}\right)(1 - a_0/W)\right]^2} \tag{10}$$

With the modified definition, the notched strength formula in Eq. (9) reduces to the one in Eq. (3).

An assessment of Eq. (9) is made through comparison with the experiments described in the following sections. The model identifies five fundamental material properties that govern notched strength: the elastic constants $E_1$, $\nu_{12}$, and $\mu_{12}$, the unnotched tensile strength, $\sigma_0$, and the fracture energy, $\Gamma$. Additional insights into the contributions from shear deformation to notch sensitivity are obtained through measurement of the shear strength, $\tau_0$, in combination with the results plotted in Fig. 2(a). The elastic constants and the strengths are obtained from standard instrumented tension and shear tests, whereas the fracture energy is estimated from the work of fracture in notched tension tests. The latter tests are performed on specimens with varying notch lengths, for the purpose of establishing the dependence of strength on size.

## III. Materials

The composites were comprised of seven layers of Nextel 720 fiber cloth in an 8-harness satin weave and a porous matrix of mullite and alumina. The processing route was essentially identical to that described in earlier articles.[17,18] Briefly, the matrix was introduced in two steps: (i) vacuum infiltration of a slurry containing 80% mullite and 20% alumina particles into the fiber preform and (ii) impregnation and pyrolysis of an alumina precursor solution ($Al_2Cl(OH)_5$). The effective volumetric yield of the precursor solution upon conversion to $\gamma$-alumina, determined in the manner described below, was 6.4%. To prevent segregation of the precursor during drying, the panels were gelled by placing them in a chamber containing gaseous $NH_4OH$ for 6 h immediately following impregnation. After drying, the panels were fired at 900°C for 2 h, thereby converting the precursor to $\gamma$-alumina. After all impregnation cycles were completed, the panels were given a final heat treatment at 1200°C for 2 h. In the latter step, the $\gamma$-alumina is converted to $\alpha$-alumina. The average fiber volume fraction was 38%.

Three different composites were fabricated, distinguished from one another by the number of precursor impregnation and pyrolysis cycles. Selection of the pertinent range was based in part on the results of a separate study, focused on the effects of the volume fraction of precursor-derived alumina, $V_{PDA}$, on matrix properties.[29] The results of the latter study, coupled with the He and Hutchinson[30] crack deflection criterion, suggest that the deflection condition is not satisfied once $V_{PDA}$ exceeds a critical value of about 9%–10%. With the current precursor, this critical value is achieved after five impregnation and pyrolysis cycles. Consequently, to explore the effects of matrix strength, all within the crack deflection domain, panels were fabricated with either zero, two, or four impregnation cycles.

Matrix porosity and concentration of PDA were measured using the Archimedes method.[31] The initial matrix porosity (following slurry infiltration but prior to precursor impregnation) was $p_m^0 = 39\%$. Assuming that the pore space remains open during processing and the precursor solution completely fills the pore volume during each impregnation, the matrix porosity after $N$ impregnation cycles is predicted to follow the relation

$$p_m = p_m^0\left(1 - (1 - (1 - y_p)^N)\frac{\rho_\gamma}{\rho_\alpha}\right) \tag{11}$$

where $p_m$ is the matrix porosity, $y_p$ is the precursor yield (upon conversion to $\gamma$-alumina), and $\rho$ is the density of the PDA in the $\alpha$ or $\gamma$ states. The precursor yield ($y_p = 6.4\%$) was calculated from Eq. (11) using the measured values of $p_m$ and $p_m^0$ for both $N = 2$ and 4. The change in porosity following precursor impregnation was also used to determine the $V_{PDA}$, as summarized in Table I. The latter spans the targeted range, from 0% to 8%.

The effect of PDA concentration on matrix strength was characterized through hardness measurements. For this purpose, Vickers indentations were made on polished cross-sections

**Table I. Summary of Elastic Constants and Anisotropy Parameters as a Function of Precursor Concentration**

| $N$ | $V_{PDA}$ (%) | $E_1$ (GPa) | $\nu_{12}$ | $\mu_{12}$ (GPa) | $\rho$ | $g(\rho)$ |
|---|---|---|---|---|---|---|
| 0 | 0 | 48.3 | 0.06 | 4.3 | 5.5 | 3.1 |
| 2 | 3.9 | 56.1 | 0.10 | 8.4 | 3.3 | 2.0 |
| 4 | 8.2 | 63.0 | 0.13 | 14.0 | 2.2 | 1.5 |

PDA, precursor-derived alumina.

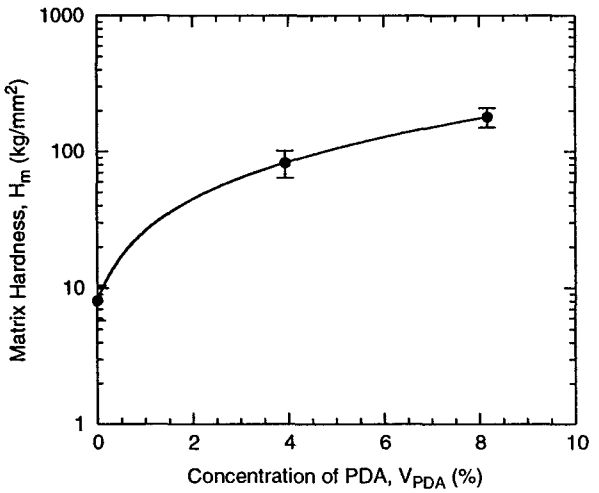


**Fig. 3.** Variation in matrix hardness with precursor-derived alumina (PDA) concentration.

within matrix-rich regions between the fiber cloths, with a mass of 200 g. The results from such measurements, plotted in Fig. 3, reveal a strong sensitivity of matrix hardness, $H_m$, to $V_{PDA}$, increasing by more than an order of magnitude over the range $V_{PDA} = 0\%–8\%$. Moreover, they demonstrate that the alumina derived from the precursor has a much stronger influence on the matrix than that associated with the particulates in the slurry. For instance, the addition of less than 1% PDA has the effect of doubling the matrix hardness, relative to the unimpregnated material containing 20% alumina in particulate form.

Hereafter, experimental results for various composite properties are presented in terms of either the PDA concentration or the matrix hardness, as appropriate. Their connections to the number of precursor impregnation cycles can be established through the results plotted in Fig. 3 and summarized in Table I.

## IV. Mechanical Testing Procedures

A variety of mechanical tests were performed on each of the three composite panels, with the goal of assessing the degree of notch sensitivity of strength in the 0°/90° orientation. To this end, measurements were made of the key properties described above, notably: the elastic constants $E_1$, $\nu_{12}$, and $\mu_{12}$, the unnotched tensile strength, $\sigma_0$, the shear strength, $\tau_0$, and the fracture energy, $\Gamma$. A secondary objective was to assess the effects of matrix strength on the pertinent composite properties.

The unnotched tensile strengths were measured using uniaxial tensile bars, approximately 10 mm wide, and with gauge lengths, $L$, of either 20 or 64 mm. (The rationale for probing gauge length effects stems from the length of the fracture process zone in the notched specimens, as described below.) The displacement rate was 0.012 mm/min. In all cases, the longitudinal strains were measured both through a non-contacting laser extensometer and a strain gauge. Transverse strains were also measured with a strain gauge.

To assess the effects of the matrix on the 0°/90° strength, the tensile properties of dry fiber cloth were also measured,

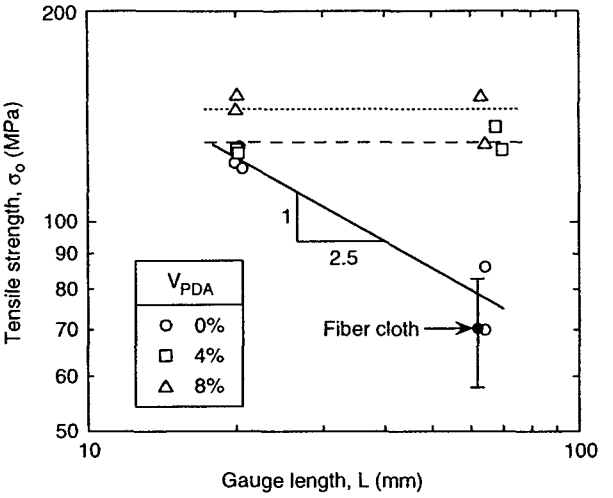


**Fig. 4.** Effects of gauge length and matrix hardness on unnotched tensile strength.

using test coupons with a gauge length of 64 mm (identical to the length of one set of composite specimens) and a gauge width of 10 mm. Test samples were cut from the same fiber cloth used in composite fabrication and fired at 550°C for 2 h to remove the factory-applied sizing. The sample ends were tabbed with silicone rubber and clamped between frictional grips for testing.

Notch sensitivity of strength was examined through single-edge notched tension tests (SENT).[‡] The ratio of notch length to specimen width was fixed at 0.5 and scale effects were probed by varying the specimen width, from 12 to 24 mm. The height to width ratio was fixed at 2.5. Crack mouth opening displacements were measured using a spring-loaded gauge mounted between knife blades affixed to the sample. The remote displacement was also monitored using an LVDT. Additionally, the sequence of damage events leading to fracture was obtained by optical imaging of the external specimen surface. To enhance the contrast associated with such damage, the surfaces were coated with a thin (30 nm) layer of Au–Pd.

The in-plane shear response was measured using the Iosipescu test in the 0°/90° orientation.[32] Specimens were 19 mm wide with symmetrical V-notches, each 3.8 mm deep, with an included angle of 105°. Gauges were mounted at ±45° to measure shear strains. The tests were performed at a displacement rate of 0.05 mm/min.

## V. Experimental Measurements and Observations

### *(1) Unnotched Tensile Properties*

Figure 4 demonstrates the effects of gauge length and PDA concentration on the unnotched tensile strength. The unimpregnated composite exhibits a significant sensitivity of strength to gauge length, diminishing by about 1/3, from 120 to 80 MPa, over the range $L = 20–64$ mm. In contrast, the composites with either 4% or 8% PDA show no apparent length dependence. Furthermore, the tensile strength increases with $V_{PDA}$ for constant gauge length. For $L = 20$ mm, the strength improvement is a modest 10%–15% over the range $V_{PDA} = 0\%–8\%$; for $L = 64$ mm, the increase is more substantial, approaching 60%. Changes in $E_1$ and $\nu_{12}$ are also observed over this range of PDA concentrations (Table I). Modulus rises 30%, from 48 to 63 GPa, while Poisson's ratio increases nearly twofold, from 0.06 to 0.13.

Also shown for comparison in Fig. 4 is the strength of the fiber cloth, taken to be the product of the fiber volume fraction

[‡]With clamped ends, SENT provides a more critical assessment of notch sensitivity than double edge notched tension (DENT), because of the higher stress intensity at a prescribed normalized notch length, $a_0/W$. A secondary advantage of SENT is that it requires significantly less material for testing; both the specimen width and the specimen length are one half of the values needed for DENT at a fixed $a_0/W$.

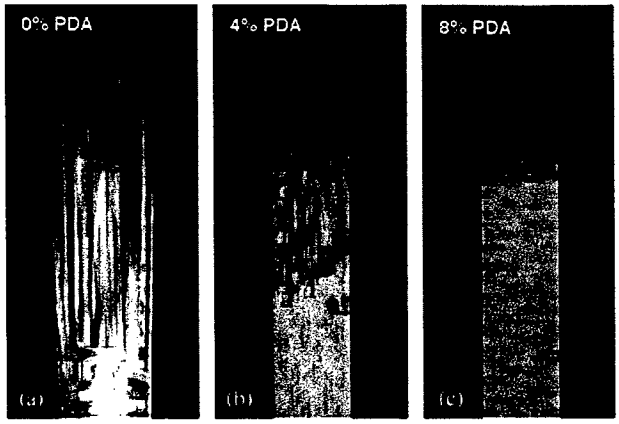


**Fig. 5.** Macrophotographs of fractured tensile specimens, showing reduction in degree of fiber pullout with increasing precursor-derived alumina (PDA) concentration.

(38%) and the mean cloth strength (186±33 MPa). The resulting value (71±13 MPa) is in reasonable agreement with the mean strength (about 80 MPa) of the composite with no PDA. This correlation indicates that the composite strength is dictated entirely by the fiber cloth, with no beneficial effect of the matrix. Moreover, it suggests that the gauge length dependence of the strength of this composite can be rationalized on the basis of the corresponding length dependence of the cloth itself. Assuming a Weibull distribution for the fiber strength, the predicted length dependence is given by

$$\frac{\sigma}{\sigma_0} = \left(\frac{L}{L_0}\right)^{-1/m} \tag{12}$$

where $\sigma_0$ and $L_0$ are the reference strength and reference length, respectively. From the slope of the line in Fig. 4 (presented in log–log coordinates), $m$ is estimated to be about 2.5±0.4. (Comparisons of $m$ with previously reported values on pristine fibers is problematic, since the latter values span the range of 2.8–26, depending on the method.[33–35] Further, these values pertain only to pristine fibers and may not accurately represent the fiber condition after weaving.)

Accompanying the elevations in strength with $V_{PDA}$ is a change in the appearance of the fracture surfaces (Fig. 5). In the unimpregnated composite, fiber pullout is extensive, with long exposed fiber lengths. As the matrix strength is increased with PDA addition, a significant reduction in pullout lengths is apparent. This observation is qualitatively consistent with models of fiber fragmentation and bundle failure, where pullout lengths are predicted to fall with elevations in interface properties.[22]

### *(2) Notched Tensile Properties*

The notched tensile response and associated damage mechanisms are shown in Figs. 6–8. For samples with $V_{PDA} = 0\%$, the first apparent damage event is a shear band at the notch tip, located at the boundary between fiber tows (Fig. 6(a)), and is manifested in the onset of non-linearity in the stress–displacement response (Fig. 7). As the stress increases, additional shear bands form along tow boundaries, with small intervening tensile cracks (the latter only barely evident on Fig. 6(a)). The shear bands extend to a distance of about 10 mm on either side of the notch plane. The sequence of shear banding and tensile cracking proceeds until all fiber bundles have fractured. The subsequent response exhibits significant softening as the broken fibers pull out, presumably resisted by friction as they slide past the surrounding matrix. The spatial extent of the damage and the pullout is evident in the low-magnification image of a typical fractured specimen, shown in Fig. 8(a).

For composites with the intermediate matrix ($V_{PDA} = 4\%$), a similar sequence of damage events accompanies fracture. However, in this case, the length of the shear bands and the extent of fiber pullout are reduced significantly, as seen in the sequence shown in Fig. 6(b) as well as the fractured specimen in Fig. 8(b). Additionally, the peak stress is lower and occurs at a lower value of remote displacement, the latter being consistent with the reduced shear band length.

For the composites with the strongest matrix ($V_{PDA} = 8\%$), shear banding is almost negligible. Instead, fracture occurs essentially by the propagation of a single tensile crack, with some meandering from a pure mode I path. This view is consistent with the rather narrow band of damage and short pullout lengths seen on the fracture surface (Fig. 8(c)). Accompanying this diminished shear banding is a further reduction in the peak stress and the corresponding displacement.

Figure 9 summarizes the effects of notch length and precursor addition on the notched strength. In all materials, some notch sensitivity is observed, with strength diminishing with increasing notch length. Further, the degree of notch sensitivity increases with PDA concentration. Over the range $a_0 = 0$–12 mm, the unimpregnated composite strength falls approximately 25%. In contrast, the densest composite ($V_{PDA} = 8\%$) exhibits a 60% strength reduction over the same notch length range. These trends suggest strong dependence of notch sensitivity on the spatial extent of the shear bands, in qualitative agreement with the theoretical results presented in Section II. A quantitative assessment is made in Section VI.

### *(3) Shear Properties*

Changes in shear response with PDA concentration are shown in Fig. 10. In each case, the response is essentially elastic–plastic, with only modest strain hardening. Failure occurs through the formation of a localized damage band across the specimen section, leading to a plateau stress at a strain of 2%–3%: well beyond the tensile failure strain of the fibers. This behavior is reminiscent of the shear response of fiber composites with ductile matrices, including both polymers and metals. Further, there is a pronounced sensitivity of the shear modulus and strength to the state of the matrix. Roughly fourfold increases in both properties are obtained as the PDA concentration is increased from 0% to 8%, with the shear modulus rising from 4 to 14 GPa (Table I) and the strength increasing from 8 to 32 MPa.

These elastic–plastic characteristics suggest that the composite shear strength should scale with the shear "flow stress" of the matrix, as obtained in metal and polymer matrix composites. Using the Tresca yield criterion (applicable to materials that deform by dislocation plasticity), the matrix shear strength is predicted to be half the uniaxial yield stress. Furthermore, the uniaxial yield stress is roughly three times the matrix hardness, $H_m$. Upon combining these results, the predicted composite shear strength is about $H_m/6$.

Figure 10(b) shows the dependence of the composite shear strength on matrix hardness. For the weakest matrix, the composite strength is consistent with the rudimentary prediction: $H_m/6$. For stronger matrices, the shear strength rises with matrix hardness, but at a much lower rate than predicted. The discrepancy is likely because of the assumed form of the yield criterion. Specifically, the porous ceramic matrix likely follows a different yield condition (not the Tresca criterion). The discrepancy highlights the need for the development of appropriate flow laws for the porous matrices, for use in predicting composite properties.

## VI. Analysis of Notch Sensitivity

The predicted notched strengths from the model presented in Section II have been calculated using Eq. (9) in combination with the measured elastic constants $E_1$, $\mu_{12}$, and $G_{12}$, the unnotched tensile strength, $\sigma_0$, and the work of fracture, $\Gamma$. The elastic parameters and corresponding anisotropy function $g(\rho)$ are summarized in Table I. Because of the absence of gauge

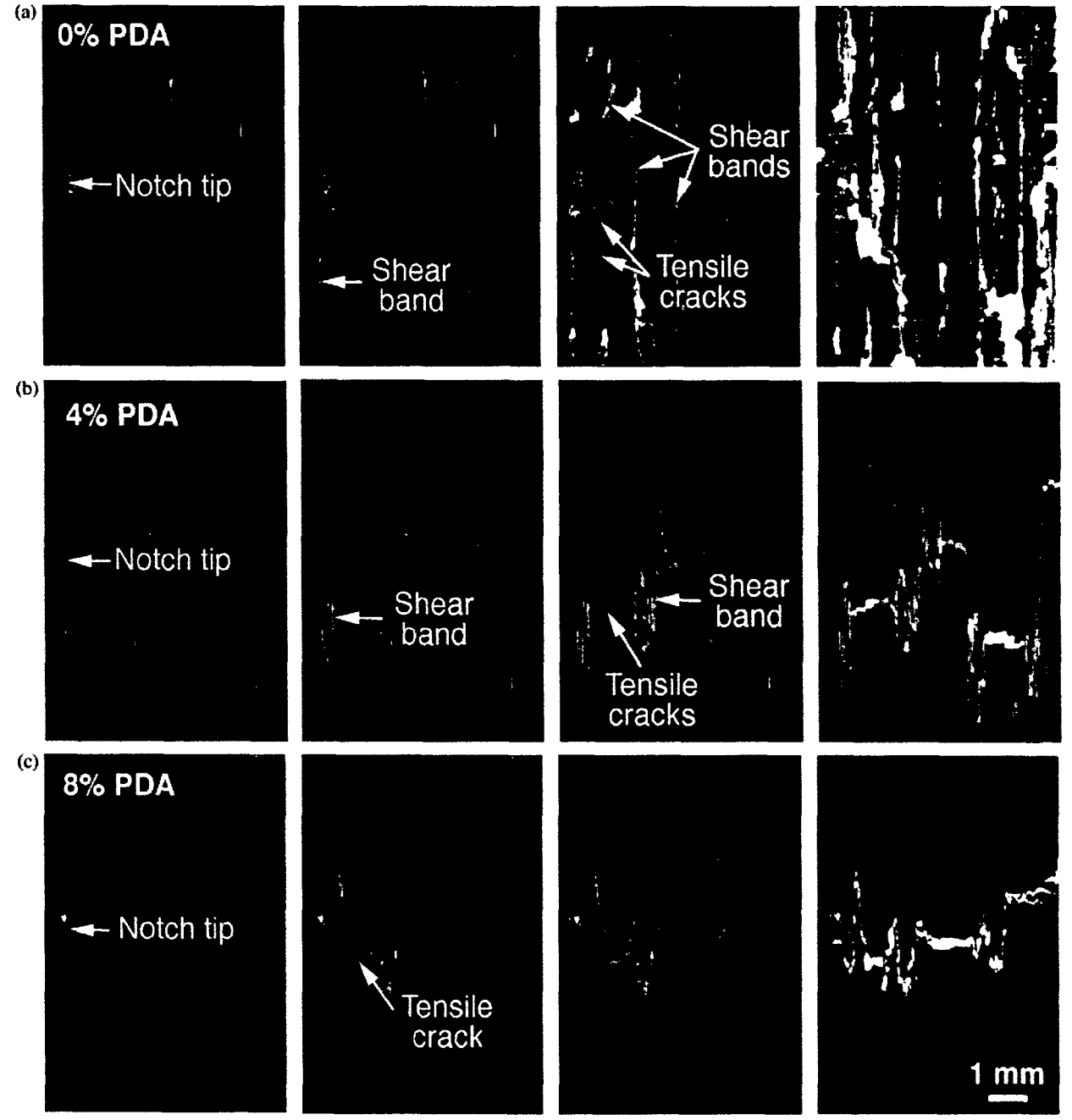


**Fig. 6.** Progression of damage in edge-notched tensile specimens: (a) $V_{PDA} = 0$, (b) $V_{PDA} = 4$, (c) $V_{PDA} = 8$. In each sequence, the first picture represents the pristine (unloaded) specimen. The subsequent images are at progressively increasing displacements, indicated in Fig. 7. PDA, precursor-derived alumina.

length dependence in materials with either 4% or 8% PDA, $\sigma_0$ was taken to be the average of all measured unnotched tensile strengths (including both 20 and 64 mm gauge lengths). In contrast, for the unimpregnated material, only the values measured for the 20 mm gauge length were used, since this value corresponds more closely to the length of the damage zone at the notch tip. $\Gamma$ was measured from the area under the load–displacement curves from the notched tests.

Comparisons between the predictions and the experiments are presented in Fig. 11. In general, the predictions lie above the measured values. Additionally, the magnitude of the discrepancy increases from roughly 10% to over 40% as the PDA concentration is increased from 0% to 8%. The discrepancy is believed to be associated mainly with the *shape* of the traction law, as described below.

The stress–displacement curves in Fig. 7, as well as previous theoretical models of fiber failure and pullout, suggest that the bridging traction law can be partitioned into two parts[§] (Fig. 12). The first is characterized by rapid hardening, a high peak stress (comparable with the unnotched strength), and a small critical displacement, with a fracture energy denoted $\Gamma_i$. In this domain, the inelastic displacement occurs through matrix cracking and associated interfacial debonding and sliding, with minimal fiber failure. The second part is characterized by exponential softening, a low strength (that because of pullout of broken fibers), and a large critical displacement (dictated by the pullout length). In this domain, virtually all fibers are broken.

[§]A similar two-part traction model has been used to rationalize notch sensitivity in fiber-reinforced Ti-matrix composites.[36]

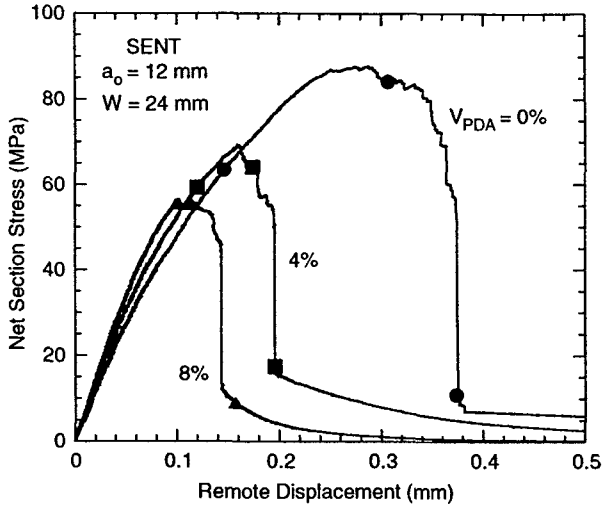


**Fig. 7.** Stress–displacement response of single-edge notched tension tests (SENT) specimens. Symbols represent the coordinates corresponding to the micrographs in Fig. 6.

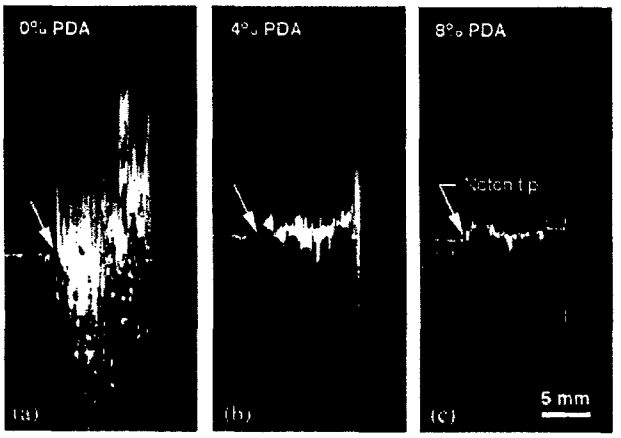


**Fig. 8.** Macrophotographs of fractured notched tensile specimens.

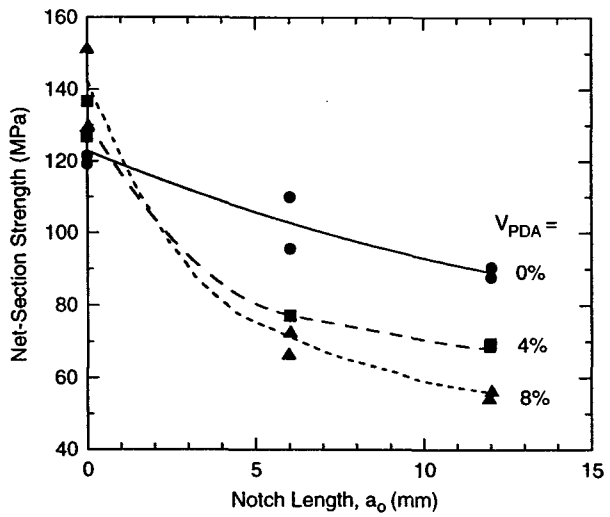


**Fig. 9.** Notched strength as a function of notch length and precursor-derived alumina (PDA) concentration.

The pullout process yields additional fracture energy, $\Gamma_p$, yielding a total, $\Gamma = \Gamma_i + \Gamma_p$. Despite differences in their shapes, each of the two bridging laws contributes a comparable amount to the total fracture energy. The notch length range in which each

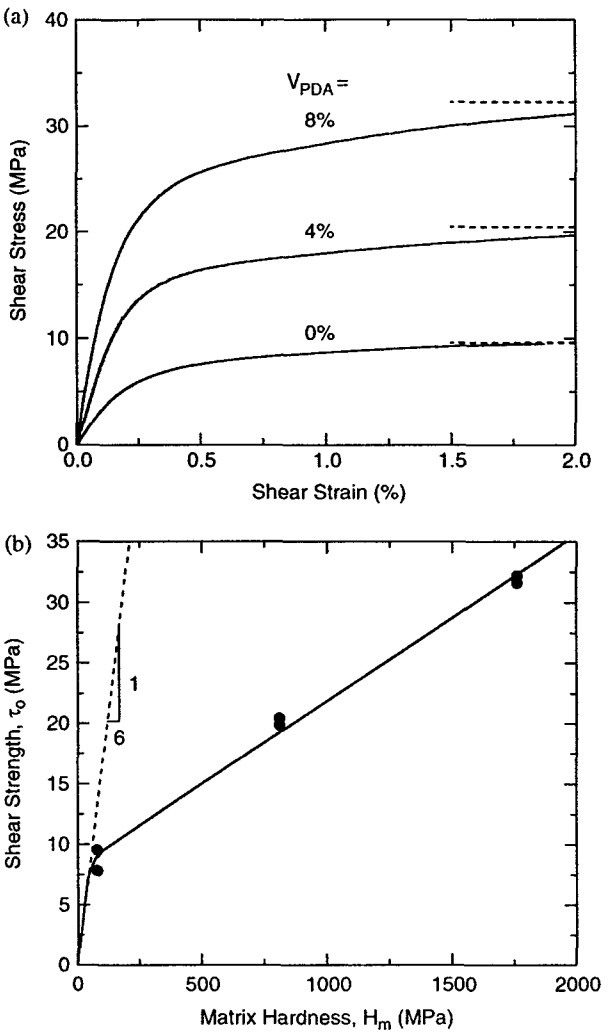


**Fig. 10.** Related effects of precursor-derived alumina (PDA) concentration and matrix hardness on composite shear properties: (a) stress–strain response and (b) shear strength. Dashed lines in (a) denote limit stress values at larger strains. Also shown in (b) is the expected trend for a ductile matrix composite (dashed line), subject to the Tresca yield criterion.

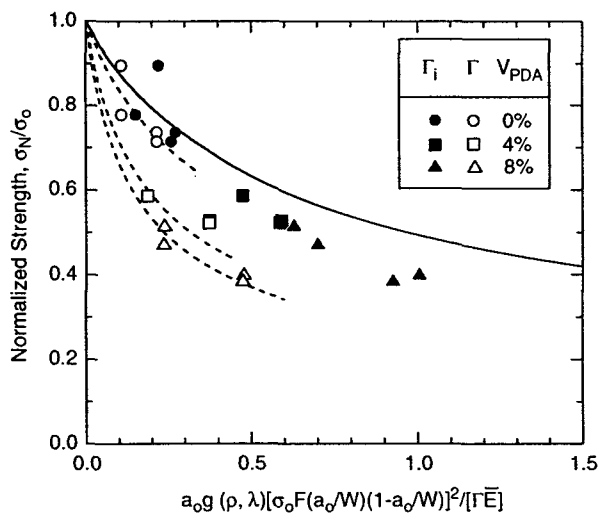


**Fig. 11.** Variation in notched strength with normalized notch length. Solid line is prediction of Eq. (9). Open symbols are experimental values, calculated using the total measured fracture energy; solid symbols are experimental values, calculated using the fracture energy without the pullout contribution.

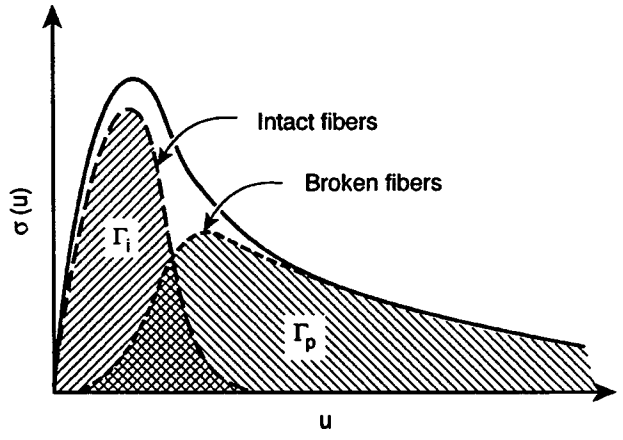


**Fig. 12.** Partitioning of the bridging traction law. Total stress is the number-weighted average of contributions from intact and broken fibers. $\Gamma_i$ and $\Gamma_p$ represent the energies associated with deformation of intact fibers and pullout of broken fibers, respectively.

has a significant effect on notch sensitivity depends on the characteristic bridging length scale, calculated using Eq. (2), with the appropriate value of fracture energy.[37] Specifically, the length $a_i$ pertinent to the first part of the bridging law is obtained using $\Gamma_i$ in Eq. (2), whereas the length $a_p$ where pullout plays a significant role is found using the total fracture energy: $\Gamma_i+\Gamma_p$. When $a_0 < a_i$, notch sensitivity is dictated by the first part of the bridging law; pullout contributes significantly to notched strength only at larger values of notch length: $a_0 > a_p$.[36]

This energy partitioning scheme was implemented in the following way. The pullout contribution was obtained from the stress–displacement curves of the notched specimens at large displacements where all fibers are clearly broken. Assuming that the pullout lengths follow an exponential distribution and that the fibers are resisted by friction, with a sliding stress, $\tau_s$, the predicted response for a 2D fiber composite in a 0°/90° orientation is[38,39]

$$\sigma = \frac{V_f \tau_s h_0}{R} \exp\left(-\frac{u}{h_0}\right) \tag{13}$$

where $u$ is the inelastic remote displacement, $R$ is the fiber radius, and $h_0$ is the mean pullout length. Representative curves from each of the three materials, shown in Fig. 13, confirm the validity of Eq. (13) in this domain. The inferred values of $h_0$ and $\tau_s$ are plotted in Fig. 14. Strictly, the contribution from pullout at smaller displacements is obtained by weighting the pullout stress by the number fraction of broken fibers, as shown schematically by the dotted curve in Fig. 12. The corresponding pullout energy, $\Gamma_p$, is the integral of this weighted traction law over the displacement interval $0-\infty$. Information on the fraction of broken fibers being absent, the pullout energy is estimated by extrapolating the exponential law (assuming all fibers are broken) back to the peak stress and then integrating over the appropriate limits. Although the details of the traction law are likely in error in the transition where the fiber failure rate is high (overestimating the bridging stress in some parts and underestimating it in others), the fracture energy is likely captured adequately, since most of it is dissipated at larger displacements. The fracture energy pertinent to notch sensitivity in the short notch domain, $\Gamma_i$, is then taken as the difference: $\Gamma-\Gamma_p$. The results of this energy partitioning are summarized in Fig. 15. They demonstrate that $\Gamma_p$ represents a significant fraction of $\Gamma$, especially for large values of $V_{PDA}$.

To justify use of $\Gamma_i$ in notched strength predictions, the values of $a_i$ and $a_p$ have been calculated from Eq. (10) and the fracture energies in Fig. 15, and compared with $a_0$ in Fig. 16. In the intact

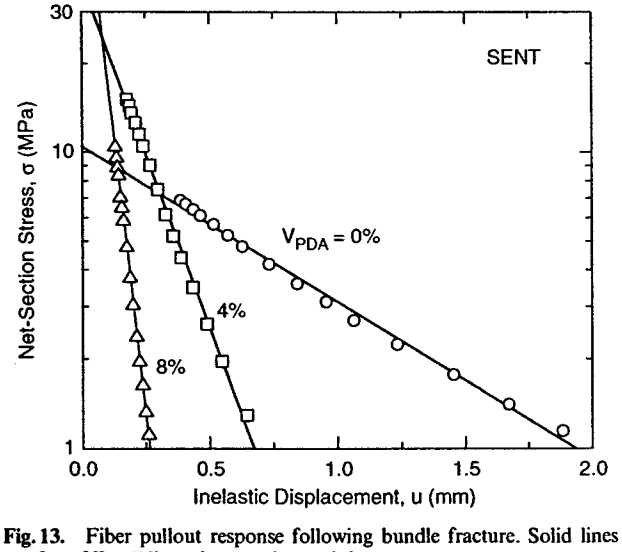


**Fig. 13.** Fiber pullout response following bundle fracture. Solid lines are fits of Eq. (13) to the experimental data.

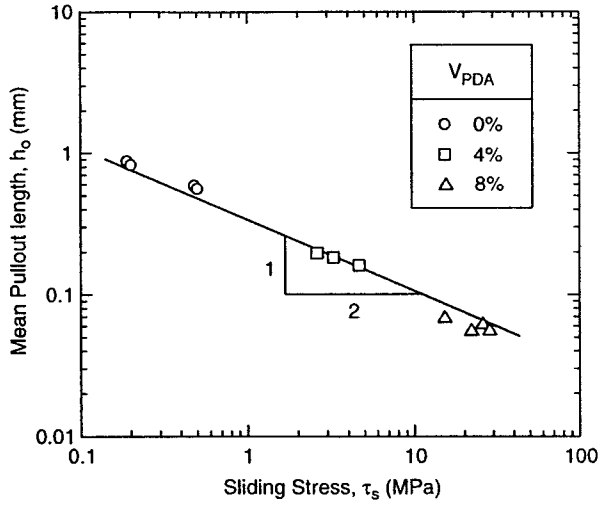


**Fig. 14.** Effects of precursor-derived alumina (PDA) concentration on both interface sliding stress and mean fiber pullout, as determined from the pullout response (Fig. 13).

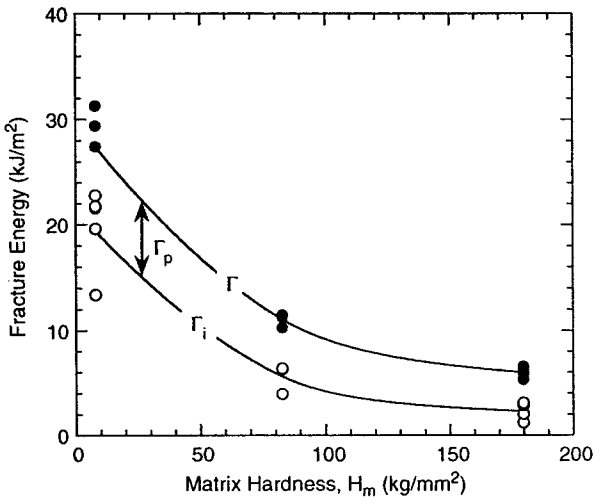


**Fig. 15.** Effects of matrix hardness on the total fracture energy, $\Gamma$, and the fracture energy without the pullout contribution, $\Gamma_i$.

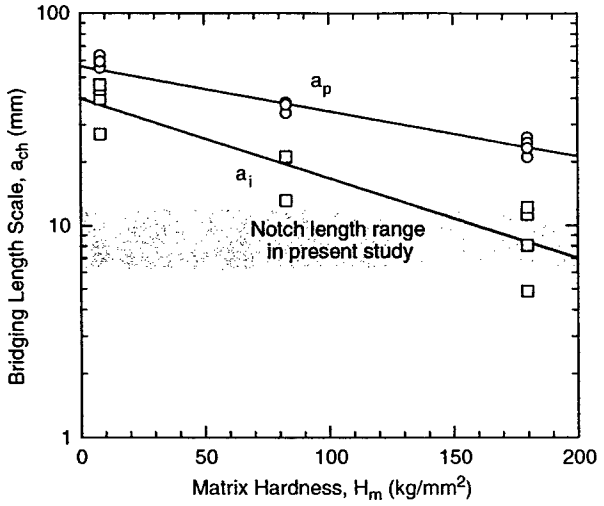


**Fig. 16.** Comparisons of bridging length scales $a_i$ and $a_p$ with the notch lengths used in the present study.

fiber domain, $a_i$ falls in the range of 10–40 mm, decreasing with increasing $V_{PDA}$. This range is comparable with (but generally somewhat greater than) the notch lengths used in the present experiments ($a_0$ = 6–12 mm). The values in the pullout domain range from 20 to 60 mm, considerably larger than $a_0$. The inference is that bridging from pullout contributes little to the notched strength over the current notch length range, but would become significant for notch lengths on the order of several centimeters.

Revised strength predictions utilizing $\Gamma_i$ as the fracture energy in Eq. (9) are shown in Fig. 11. In this case, the data for all materials collapse onto essentially a single band, independent of $V_{PDA}$. Furthermore, the model predictions are considerably closer to the experimental measurements (within about 10%–20%). These results provide confidence in the proposed energy partitioning method for ascertaining the contribution pertinent to short notches and provides preliminary validation of the modified strength formula in Eq. (9).

Insights into the effects of PDA concentration on notch sensitivity are obtained by considering changes in the parameter values that control the bridging length scale, $a_{ch}$ (Eq. (10)). Over the PDA range probed in this study, $\sigma_0$ and $\bar{E}$ increase by about 20% and 30%, respectively. Being fiber-dominated properties, they exhibit the weakest sensitivity to the state of the matrix. Furthermore, their changes have essentially offsetting effects on $a_{ch}$. In contrast, $g(\rho,\lambda)$ depends on a matrix-sensitive property, notably the shear modulus. Consequently, it decreases by a greater amount: a factor of about 2. This change produces a proportionate twofold increase in $a_{ch}$. $\Gamma_i$ is by far the most matrix sensitive, because of its strong dependence on the composite shear strength, as illustrated in Fig. 2. Indeed, it decreases by almost an order of magnitude, resulting in a proportionate (nearly 10-fold) reduction in $a_{ch}$. The latter reduction in $a_{ch}$ is significantly greater than the corresponding increase because of $g(\rho,\lambda)$. The net result of these dependencies is a decrease in $a_{ch}$, by a factor of about 4, and hence an increase in notch sensitivity, in accordance with Eq. (3).

## VII. Summary

The strength and notch sensitivity of a family of porous-matrix composites have been examined experimentally. The unnotched tensile and shear strengths can be increased by strengthening the matrix, via addition of a PDA, but the benefits are offset by an increase in notch sensitivity.

A model, based originally upon finite element simulations, has been used to rationalize the degree of notch sensitivity. The simulations account for the interactions between notch tip tensile and shear bands in semi-infinite, notched specimens of elastically isotropic composites. By interpolating between the limiting cases of very short and very long notches, a simple formula for notched strength is obtained. This formula has been modified to account for the effects of elastic anisotropy and finite sample size, allowing comparison with the experimental measurements.

Predictions of the notched strength overestimate the experimental measurements when the *total* (measured) fracture energy is used. This discrepancy arises because of the two dissimilar parts of the bridging law. To remedy the problem, a method for partitioning the bridging law and the associated fracture energies has been proposed and implemented. For the range of notch lengths used in the present study, notch sensitivity is dictated by the initial rising part of the bridging law, where the fibers are largely intact. Use of the fracture energy from this part of the bridging law in combination with the notched strength formula yields predictions that are in reasonable agreement with the measurements. The choice of this fracture energy can be justified on the basis of the characteristic bridging length scales of the two parts of the bridging law relative to the notch length.

Effects of PDA concentration on notch sensitivity can be rationalized in terms of the characteristic bridging length scale, which, in turn, is dictated by the interplay between $\sigma_0$, $\bar{E}$, $g(\rho,\lambda)$, and $\Gamma_i$ in Eq. (3). The net result is a decreasing $a_{ch}$ and hence heightened notch sensitivity with increasing PDA concentration.

Finally, the model of notch sensitivity presented here would be applicable to other ceramic composites with weak matrices, such as C/C and SiC/C.[40] In these systems, fracture of notched specimens is accompanied by formation of shear bands perpendicular to the notch plane, in a manner similar to that of the present oxide composites.

## References

[1]P. E. D. Morgan and D. B. Marshall, "Ceramic Composites of Monazite and Alumina," *J. Am. Ceram. Soc.*, **78** [6] 1553–63 (1995).

[2]J. B. Davis, D. B. Marshall, and P. E. D. Morgan, "Oxide Composites of $Al_2O_3$ and $LaPO_4$," *J. Eur. Ceram. Soc.*, **19** [13–14] 2421–6 (1999).

[3]A. Szweda, M. L. Millard, and M. G. Harrison, "Fiber-Reinforced Ceramic Composite Member"; U.S. Patent No. 5 017 522, May 21, 1991.

[4]A. Szweda, M. L. Millard, and M. G. Harrison, "Fiber-Reinforced Ceramic–Matrix Composite Member and Method for Making"; U.S. Patent No. 5 601 674, February 11, 1997.

[5]S. C. Jurf and R. A. Butner, "Advances in Oxide–Oxide CMC," *J. Eng. Gas Turb. Power*, **122** [2] 202–5 (2000).

[6]L. P. Zawada, "Longitudinal and Transthickness Tensile Behavior of Several Oxide/Oxide Composites," *Ceram. Eng. Sci. Proc.*, **19** [3] 327–39 (1998).

[7]L. P. Zawada, R. S. Hay, S. S. Lee, and J. Staehler, "Characterization and High-Temperature Mechanical Behavior of an Oxide/Oxide Composite," *J. Am. Ceram. Soc.*, **86** [6] 981–90 (2003).

[8]S. G. Steel, L. P. Zawada, and S. Mall, "Fatigue Behavior of a Nextel 720/Alumina Composite at Room and Elevated Temperature," *Ceram. Eng. Sci. Proc.*, **22** [3] 695–702 (2001).

[9]B. Kanka and H. Schneider, "Aluminosilicate Fiber/Mullite Mullite Composites with Favorable High-Temperature Properties," *J. Eur. Ceram. Soc.*, **20** [14–15] 619–23 (2000).

[10]J. She, P. Mechnich, H. Schneider, M. Schumücker, and B. Kanka, "Effect of Cyclic Infiltrations on Microstructure and Mechanical Behavior of Porous Mullite/Mullite Composites," *Mater. Sci. Eng. A.*, **325** [1–2] 19–24 (2002).

[11]V. A. Kramb, R. John, and L. P. Zawada, "Notched Fracture Behavior of an Oxide/Oxide Ceramic–Matrix Composite," *J. Am. Ceram. Soc.*, **82** [11] 3087–96 (1999).

[12]V. A. Kramb, R. John, and D. A. Stubbs, "A Study of the Damage Progression from Notches in an Oxide/Oxide Ceramic–Matrix Composite Using Ultrasonic C-Scans," *Comp. Sci. Technol.*, **61** [11] 1561–70 (2001).

[13]E. Mouchon and P. Colomban, "Oxide Ceramic Matrix/Oxide Fibre Woven Fabric Composites Exhibiting Dissipative Fracture Behavior," *Composites*, **26** [3] 175–82 (1995).

[14]W. C. Tu, F. F. Lange, and A. G. Evans, "Concept for a Damage-Tolerant Ceramic Composite with Strong Interfaces," *J. Am. Ceram. Soc.*, **79** [2] 417–24 (1996).

[15]C. G. Levi, J. Y. Yang, B. J. Dalgleish, F. W. Zok, and A. G. Evans, "Processing and Performance of an All-Oxide Ceramic Composite," *J. Am. Ceram. Soc.*, **81** [8] 2077–86 (1998).

[16]J. A. Heathcote, X.-Y. Gong, J. Yang, U. Ramamurty, and F. W. Zok, "In-Plane Mechanical Properties of an All-Oxide Ceramic Composite," *J. Am. Ceram. Soc.*, **82** [10] 2721–30 (1999).

[17]M. Mattoni, J. Y. Yang, C. G. Levi, and F. W. Zok, "Effects of Matrix Porosity on the Mechanical Properties of a Porous-Matrix, All-Oxide Ceramic Composite," *J. Am. Ceram. Soc.*, **84** [11] 2594–602 (2001).

[18]M. A. Mattoni and F. W. Zok, "Notch Sensitivity of Ceramic Composites with Rising Fracture Resistance," *J. Am. Ceram. Soc.*, **87** [5] 914–22 (2004).

[19]E. A. V. Carelli, H. Fujita, J. Y. Yang, and F. W. Zok, "Effects of Thermal Aging on the Mechanical Properties of a Porous-Matrix Ceramic Composite," *J. Am. Ceram. Soc.*, **85** [3] 595–602 (2002).

[20]C. G. Levi, F. W. Zok, J.-Y. Yang, M. Mattoni, and J. P. A. Lofvander, "Microstructural Design of Stable Porous Matrices for All-Oxide Ceramic Composites," *Z. Metallkd.*, **90** [12] 1037–47 (1999).

[21]A. G. Evans and F. W. Zok, "The Physics and Mechanics of Fiber-Reinforced Brittle Matrix Composites," *J. Mater. Sci.*, **29** [15] 3857–96 (1994).

[22]W. A. Curtin, "Theory of Mechanical Properties of Ceramic–Matrix Composites," *J. Am. Ceram. Soc.*, **74** [11] 2837–45 (1991).

[23]M. Ibnabdeljalil and W. A. Curtin, "Strength and Reliability of Fiber-Reinforced Composites: Localized Load-Sharing and Associated Size Effects," *Int. J. Solids Struct.*, **34** [21] 2649–68 (1997).

[24]M.-Y. He, B. Wu, and Z. Suo, "Notch-Sensitivity and Shear Bands in Brittle Matrix Composites," *Acta Metall. Mater.*, **42** [9] 3065–70 (1994).

[25]Z. Suo, S. Ho, and X. Gong, "Notch Ductile-to-Brittle Transition Due to Localized Inelastic Band," *J. Eng. Mater. Technol.*, **115** [3] 319–26 (1993).

[26]R. John and B. Rigling, "Effect of Height to Width Ratio on K and CMOD Solutions for a Single Edge Cracked Geometry with Clamped Ends," *Eng. Fract. Mech.*, **60** [2] 147–56 (1998).

[27]Z. Suo, G. Bao, B. Fan, and T. C. Wang, "Orthotropy Rescaling and Implications for Fracture in Composites," *Int. J. Solids Struct.*, **28** [2] 235–48 (1991).

[28]G. Bao, S. Ho, Z. Suo, and B. Fan, "The Role of Material Orthotropy in Fracture Specimens for Composites," *Int. J. Solids Struct.*, **29** [9] 1105–16 (1992).

[29]H. Fujita, G. Jefferson, C. G. Levi, and F. W. Zok, "Controlling Mechanical Properties of Porous Mullite/Alumina Mixtures Via Precursor-Derived Alumina," *J. Am. Ceram. Soc.*, **88** [2] 367–75 (2005).

[30]M. Y. He and J. W. Hutchinson, "Crack Deflection at an Interface Between Dissimilar Elastic Materials," *Int. J. Solids Struct.*, **25** [9] 1053–67 (1989).

[31]ASTM Standard C 20, *Standard Test Methods for Apparent Porosity, Water Absorption, Apparent Specific Gravity, and Bulk Density of Burned Refractory Brick and Shapes by Boiling Water*. American Society for Testing and Materials, Philadelphia, PA, 2002.

[32]ASTM Standard C 1292, *Standard Test Method for Shear Strength of Continuous-Fiber Reinforced Advanced Ceramics at Ambient Temperature*. American Society for Testing and Materials, Philadelphia, PA, 2002.

[33]D. M. Wilson, "Statistical Tensile Strength of Nextel 610 and Nextel 720 Fibres," *J. Mater. Sci.*, **32** [10] 2535–42 (1997).

[34]K. G. Dassios, M. Steen, and C. Filiou, "Mechanical Properties of Alumina Nextel 720 Fibres at Room and Elevated Temperatures: Tensile Bundle Testing," *Mater. Sci. Eng. A*, **349**, 63–72 (2003).

[35]J. Goering and H. Schneider, "Creep and Subcritical Crack Growth of Nextel 720 Alumino Silicate Fibres as Received and After Heat Treatment at 1300 C," *Ceram. Eng. Sci. Proc.*, **18** [3] 95 (1997).

[36]S. J. Connell, F. W. Zok, Z. Z. Du, and Z. Suo, "On the Tensile Properties of a Fiber Reinforced Titanium Matrix Composite—II. Influence of Notches and Holes," *Acta Metall. Mater.*, **42** [10] 3451–61 (1994).

[37]F. W. Zok, "Fracture and Fatigue of Continuous Fiber-Reinforced Metal Matrix Composites"; pp. 189–220 in *Comprehensive Composite Materials*. Vol. 3. Edited by A. Kelly and C. Zweben. Pergamon, Oxford, 2000.

[38]P. Brenet, F. Conchin, G. Fantozzi, P. Reynaud, D. Rouby, and C. Tallaron, "Direct Measurement of Crack-Bridging Tractions: A New Approach to the Fracture Behavior of Ceramic/Ceramic Composites," *Comp. Sci. Technol.*, **56** [7] 817–23 (1996).

[39]J. C. McNulty and F. W. Zok, "Low-Cycle Fatigue of Nicalon-Fiber-Reinforced Ceramic Composites," *Comp. Sci. Technol.*, **59** [10] 1597–607 (1999).

[40]F. A. Heredia, S. M. Spearing, T. J. Mackin, M. He, A. G. Evans, P. Mosher, and P. Brondsted, "Notch Effects in Carbon Matrix Composites," *J. Am. Ceram. Soc.*, **77** [11] 2817–27 (1994). □